SCANNING PROBE MICROSCOPY OF PROTEIN NANOWIRES

By

Kathleen Ann Walsh

A DISSERTATION

Submitted to
Michigan State University
in partial fulfillment of the requirements
for the degree of

Physics – Doctor of Philosophy

2013

ABSTRACT

SCANNING PROBE MICROSCOPY OF PROTEIN NANOWIRES

By

Kathleen Ann Walsh

The bacterium *Geobacter sulfurreducens* grows electrically-conductive pili, which act as protein nanowires, in order to transfer electrons from the cell to electron acceptors in its environment when direct charge transfer through the cell membrane is not feasible. Understanding the electronic structure of the pili can provide insight into fundamental processes of electron transfer in biological systems.

This study investigated the electronic structure of these protein nanowires using the toolbox of scanning probe microscopy, specifically scanning tunneling microscopy and point tunneling spectroscopy. These measurements were performed at 77 K and at room temperature. The measured data are compared to theoretical calculations.

Density of states measurements using tunneling spectroscopy show that these pili act as narrow-gap biological semiconductors at 77 K. The onset of nonzero density of states remains within the metabolically-relevant voltage range. At room temperature, spectroscopy of the pili retains a gap-like structure, but this pseudogap is raised to a nonzero density of states at even the smallest applied voltages. These pilus nanowires also exhibit a distinct spatial dependence of the density of states across the breadth of the pili.

To Mom and Dad—I wouldn't be here without you.

ACKNOWLEDGMENTS

My heartfelt gratitude goes out to Mrs. Kilgore, the *sine qua non* of my scientific career. She stayed after school two evenings every week, offering help to any of her Middle Math II students who wanted to take her up on it and tutoring such students through topics again and again until we could succeed. Without her patient assistance in seventh grade, my life today would be radically different.

I heartily appreciate my friends and colleagues who have made my graduate school experience more cheerful: Jenna, Megan, Sean, Emily, Emi, Carla, Brent, *et al.* Most timely thanks goes to my "thesis buddy" Carla for helping me stay on track lo, these many months. Thanks for the good times, and sorry about the rants.

On the colleague side, Sanela Lampa-Pastirk, in addition to purifying sample for me, was always willing to help me navigate interdisciplinary research and to encourage me not to give up on the ideal of rigor. Josh Veazey was a fountain of insight and perspective. Josh and Sanela laid the groundwork for everything I've done with *Geobacter*. Sean Wagner in the UHV-STM lab next door (and the desk next to mine in the office) taught me STM and has been a great colleague and friend ever since. Nathaniel Leonard generously let me test GSH mode on his samples and worked with me on them. Thanks also go to Scott MacLaren for GSH Mode collaboration (including the name for it) and other wonderful things.

I've been fortunate enough to have several great research mentors. Dr. Elizabeth Behrman was a superlative undergraduate advisor. She convinced me that "words people" can succeed in physics and showed me how to do research. My REU with Norman Birge made it abundantly clear that I wanted to be an experimentalist. Alexandra Gade told me, "You should do something that makes you happy" and encouraged me to go do it.

Stuart Tessmer has been the best graduate advisor I could hope for. Seriously, it's like working for Mister Rogers. I've learned from him not just how to be a better scientist but how to be a better person. Stuart's example proves that being nice all the time is a viable leadership style, one I hope to emulate.

Most CMP experimentalist grad students here thank Reza Loloee, and for good reason. He's always willing to help, is tremendously clever and useful, and genuinely cares about the students. Reza makes sure the basement stays collegial and doesn't get too grim.

Lastly and mostly, I am immensely fortunate to have parents who understand me and are also my friends. Thanks, Mom and Dad.

TABLE OF CONTENTS

LIST OF TABLES

LIST OF FIGURES

Chapter 1

Overture

The search is on for electronic materials with interesting, tunable properties. Complementary to the strategy of devising such materials by doping well-studied crystals to modify their properties in the desired direction is the approach of using and modifying structures already present in natural materials [1]. Among the vast range of suggested such materials are, *e.g.,* nanoscale fibers made from viruses [2]. It has already been established that electrically conductive protein filaments [3] are produced by several different species of bacteria, including the *Geobacter sulfurreducens* species studied in this thesis [4, 5]. Endeavoring to elucidate further the electronic properties of a specific type of protein filament harvested from *G. sulfurreducens* in order to exploit them optimally, as well as to understand how they work on a fundamental level, is the subject of this study—why reinvent the nanowire? The protein nanowires studied in this work are the pili (singular: pilus) expressed by *G. sulfurreducens*, shown in Figures 1.1 and 1.2.

In the course of its metabolic/respiratory process—breathing and eating are much the same to a single-celled organism—*Geobacter sulfurreducens* gains energy by breaking apart organic molecules, which leads to an excess of electrons inside the cell. To discharge itself, *Geobacter* donates these electrons to various electron acceptors in its environment, thereby chemically reducing them. These electron acceptors perform the same role for *Geobacter*, an anaerobic bacterium, that oxygen does for aerobic-respiring creatures.

Geobacter sulfurreducens is often provided with the electron acceptor iron (III) oxide to

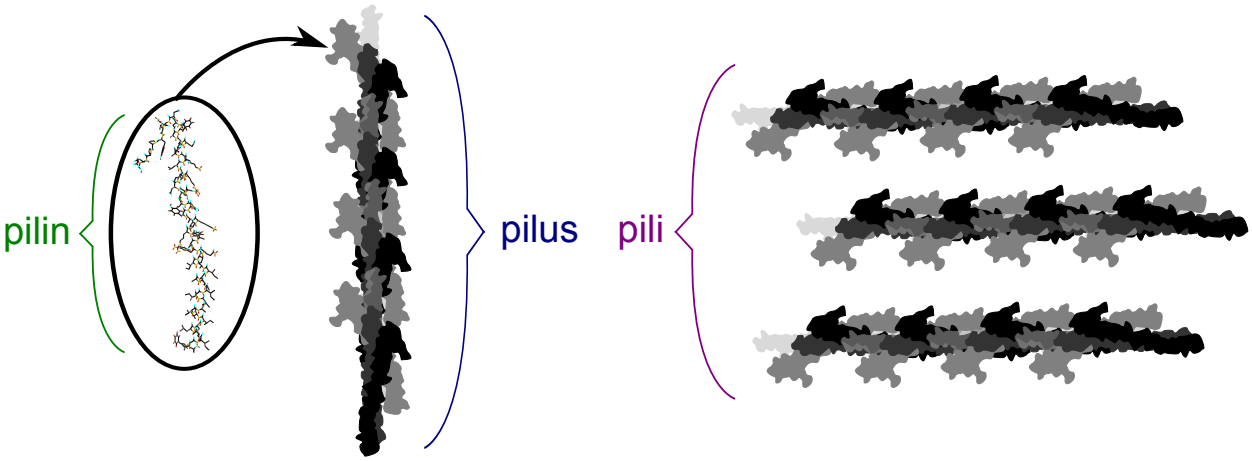

Figure 1.1: Each seahorse-shaped subunit of a pilus is an individual pilin. Four or five pilins make up one turn of the helical pilus [6]. The plural of *pilus* is *pili*. For simplicity, these *Geobacter* pili are sketched with no terminating proteins (coded for by *pilC* in some bacterial pili [6]). Pilin structure is displayed from Swiss-PdbViewer [7] using the coordinates in Reference [8]. Pili were drawn using a space-filling model representation from RasMol [9] as a cookie cutter to form the shapes. For interpretation of the references to color in this and all other figures, the reader is referred to the electronic version of this dissertation.

reduce when grown in the lab because Fe(III) oxide is the classic electron acceptor of this type of metabolic process [10]. Alternatively, *Geobacter* can take advantage of other electron acceptors in the environment, including uranium (VI) oxide [11, 12]. This makes *G. sulfurreducens* an exciting candidate for bioremediation schemes [13], since reducing uranium (VI) oxide to uranium (IV) oxide—which *Geobacter* species can do—decreases its solubility and precipitates the uranium out of groundwater, which can therefore decrease the spread of uranium contamination [11]. Such schemes are currently limited by scalability issues due in part to the large areas involved and the small size of the bacteria, as well as frequently-significant differences between laboratory conditions and field-scale circumstances [14]; hence much further study is needed to aid in making the process viable. Furthermore, this ability of *G. sulfurreducens* to transfer negative charge to an acceptor material enables it to be used in microbial fuel cells, as in Figure 1.3. Replacing the standard environmental electron acceptors such as Fe(III) with the anode electrode of a battery to be charged or a device

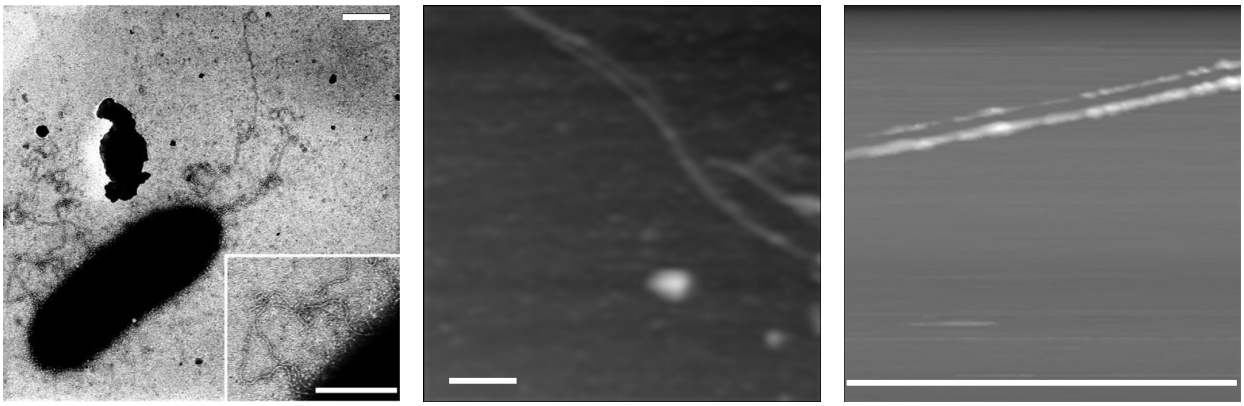

Figure 1.2: The pilus nanowires of *Geobacter sulfurreducens*, observed using different magnifications and different microscopies. Left: Transmission electron micrograph of *G. sulfurreducens* cells and pili from Reference [3]. Adapted by permission from Macmillan Publishers Ltd: NATURE [3], copyright 2005. Center: Atomic force micrograph of purified *Geobacter* pili. Right: Scanning tunneling micrograph of a purified *Geobacter* pilus (the "echo" above the pilus is due to a multiple-tip effect). Scale bars are 200 nm.

to be powered, and inserting hydrocarbons such as acetate for *Geobacter* to break up into carbon dioxide, enables *Geobacter*'s metabolic process to be used for electricity generation applications [15]. The continued efficiency of these microbial fuel cells as *Geobacter* cells grow into stacks and form a biofilm can be attributed to the pili [16] which are the subject of this research. Pili allow cells in the biofilm whose membranes are not directly touching the electron acceptor still to be in electrical contact with it [16].

For the cell to reduce the electron acceptor, it must by some means transfer its excess electrons to that electron acceptor. Soluble electron acceptors can permeate directly into the cell. Alternatively, the cell membrane can be in direct contact with an insoluble electron acceptor, for example when insoluble electron acceptors are diffusing through the cell's environment and occasionally encountering the cell or when the cell is sitting directly atop an insoluble electrode in a microbial fuel cell [16]. In this case, the cell can transfer the electrons to the electron acceptor through, *e.g.,* metal-containing cytochromes in the outer membrane of the cell [17]. If, however, the outer cell membrane is not in direct contact with electron

acceptors, for example if it is "land-locked" in the middle of a biofilm, the cell must find an alternate means of discharging itself. One method is to use intermediary electron acceptors, called electron shuttles, which diffuse between the cell and the terminal electron acceptor elsewhere in the environment; this is essentially creating soluble electron acceptors to move between the cell and an insoluble electron acceptor elsewhere. These electron shuttles diffusively move to the cell membrane, at which point the cell discharges itself onto the electron shuttle; the newly-reduced electron shuttle then diffuses away and eventually relieves itself of that excess charge against another electron acceptor elsewhere, freeing it to begin again [17]. This approach is so favored by some bacteria that they actually express proteins to manufacture these electron shuttles and release them into their environment; this is done by the *Shewanella* species [18]. Although *Geobacter* species do not manufacture electron shuttles [19], if electron shuttles are present in the environment, *Geobacter* will discharge itself onto them as it would with other soluble electron acceptors [18]. In biofilms, the stacks of bacteria are surrounded by a medium filled with all manner of cellular byproducts and assistive molecules, so isolation of the components of the biofilm is necessary to determine the critical component for electron transfer. The research described here builds on previous studies, *e.g.,* Reference [3], which have determined that the pili, protein nanowires extended from the cell membrane, are responsible for electrical transport from *G. sulfurreducens* to spatially distant elements of its environment.

Geobacter sulfurreducens, and also certain other bacteria, express electrically conductive type IV pili to perform electron transport to insoluble electron acceptors at some distance from the cell [3]. Type IV pili are grouped together based on similarities in the amino acid sequences of their pilins [20]. The type IV pilus structure is common among bacteria and used for different purposes by different species; some bacteria use them for locomotion, but

this does not appear to be the case for *Geobacter sulfurreducens* [10], and some bacteria use them to help hold bacterial biofilms together structurally, which does appear to be one function of *Geobacter*'s pili [21]. *Geobacter*'s pili are electrically conductive, but not all type IV pili are electrically conductive; the pili of *Pseudomonas aeruginosa* strain K, for example, are insulators [22]. Type IV pili are composed of subunits, called pilins, which are expressed inside the cell, assembled inside the cell's outer membrane and pushed outside the cell through a pore in the outer membrane [6]. Each pilus has a repeating helical structure comprised of pilin subunits and can grow to be at least several micrometers long (see, *e.g.,* Figure 1.2 or Reference [3]).

Veazey *et al.* [23] established that the protein matrix of the pili, rather than associated cytochromes or metal atoms, are responsible for the electronic conductivity of the pili. Such purified protein nanowires [12] were investigated in this research. Pili in bacterial biofilms are accompanied by various other extracellular productions of the bacteria, including metal-containing molecules. For this study, these molecules were removed [12], leaving only the purified protein matrix.

While several studies have addressed axial charge transport along the length of nanowires of various species (*e.g.,* [24, 25]), transverse properties of the nanowire diameters are also a subject of consideration, as pili are permitted to intertwine with one another [26], and as pili are electrically conductive in the transverse direction [3].

The aim of this research is to study the electronic properties of the protein nanowires grown by *Geobacter sulfurreducens*. To this end, the pili are investigated by physical techniques as other kinds of nanowires, *e.g.,* carbon nanotubes, would be [27]. Indeed, point tunneling spectroscopy, a technique used on the pili for this research, was able to categorize carbon nanotubes as having semiconducting or metallic electronic structures, depending

on their physical structures [28, 29]. The density of states of the pili contains detailed information about the electronic structure of these protein nanowires, as discussed further in Chapter 2. Density of states measurements can be obtained with high spatial precision using the spectroscopic capabilities of the scanning tunneling microscope (STM). Scanning tunneling microscopy and point tunneling spectroscopy employ a repositionable, sharp, electrically conductive tip in close proximity to the sample to achieve nanometer-scale resolution of the sample topography. Similarly, nanoscale positionability of the localities for the spectroscopy measurements is obtained. Using scanning tunneling microscopy and spectroscopy, the density of states has been measured for wild-type *G. sulfurreducens* pili at 77 K and at room temperature. Temperatures are generally referred to here using two significant figures, *i.e.,* 300 K rather than 297 K.

Throughout this document, both the words "pilus" and "nanowire" are used interchangeably to refer to the pili grown by *G. sulfurreducens* which act as a biological type of nanowire; the electrically conductive pili behave like wires of nanometer-scale diameter. Often, the terms "bias" and "voltage" are used synonymously, as well. Because of the interdisciplinary tone of this research, various terms in this document may reflect different usages in different fields of study. Such terms include "substrate," which is always used here in its physical sense as an underlying surface upon which the subject of primary study is present, rather than in its biochemical sense. Another source of verbal subtlety lies in the names for different components of the protein nanowires under study here, as but a single letter makes the difference between discussion of a pilin (subunit of a pilus) and of pili (more than one pilus). For clarity, a terminology guide is presented in Figure 1.1.

Beginning with a discussion of the scanning probe microscopy techniques (Chapter 2) and specific microscopes (Chapter 3) used for this research, this document proceeds through

an overview of the samples studied and the theoretical underpinnings of the interpretation framework (Chapter 4). The results are then presented, together with conclusions drawn from them and suggested directions for future investigations (Chapter 5). The primary Appendix describes other work done supervising, maintaining, and using an atomic force microscope facility instrument (Appendix A). The remaining appendices present cautionary tales of pili-like artifacts (Appendix B) and further details regarding the sample preparation (Appendix C), techniques, and equipment used in this (Appendix D) and closely-related research (Appendix E) on the protein nanowires of *Geobacter sulfurreducens*.

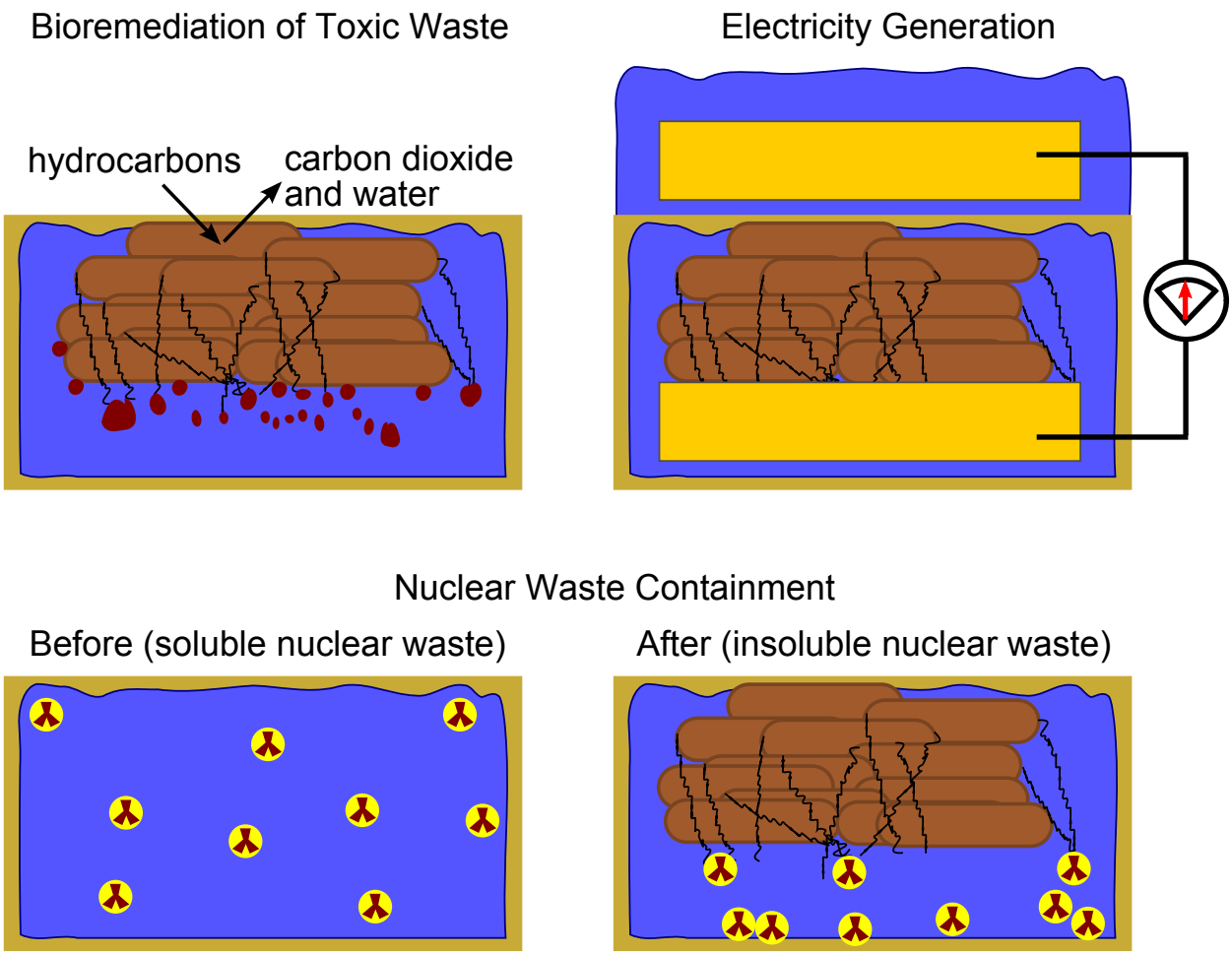

Figure 1.3: Some of the applications of *Geobacter*. In this diagram, brown rods represent cells, and black filaments represent pili. All examples here show biofilms of *Geobacter* in water-containing sediments. Upper left: Bioremediation of chemically toxic waste. Other bacteria break up complex organic waste into fermentation products [15], and *Geobacter* breaks it down still further. Upper right: Microbial fuel cell. The example pictured is based on the "BUG" design for seafloor power generation, as in Reference [15]. Bottom: Bioremediation of nuclear waste. Soluble nuclear waste (*e.g.*, U(VI) oxide) is chemically reduced and thereby rendered insoluble, at which point it precipitates out rather than perpetuating in groundwater.

Chapter 2

Scanning Probe Microscopy

The field of scanning probe microscopy covers a wide range of tools and techniques designed to investigate the properties of surfaces at the nanoscale [30, 31]. Among the myriad techniques falling under this general heading are the original scanning tunneling microscopy and other tip-based techniques such as atomic force microscopy. Unlike optical microscopy, the tip-based scanning probe microscopies are not limited by considerations of the wavelength of the photons which probe the sample but rather by the sharpness of the tips, making high spatial resolution on the angstrom or nanometer scale much easier to achieve.

While the primary tools of investigation for this research were scanning tunneling microscopy (STM) and, particularly, its close relative point tunneling spectroscopy, atomic force microscopy (AFM) was also used to obtain some of the topographs presented here. For this reason, a brief introduction to AFM is included in the description of the scanning probe microscopy methods used. The AFM scans discussed here were performed solely at room temperature, but the STM and point tunneling spectroscopy studies were done both at room temperature and at liquid nitrogen temperature (77 K) in order to investigate the temperature-dependence of the measured properties, in particular the density of states of the pilus nanowires produced by *Geobacter sulfurreducens*.

This Chapter discusses the underlying principles beneath the scanning probe microscopy measurements performed in the course of this research. Specific details of the microscopes used in this study are discussed in Chapter 3. Further details regarding some of the back-

ground for the scanning probe microscopy techniques used in this research are given in Appendix D.

2.1 Key Aspects of Scanning Probe Microscopy

In its most general sense, scanning probe microscopy uses some type of probe which gives resolution often on the (sub-)nanometer or micron scale and rasters it along or near the sample to be scanned. Since the focus of this study was on electronic properties in a sample as reflected in the density of states at the sample's surface, the science of interest in this study was amenable to the techniques of scanning tunneling microscopy, its near cousin point tunneling spectroscopy, and atomic force microscopy.

2.1.1 Overview

For experiments such as those discussed here, the aim is to gain information on the nanoscale properties of the system. While properties of bulk amounts of the sample can be measured with mesoscale electrodes and their properties averaged (for the case of *Geobacter* pili, see, *e.g.,* Reference [32]), the optimal way to investigate the properties of a small sample such as a nanowire is to probe one instance of the sample itself rather than an assembly of such. For samples which are small and not easily positionable, it behooves the experimenter to position the measurement device instead: if the sample won't come to the probe, the probe will come to the sample. This ability to reposition the probe is a chief strength of scanned probe microscopies.

The positioning of the tip and sample with respect to each other is conventionally achieved by mounting either the tip or the sample on a scanner made from a piezoelectric material.

(While some microscopes scan the sample with respect to a stationary tip, a larger number of the microscopes used for this study scan the tip with respect to a stationary sample, so for simplicity, the tip-scanning scenario will be used for the following description.) Since piezoelectric materials expand or contract in response to applied voltages, computer-controlled electronic signals can be used to direct the motion of the tip by controlling the extension or compression of elements of the piezoelectric supports. The tip is rastered along the sample by being moved back and forth with some speed along one direction while the tip is slowly moved in the orthogonal direction. Proper tip–sample separation is maintained in the z direction by a feedback loop which, in the case of the standard "constant current" STM mode, constantly compares the detected tunneling current to a predetermined setpoint. If the tunneling current is insufficient or is too great, the tip is extended or retracted until the detected tunneling current reaches the setpoint. Further discussion of this raster scanning motion and the feedback is reserved for Appendix D.

2.1.2 STM and AFM Tips

Not all scanning probe microscopies use physical tips to obtain information about the sample, but tip characteristics are critical for the techniques used in this study. The details of the specific tips used for this research will be discussed in Chapter 3, but a few general remarks will be mentioned here as to the properties of and common modes of confusion resulting from STM and AFM tips.

Tip Properties

In order to achieve the nanometer-scale resolution used for these measurements, the tips must be extremely sharp. In general, STM and some AFM techniques routinely achieve atomic

resolution; however, this was not necessary for this study. The STM tips used here were mechanically cut from Pt:Ir wire (80% platinum, 20% iridium). Well-formed mechanically cut tips have a radius of curvature at the tip apex of approximately several tens of nm [30], although only the few tip atoms nearest the sample are relevant for STM.

During an STM experiment, the tip and sample are brought to a separation of approximately one nanometer, as shown schematically in Figure 2.1. This is close enough that quantum tunneling of electrons between the tip and the sample, with the dominating directionality set by a voltage between the tip and the sample, can reach the relatively easily-detectable nanoampere regime. While other portions of the tip may come within a few nanometers of the surface as well, tunneling will be predominantly through the atom or few atoms at the apex of the tip.

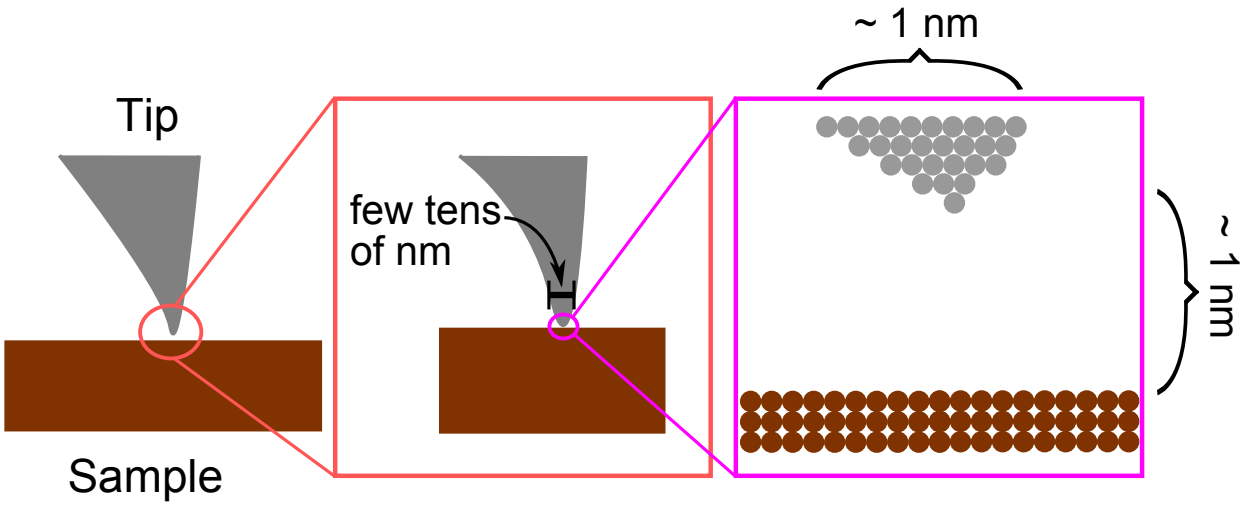

Figure 2.1: Schematic of an STM tip and sample at progressive layers of magnification moving from left to right. Large circles in the right image represent atoms surrounded by mobile electrons. The radius of curvature of a typical tip is several tens of nanometers. The apex of a good tip is essentially a single atom.

Tip Artifacts

Because the tunneling current detected by STM depends exponentially on tip–sample separation, only the last few atoms of the STM tip are relevant. For small, flat scan areas, this can even be only the single atom at the very apex of the tip [33]. When the scan incorporates features of different heights, such as pili or graphite step edges, multiple "minitips" at the apex of the tip can be as close as a few angstroms together [33] or several nanometers apart from one another. These multiple tips are generally at different distances away from the sample and, hence, contribute to the net image with different strengths. The configuration of the multiple tips can often be deduced from the scan image itself. The number of multiple minitips involved can be deduced from the number of times each feature in the image is repeated. An example of a multiple tip causing repeated images is given in Figure 2.2, and the topic is discussed further, with an even more egregious example of a multiple tip, in Appendix B.

2.2 Scanning Tunneling Microscopy

Scanning tunneling microscopy [34] rasters an electrically conductive tip in close proximity to (but not touching) a surface which is not a strong insulator. Electrons naturally quantum mechanically tunnel between the tip and the sample, and by applying a bias voltage between the tip and the sample, the preferential direction of tunneling electrons and the probability of tunneling can be controlled. This is schematically shown in Figure 2.3.

When looking at feature sizes on the order of 1 nm, as done in this study, the shape of the molecular orbital at the end of the tip can be ignored, and it can be assumed that the wavefunction of the apex of the tip is a (spherical) *s*-orbital [30], meaning that the subatomic

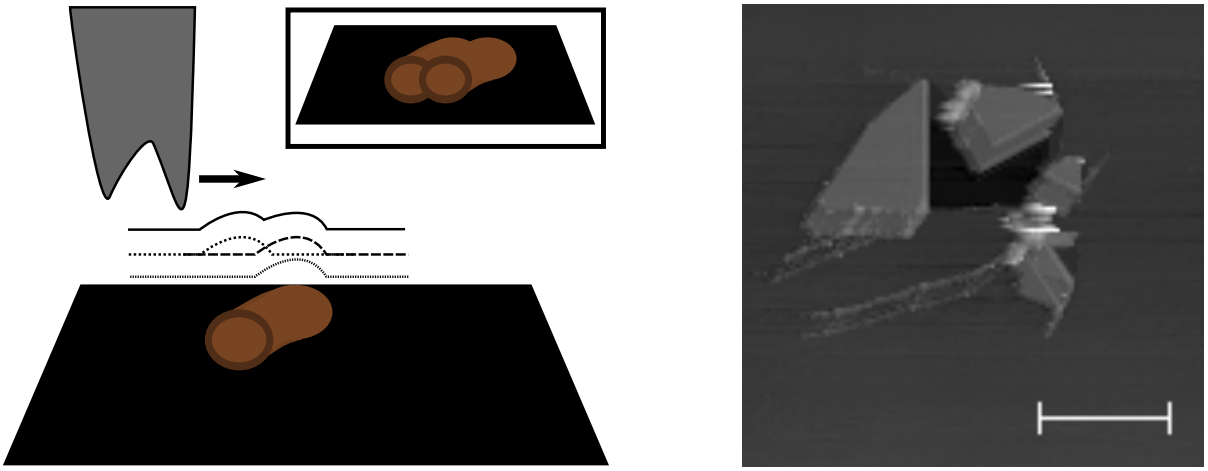

Figure 2.2: Left: Diagram of a typical multiple tip. The feature on the sample is measured first with the rightmost tip, then with the left tip, and the two values are summed together to give the appearance of two features. The bottom trace is that attributable to a single tip; the dashed and dotted traces are the superimposed images due to both the tips, and the top trace is the result. The inset image is how the feature would appear to the experimenter. Right: Pili and graphite flakes imaged by a multiple tip; scale bar is 200 nm. Imaged with applied bias voltage + 0.5 V and tunneling current setpoint 0.1 nA. (+ 0.5 V, 0.1 nA)

shape of the tip does not contribute to the resolution of the image.

2.2.1 Review of Tunneling Through an Energy Barrier

This brief review of tunneling through a finite energy barrier is not only relevant to the basic principle of STM operation but also to the schematic model for tunneling between available energy states within the pili, as discussed in Chapter 4. Both for tunneling between the tip and sample in STM and for tunneling from site to site along the nanowire, it is sufficient to consider the one-dimensional case. Since a well-formed STM tip is extremely sharp and has a sufficiently high aspect ratio, only the few atoms at the very apex of the tip contribute to the signal, as will be discussed below, and for site-to-site tunneling through nanowires, each piecewise step along the tunneling pathway can be considered to be along one dimension. This discussion follows the simplest case described in Reference [30]; similar

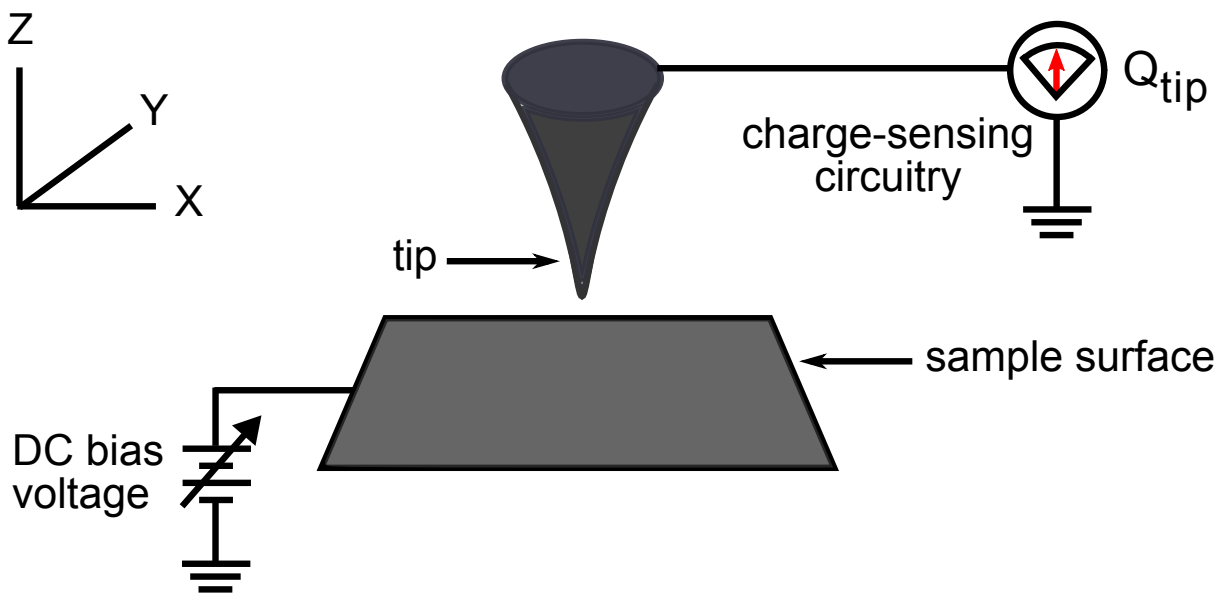

Figure 2.3: Diagram of an STM experiment. An atomically sharp, electrically conductive tip is rastered very near to an electrically non-insulating sample, which is biased at a voltage value chosen by the operator. Electrons tunneling between the tip and the sample are measured by sensitive charge-detection circuitry, and the z position of the tip is adjusted to keep the detected tunneling current, proportional to the number of tunneled electrons per second, constant.

and more involved discussions can be found in essentially any STM book, as well.

Start from the Schrödinger equation for one electron tunneling between the tip and sample in the z direction,

$$-\frac{\hbar^2}{2m}\frac{d^2}{dz^2}\psi(z) + U(z)\psi(z) = E\psi(z) \tag{2.1}$$

with $U(z)$ used here to denote the potential to avoid confusion with the voltage V. For simplicity in the immediate discussion, consider the case where both tip and sample are metals so the conduction electrons can move freely. Electrons are superpositions of plane waves inside the metals, $\psi(z) = \psi(0)\, e^{\pm ikz}$, with k given by $k = \frac{\sqrt{2m(E-U)}}{\hbar}$. The probability of an electron being found inside this barrier decreases rapidly the further along z into the

barrier the electron is sought. The electron wave function decays exponentially with barrier depth: $\psi(z) = \psi(0)\ e^{-\kappa z}$, where the decay constant $\kappa = \frac{\sqrt{2m(U-E)}}{\hbar}$. The tunneling current can be described as the number of electrons per unit time which tunnel through the barrier into the second metal, where they're detected by the electronics in the rest of the apparatus. Thus *the tunneling current is exponentially dependent upon distance.* The work function ϕ of a material is the energy required to remove an electron from the material into the vacuum (this is larger than the energy due to the applied bias in the STM system, $e \times V$ [30]), as indicated in Figure 2.4. Using typical values for work functions of materials used in STM, the tunneling current decays an order of magnitude for every angstrom of separation between the materials [30]. This is a significant and frequently-invoked idea, as it is responsible for the excellent lateral resolution of STM, the relevance of only the nearest few atoms to the sample in STM tips, and the limited spatial ranges throughout biological samples in which tunneling conductivity can be significant.

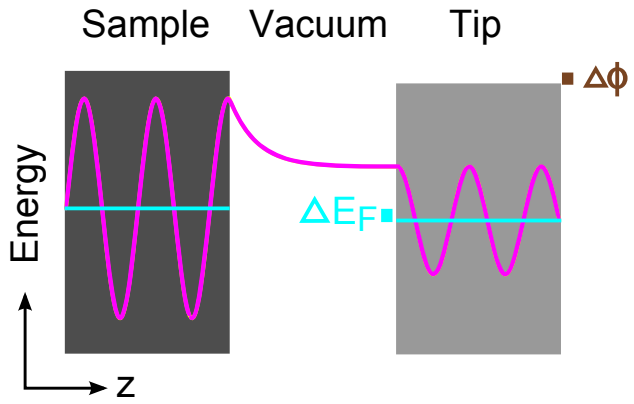

Figure 2.4: Diagram of one-dimensional tunneling for the STM tip–sample system. Electron wavefunctions are shown superimposed on gray-colored rectangles representing the electronic states available within the materials. Electron wavefunction in each region shown in fuchsia. Fermi energy of each material shown in cyan. The difference between Fermi levels of the materials is shown by a cyan slab (this can be controlled by applying a bias voltage), and the difference between work functions of the materials is shown by a brown slab.

Applying a bias voltage tilts the energy barrier such that one side of the barrier has

available empty states at the same energy as there are filled states on the other side of the barrier. A tilted energy barrier also occurs due to tunneling between materials with different work functions. This tilt is shown as the difference in heights of the gray backgrounds of the different materials in Figure 2.4. In the case of a positive bias applied to the sample, this means energy states in the sample are opened up for electrons from the tip to tunnel into. Most scans performed during the course of this research were done with a positive bias applied to the sample, which investigates the emptied states near the Fermi level of the sample. A sketch of tunneling between the tip and the sample is given in Figure 2.5. An applied bias voltage enhances the tunneling probability in a particular direction.

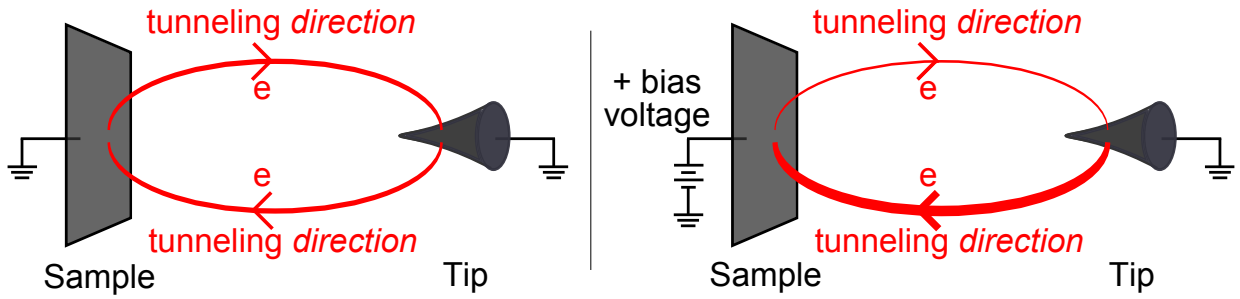

Figure 2.5: Diagram of the effect of bias voltage on tunneling. Left: Both tip and sample are grounded. Electrons can tunnel between tip and sample with equal probability, here represented by the thickness of the curves. Right: Positive bias applied to the sample. Electrons continue to tunnel in both directions, but the tip-to-sample tunneling probability is enhanced by the applied positive bias. Since this is a tunneling process, these lines do *not* represent travel paths; rather, the detected position of the electron changes discontinuously from tip to sample or *vice versa*.

The details of the tunneling are perhaps clearer in terms of the local density of states (LDOS) of the tip and the sample in an energy level picture. The term "density of states" refers to the number of available quantum states for particles (considered here to be electrons for simplicity) to inhabit as a function of energy. STM, by applying a bias voltage between the sample and the tip, provides an energy equal to the charge of the electron multiplied by the applied voltage. Electrons will fill states between the Fermi energy (zero applied

voltage, hence zero applied energy) and the energy corresponding to the bias voltage, hence the STM signal integrates over the energies between the Fermi energy and the bias energy. Assuming the density of states of the tip is constant throughout the scanned image and only the LDOS of the sample can vary, and neglecting thermal effects on the Fermi-Dirac distribution describing the electrons, the tunneling current signal

$$I(V) \propto \int_{E_F}^{eV} \psi^*_{sample}(\epsilon)\ \psi_{sample}(\epsilon)\ d\epsilon = \int_{E_F}^{eV} LDOS_{sample}(\epsilon)\ d\epsilon \tag{2.2}$$

where E_F is the Fermi energy and eV is the energy corresponding to the applied bias voltage V [30]. The number of electrons which tunnel at a given voltage in an STM experiment is a function of the density of states in that energy range. When there are more states available for the electrons to fill, the detected tunneling current will be greater in magnitude. The tip is made of a material which has an innocuous density of states in the energy regimes relevant to these experiments; consequently, any features seen in the observed tunneling current are due to the properties of the sample. A sketch of the density of states of the tip and the sample during an STM measurement is given in Figure 2.6. Further discussion of the density of states is reserved for the description of point tunneling spectroscopy below.

2.2.2 Topography and Local Density of States Probed by STM

STM topographs are a convolution of the physical height of features on the sample *and* the tip and of the local density of states of the sample *and* the tip. Ordinarily, the tip density of states can be ignored unless the tip becomes contaminated by extraneous material. If the tip is uncontaminated and is neither a multiple tip nor particularly blunt, its effect on the resulting STM image can be ignored, and features in the STM topographs can be attributed

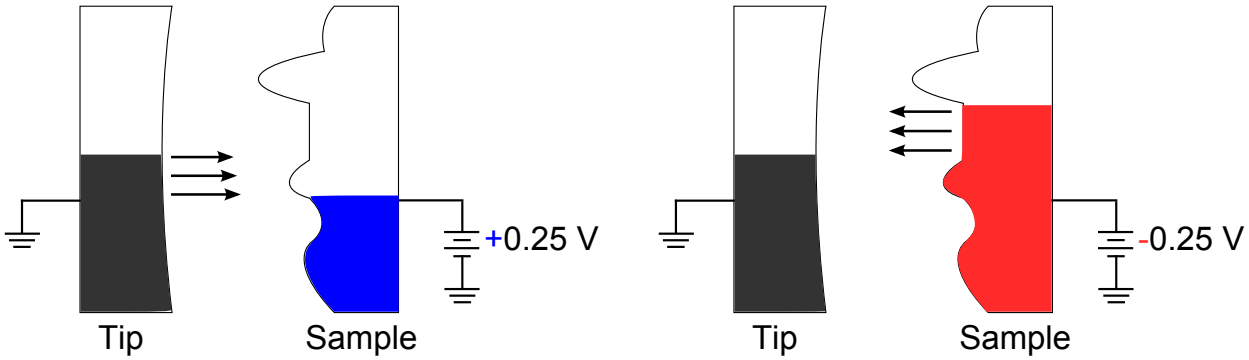

Figure 2.6: Diagram of the effect of bias voltage, showing the electronic states of the tip and the sample. Shaded areas represent filled electronic states. Arrows denote electron net tunneling direction. The tip has a smooth density of states. The sample density of states here has discernible features. Left: Sample is positively biased with respect to the tip. Electrons from the tip tunnel into sample states with energies between the Fermi energy and the energy set by the applied bias voltage. Right: Sample is negatively biased. Electrons from the sample tunnel into tip states between the Fermi energy and the bias energy.

to a convolution of the sample geometry and local density of states.

An example of STM topography is shown in Figure 2.7, along with a height profile along part of the image. The high spatial resolution of STM permits topography of very small features, including single atomic layers of graphite as in Figure 2.7. STM topographs are generally labeled by the bias voltage applied to the sample and the tunneling current setpoint used during the particular scan, thus: (+ 0.5 V, 0.1 nA).

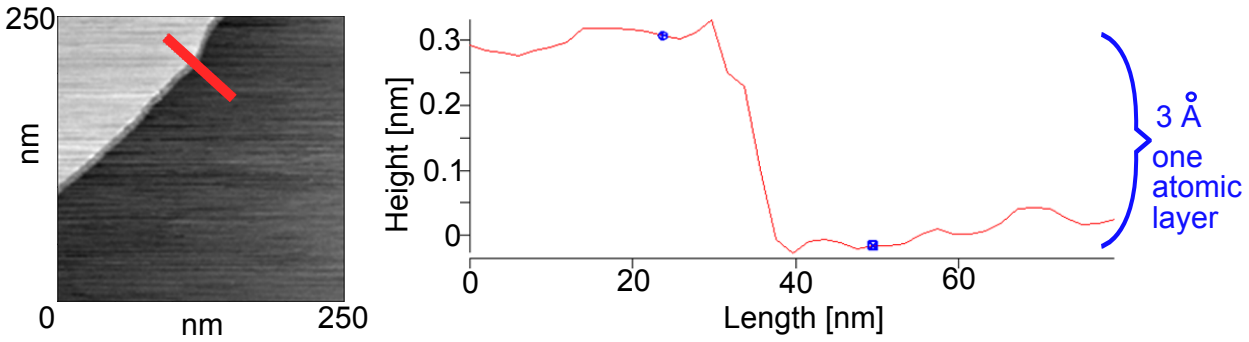

Figure 2.7: Left: 250 nm × 250 nm STM topograph of a graphite step edge. The red line marks the location of the height profile to the right. Right: Line section across the edge. The blue points on the section are separated by the height of one atomic layer of graphite. (+ 0.5 V, 0.2 nA)

The word "topograph" is used somewhat euphemistically, since electronic effects often dominate the details of the topographs, as STM is sensitive to the entire wavefunction of the sample, not just to the spatial positions of various elements of the sample. For this reason, pronouncements about the true conformation of sample features must take into account the local density of states information about the sample, either by acquiring topographs at various bias voltages or by performing spectroscopy measurements [35]. Since the samples studied in this work were not perfectly flat, the geometric properties of the sample terrain also contributed greatly to the resulting topographs.

2.3 Point Tunneling Spectroscopy

A primary motivation for the development of STM was the quest for the ability to obtain tunneling spectroscopy measurements with high spatial resolution [36, 37]. Point tunneling spectroscopy, hereafter often referred to for brevity as "spectroscopy," is a process whereby a scanning tunneling microscope probe is parked in position at one point of a sample, the bias voltage is ramped over a range, and the resultant tunneling current is monitored. (This is the "tunneling" in "point tunneling spectroscopy.")

Tunneling spectroscopy allows a nearly-direct view of the electronic levels in the sample, since it measures tunneling current at a range of voltages instead of at a single bias voltage. The "nearly" qualifier is because the signal will be slightly obscured by convolution with instrument properties and with statistical effects due to nonzero temperature, discussed in Chapter 5. Similar information could be obtained by acquiring STM whole-image topographs at a range of bias voltages (voltage dependent imaging), but the spectroscopy measurement approach allows the range of bias voltages to be investigated at each individual

selected point on the sample. (This is the "point" in "point tunneling spectroscopy.") An extended variant of this technique, scanning tunneling spectroscopy (STS), performs spectroscopic measurements at every point in the scan, as does the current imaging tunneling spectroscopy (CITS) technique [38]. In this research, point tunneling spectroscopy was used to probe the local density of states. Point tunneling spectroscopy is a subset of scanning tunneling spectroscopy wherein the voltage is ramped and the local density of states is investigated at one location within an STM scan, rather than at every point. The primary reason for choosing to perform point tunneling spectroscopy rather than scanning tunneling spectroscopy measurements with the apparatus used for this research is that, since the measurement is done once per scan rather than at every pixel of the scan image, the scans complete far more quickly, thus decreasing the impact of mechanical or thermal drift, which could otherwise cause the target features to shift within the image. Since spatial dependence of the spectroscopic results across the breadth of the pili was one of the research questions of interest, minimizing drift was a strong incentive.

2.3.1 Density of States

STM and its associated spectroscopic techniques probe the density of electronic states in a localized region of the sample, in addition to surface geometry in the case of STM topographic imaging. The detected tunneling current signal is proportional to the number of quantum states available for electrons to inhabit at a particular energy or range of energies. The "density" in the term refers to a number density of electronic states available as a function of energy. This provides valuable information about the electronic structure of the sample. The density of states of a sample is probed slightly differently by point tunneling spectroscopy and by STM. These methods integrate over the energy range between the Fermi energy and

whichever voltage is applied at the time; since this voltage is swept through a range during spectroscopy, more energies can be more easily probed by spectroscopy.

In point spectroscopic density of states measurements, the number of states at each energy is obtained, where the applied voltage selects the energies probed. Point tunneling spectroscopy measurements like the ones discussed here differ from transport measurements in that the tip is spatially separated from the sample, meaning the electrons must tunnel across the gap between the tip and the sample rather than move through an electrical contact with some contact resistance. Because of the exponential dependence of tunneling current on distance, these measurements are localized to a small area at the surface of the sample. The resultant measurement is the density of states, convolved with effects from the nonzero temperature at which the measurement was performed, as well as by settings on the experimental apparatus that affect the measurement's energy resolution. Such smearings cause the discrete, closely-spaced energy levels to appear experimentally as a continuum, as sketched in Figure 2.8.

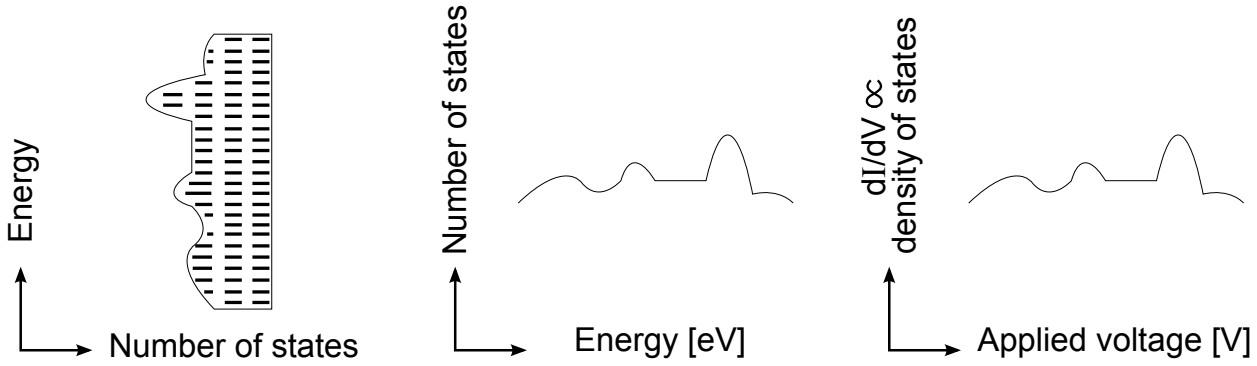

Figure 2.8: Diagram of density of states in point tunneling spectroscopy measurements. Left: The number and width of the dashes at a given energy corresponds to the number of available electronic states at that energy. The outline reflects that the observable which is proportional to the density of states appears to be a continuous quantity, due to thermal and experimental smearing of energy levels. Center: Same as left, with axes switched and dashes removed. Right: Same as left and center, as it would appear experimentally.

2.3.2 Local Density of States Probed by Point Spectroscopy

The local density of states of the sample and tip are probed by point tunneling spectroscopy. For sample feature sizes $\geq$ 1 nm, such as the pili studied here, the tip can be considered to be cylindrically symmetric and its angular momentum orbital shapes neglected, thus spectroscopy probes the electronic states of the sample for features of this size [30].

The "dynamic conductance" or "differential conductance" dI/dV is proportional to the local density of states of the sample, as can be observed by differentiating Equation 2.2, albeit features in the spectrum are smeared by thermal effects and equipment settings. This can either be obtained by performing numerical derivatives of the I–V curves or by direct measurement using a lock-in amplifier, discussed further in Appendix D. The relationship of features in the dI/dV curves to one another is the useful information, not the absolute magnitude of the differential conductance, save that $dI/dV = 0$ is an important landmark in some dI/dV spectra. Because of this and of the subtleties involved in calibrating an absolute dI/dV measurement, it is conventional to present these results in arbitrary units, plotted against the swept bias voltage [30]. An alternate convention for displaying this information is the "logarithmic density of states," $dI/dV \;/\; (I/V) \;=\; d\ln(I)/d\ln(V)$. The wary may note that this quantity increases vigorously near zero voltage. This can be somewhat alleviated by averaging over nearby values of the current [30] or by selecting one particular nonzero voltage to calculate the (I/V) for normalization [39], but rather than introduce more layers into the data analysis, this work presents dI/dV data rather than the logarithmic density of states. Furthermore, normalization issues in the differential conductance become predominantly relevant for larger voltages than those used in this work.

An example of point tunneling spectroscopy on graphite is shown in Figure 2.9. The

amount of scatter in the data is normal and is partially influenced by the electronics used to measure such small currents. This scatter adds substantial noise to the numerical derivatives used to obtain dI/dV curves, so after the five immediately-sequential I–V curves are obtained and averaged together, they are smoothed using a standard Savitzky-Golay algorithm before differentiation, as discussed in more detail in Appendix D.

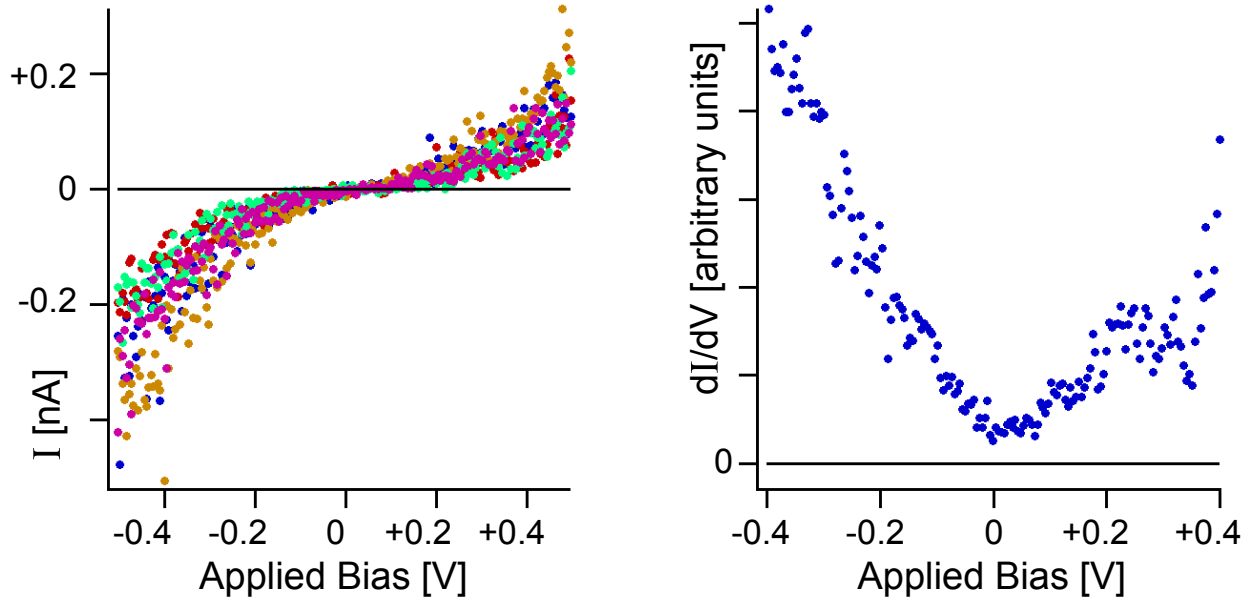

Figure 2.9: Point tunneling spectroscopy on graphite. Black horizontal lines are at zero. Left: Five I–V curves taken immediately in succession. Right: Numerically-differentiated dI/dV of the average of those five curves, with 47-point Savitzky-Golay smoothing prior to differentiation to stabilize the derivative. The extent of the voltage scale is reduced in order to avoid artifacts of the derivative at the endpoints of the I–V curve.

2.3.3 Interpretation of dI/dV Curves

As mentioned above, the ordinate of the dI/dV curves is conventionally plotted using arbitrary units, as it is the *relative* heights of features in the dI/dV curves with respect to one another that are meaningful. Zero is the only special value on the ordinate axis, as a value of zero dI/dV for a particular voltage means there are no electronic states available

at that energy. If dI/dV is zero over a range of voltages, as in the example sketch shown in Figure 2.10, this means in turn that I–V is constant over that voltage range, so adding electrons to the system does not increase the observed current; this is characteristic behavior of a semiconductor inside its bandgap or of an insulator.

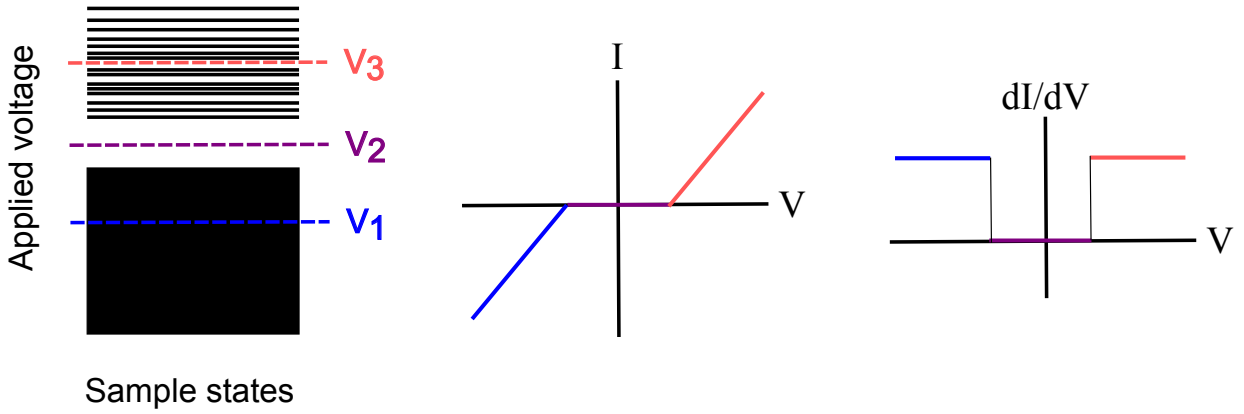

Figure 2.10: Diagrammatic I–V and dI/dV plots for the idealized semiconductor pictured on the left. As the voltage is swept from V_1 to V_3, the I–V curve behaves linearly in the valence band of the semiconductor (dI/dV is constant), the I–V curve is zero for the range of voltages inside the bandgap (dI/dV is zero), and the I–V curve is linear again (dI/dV is constant) when the applied voltage reaches the conduction band of the semiconductor.

In analyzing dI/dV curves where gap-like features are observed in the density of states, as will be discussed in Chapter 5, the edges of the gap are conventionally determined by the voltage at which the dI/dV curve rises steeply above the flat gap bottom. This is remarked upon here because often width determinations in science are done using the full width at half maximum, and gap edge location is not conventionally determined that way except when the logarithmic density of states, $dI/dV \ / \ (I/V) \ = \ d\ln(I)/d\ln(V)$, is used instead [40].

Additionally, as is common in tip-based scanning probe techniques, the tip would not infrequently change its characteristics semi-spontaneously. Since the actual measurement is a convolution of the properties of the sample and of the tip, it was important to characterize the tip frequently to ensure that artifacts were not causing spurious results such as those

highlighted in Appendix B. For example, if during a dI/dV measurement, a fragment of the sample was attracted to the tip and remained affixed there afterwards, a control measurement on graphite would then exhibit density of states characteristics of the sample. For this reason, repeated control measurements on a portion of the sample with a well-known density of states, such as the graphite substrate near the pili, are advisable and were frequently performed in this work.

2.4 Atomic Force Microscopy

While the heart of the research discussed here lies in scanning tunneling microscopy and in spectroscopy, some of the topographic scans presented here were obtained using atomic force microscopy (AFM), so it will be briefly discussed here. Additionally, the technique is intimately connected with the discussion in Appendix E. Only the amplitude modulation mode of AFM scanning will be discussed in this Chapter, with discussion of conductive AFM reserved for Appendix D. Originally developed by the team that invented the STM [41], the atomic force microscope has progressed over the past nearly three decades into a standard surface inspection tool. Just as standard STM topographs maintain a constant current between the tip and the sample, AFM topographs maintain a constant force between the tip and the sample.

Standard atomic force microscopes detect the interaction between tip and sample based on the deflection of a laser beam reflected from the back of a cantilever on which the AFM tip is mounted, as in Figure 2.11. The reflection of the laser beam obeys Snell's law—the angle of incidence is equal to the angle of reflection when the index of refraction is the same throughout the light path—thus the angle at which the reflected beam hits the detector

depends on the angle of the cantilever back surface with respect to the incident laser beam. The force between the tip and the sample can be calibrated using the spring constant of the cantilever, determined by observing the resonance frequency of the cantilever when it is just subject to Brownian motion, and taking a "force curve," watching the deflection of the cantilever as the tip is brought from far away from the surface to the point where it firmly touches the surface and then is retracted away [42].

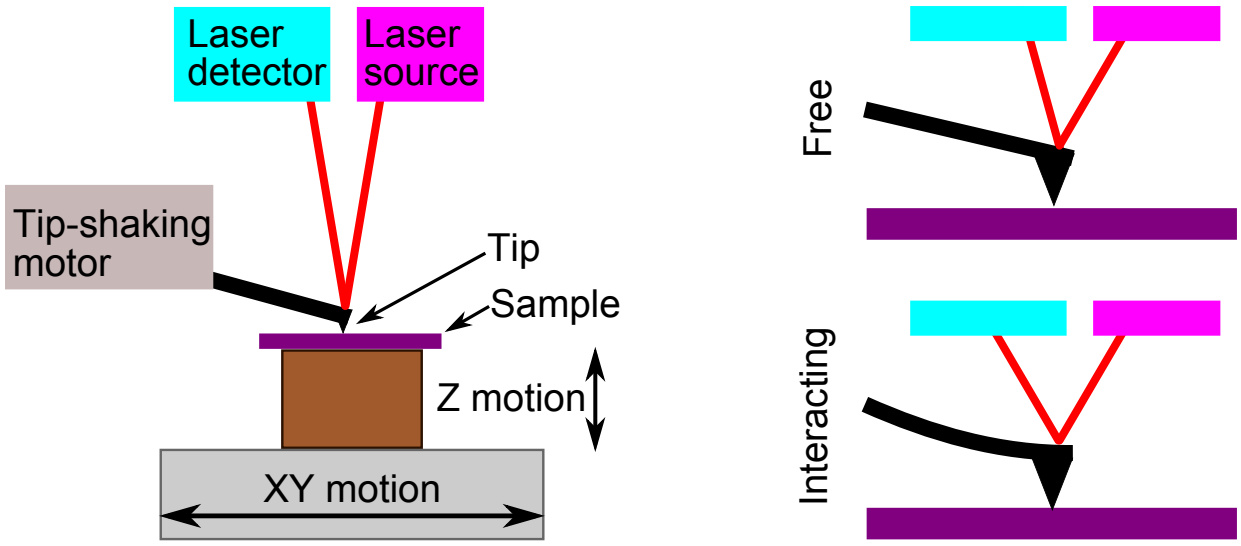

Figure 2.11: Diagram of an atomic force microscope. The tip is at the end of a cantilever; deflection of a laser reflected off the back of the cantilever is proportional to the cantilever bending. Left: Schematic of AFM hardware. Right Top: When the tip is free of the surface, the deflection of the reflected laser beam is determined by the angle at which the cantilever is mounted and, if operated in amplitude modulation mode, the angle of the cantilever at that point in its oscillation. Right Bottom: When the tip is interacting with the surface, an additional deflection due to forces from tip–sample interactions is added.

Tapping mode atomic force microscopy, also called "AC mode" or "amplitude modulation" or "intermittent-contact" AFM, is the most commonly-used AFM mode today. The cantilever is driven at or near its resonance frequency. The feedback acts on the amplitude of the cantilever's oscillation, as determined by the deflection of the position of the laser beam reflected off the back of the cantilever, as detected in a postion-sensitive photodetec-

tor. When the tip interacts with the sample, this dampens the oscillation of the cantilever, thus the atomic forces from the sample affect the amplitude of the cantilever's oscillation, which provides the data-giving signal. Contact mode, where the tip moves along the sample surface in almost the exact same fashion as a record player needle moves along the record, was not used for AFM imaging in this experiment because the tip was prone to pushing the pili laterally around on the surface when operated in this mode.

Amplitude modulation AFM can be likened to dribbling a basketball. The feedback mechanism for the basketball player is the amount of force needed to maintain the ball at the same height when it bounces back. Similarly, the feedback mechanism for amplitude modulation AFM is the amplitude of the sinusoidal voltage signal applied to the piezoelectric element controlling the cantilever and tip motion in order to make it oscillate. The damping of the amplitude, the need to apply more driving force to make it reach the desired height or "setpoint" amplitude at the top of its oscillation, gives information about the properties of the surface with which it is interacting. If one dribbles a basketball down a set of stairs, one finds that one must apply more force to the ball to make it rebound to the same height. Similarly, the AFM signal gives information about the height of features on the sample. Dribbling a basketball in the mud instead of the driveway requires more force and delays the basketball in its return to its setpoint height; similarly, the AFM "phase" signal gives information about the relative softness or the adhesion of materials. In this work, the phase signal was useful for ascertaining the location of the biological material on the hard substrate.

With these scanning probe microscopy techniques in hand, specific implementations of these microscopes (discussed in Chapter 3) can be used on the pilus nanowires expressed by *Geobacter sulfurreducens* (discussed in Chapter 4) to gain information about the density of states of that system at ambient and cryogenic temperatures (discussed in Chapter 5).

Chapter 3

Details of Experimental Apparatus

Moving from the general principles in Chapter 2 to specific instrumentation, this Chapter presents an overview of the experimental equipment used in this research. The cryogenic-capable scanning tunneling microscope used for this study was built at Michigan State University by Sergei Urazhdin and Aleksandra Tomic and operated using an RHK SPM 100 controller. While some of the research discussed here was done at room temperature, the majority of the data came from measurements taken with the microscope and sample immersed in liquid nitrogen. Additional room temperature topography was obtained using a Cypher scanning probe microscope in STM and AFM modes.

3.1 STM Hardware Configuration

A plethora of strategies and philosophies are used in the design of scanning tunneling microscopes. The cryogenic-capable STM used here followed the design developed by Besocke *et al.* [43, 44] for tip–sample coarse approach, chosen for its thermal compensation and noise-resistant qualities, since the microscope was designed for cryogenic experiments.

3.1.1 Besocke Design

The Besocke, or beetle, STM design [43] was selected for the microscopes in this laboratory because of its superior thermal compensation. Since all the piezotubes (discussed further

in Appendix D) in the microscope are the same size and are mounted on the same structure, they expand or contract identically with temperature changes. Because the piezotubes supporting the sample and, separately, the tip, are all mounted on the same rigid base, microscope vibrations affect them all equally, which makes the design vibration-resistant as well [30]. The "business end" of the cryogenic-capable STM used here is shown in Figure 3.1.

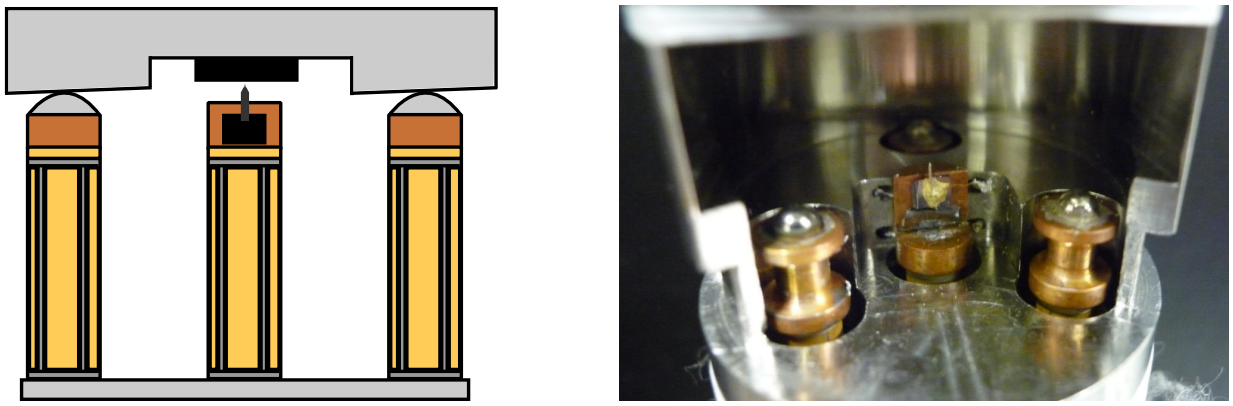

Figure 3.1: Besocke-design STM with ramps. Left: Schematic of the design. Right: Photograph of the microscope with no ramps in place. The caps atop all three "walking" piezotubes can be seen, as well as the "scanning" piezotube in the center on which a tip is mounted.

The coarse approach between the tip and the sample in this design uses inertial translation to advance or retract the sample, which is mounted on a set of ramps [44]. Essentially, the overall shape of the sample motion is screw-like. The process of inertial translation is shown in Figure 3.2. A voltage is applied to the "walking" piezotubes, causing them to bend like an elephant's trunk; the ramps, supported by the stainless steel balls atop the walking piezotubes, are rotated gently by this motion. The voltage on the walking piezotubes is then abruptly returned to zero, causing the walking piezotubes to snap back to their equilibrium position. This occurs so quickly that the ramps are no longer in contact with the walking piezotube caps and don't move, as in the magician's tablecloth trick. This means that a

different part of the ramps then sits atop the stainless steel balls summiting the walking piezotubes, which corresponds to the ramps advancing or retreating a small amount.

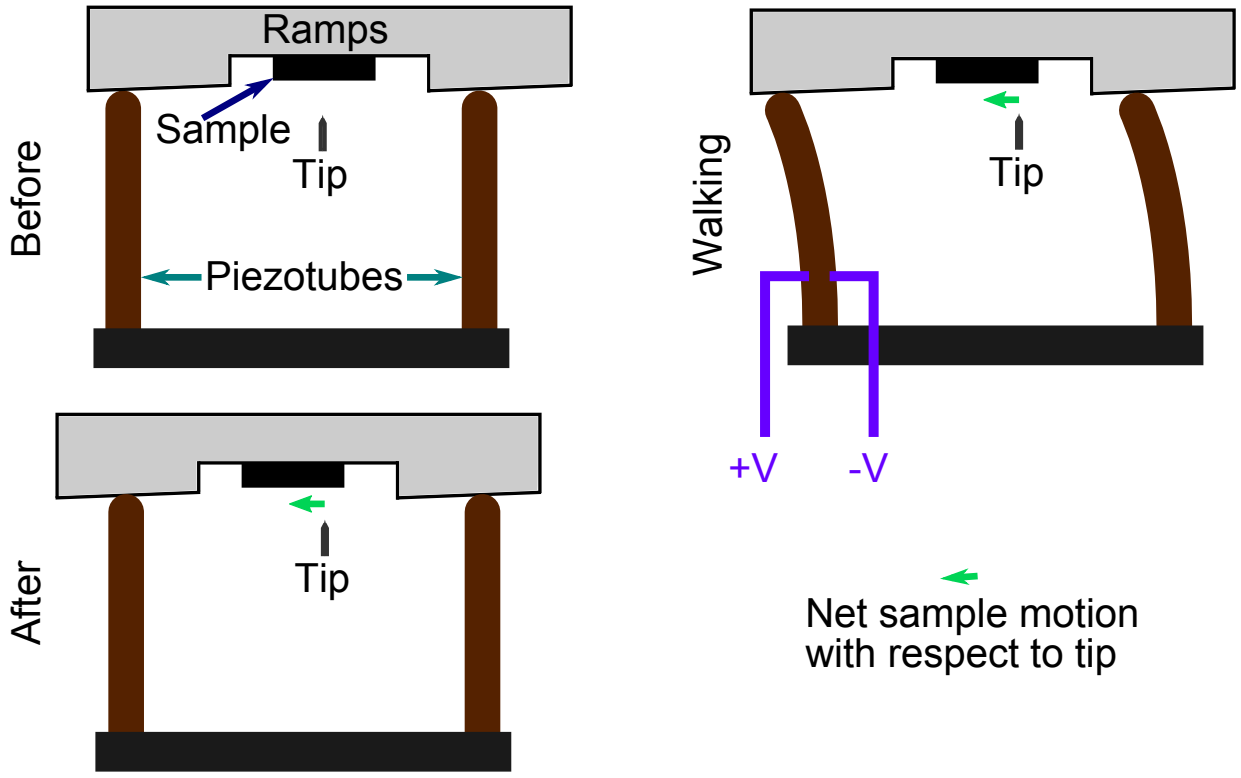

Figure 3.2: Diagram of the inertial translation process, shown in two dimensions and applied to a lateral translation for simplicity of demonstration. Motion is exaggerated for visibility. A voltage is applied to the quadrants of the walking piezotubes, causing them to bend while they carry the ramps on their tops. The voltage is then suddenly switched off, causing the piezotubes to straighten up again while the ramps and sample retain the offset.

Micrometer-scale sample translation in the lateral (X,Y) directions was also performed via the inertial translation, or stick–slip method, as shown in Figure 3.2. By this process, several square millimeters of the sample could be probed, although experiments generally ended due to irrecoverable tip damage before this much area could be scanned. This method does not necessarily result in reproducible translations over many-micron distances, since there is some variance in the motion due to the interplay between sample lateral and z motion and to slight irregularities on the ramps. Nanometer-scale offsetting of the scanning

region was done by applying lateral offset voltages to the scanning piezotube quadrants.

3.1.2 Tip Specifics

STM tips must be made of conductive material that does not form an insulating oxide layer on any timescale during which the experiment would be performed and which preferably has a simple, or at least known, density of states so that states in the tip do not obscure states in the sample. The tips used for this experiment were an alloy of platinum and iridium in an 80:20 Pt:Ir ratio. This is a conventional material, frequently used for STM tips, possessed of these desired characteristics.

To obtain good resolution, it is important to have tips with apexes which are sharp on the atomic scale. This can be achieved a not inconsiderable fraction of the time by cutting the tips mechanically with a pair of diagonal cutters. For optimal cutting, the wire should not be entirely severed by the cutters, but rather the cutters serve to weaken the wire while a pulling motion applied to the cutters stretches the wire until it breaks. The procedure used to cut most of the tips used in this experiment is demonstrated in Reference [45].

After mechanically cutting the STM tip wire, tips were affixed to mounting chips before being loaded onto the cryogenic-capable STM. A mounted tip is shown in Figure 3.3. The mounting chips were made from standard silicon wafers cleaved to be a few millimeters on a side; silicon chips were used to prevent electrical shorts between the tip and the cap of the scanning piezotube, upon which the tip chip was to be mounted. A small amount of cryogenic-compatible conductive epoxy was dabbed onto the chip. A piece of thin gold wire, to be used for connecting the tip to the coaxial tunneling current wire at the microscope, was cut and lain into the epoxy, then the tip was lain into the resulting epoxy cushion. After curing the epoxy, the tip chip was affixed to the cap of the scanning piezotube and the gold

wire was soldered to the coaxial tunneling current wire using indium solder. In this way, the tip and tunneling current wire were electrically connected.

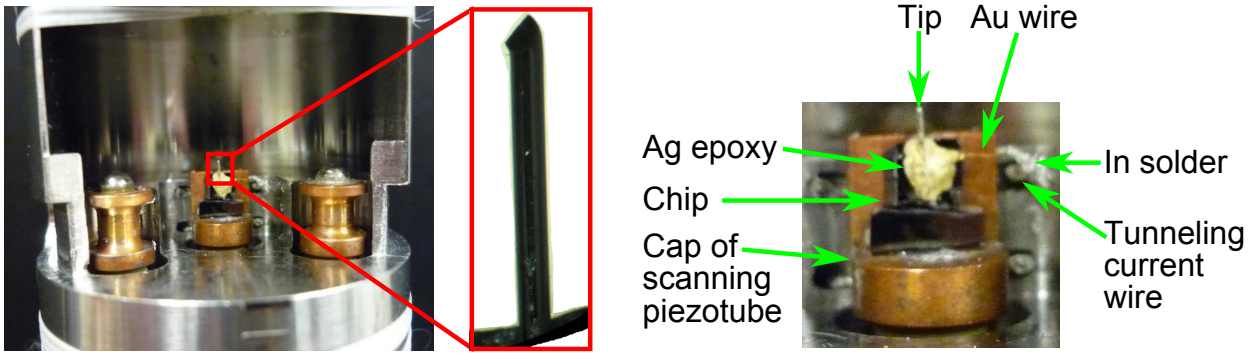

Figure 3.3: An STM tip in place on the microscope. Left: Photograph of a mounted tip. Center: Optical microscope photograph of Elizabeth, the tip used to acquire the clearest low-temperature data. The radius of curvature of the apex of a good STM tip is only a few to a few tens of nanometers, so the apex is not visible via optical microscopy. Right: Labeled components of a mounted tip.

3.1.3 Vibration Isolation

It is traditional in scanning probe microscopy measurements to suspend or support a microscope using a heavy mass and a soft spring, such that the resonant frequency of the microscope and support is far below that of typical excitations due to building vibrations. Extensive vibration isolation systems are not always necessary. For example, atomic resolution of the graphite lattice was routinely obtained using the portable EasyScan STM when it was placed on a sturdy table, including in a high school classroom during an outreach event, as shown in Figure 3.4. The commercial EasyScan STM is mounted on a heavy, marble slab with vibration-damping soft feet beneath. For the research done with the cryogenic-capable STM, the microscope was mounted on a helium storage dewar, discussed in more detail below in the context of cryogenic operations. This dewar was filled with liquid nitrogen for the 77 K experiments, for which experiments the microscope was lowered into the dewar.

For room-temperature measurements, the microscope was mounted atop the floor-secured dewar for mechanical stability purposes. The wheels of this portable storage dewar were secured with cardboard shims wedged beneath them and duct tape adhering them to the floor in order to stabilize the dewar. Sufficient vibration isolation was attained with this arrangement to enable atomic resolution of graphite at 77 K.

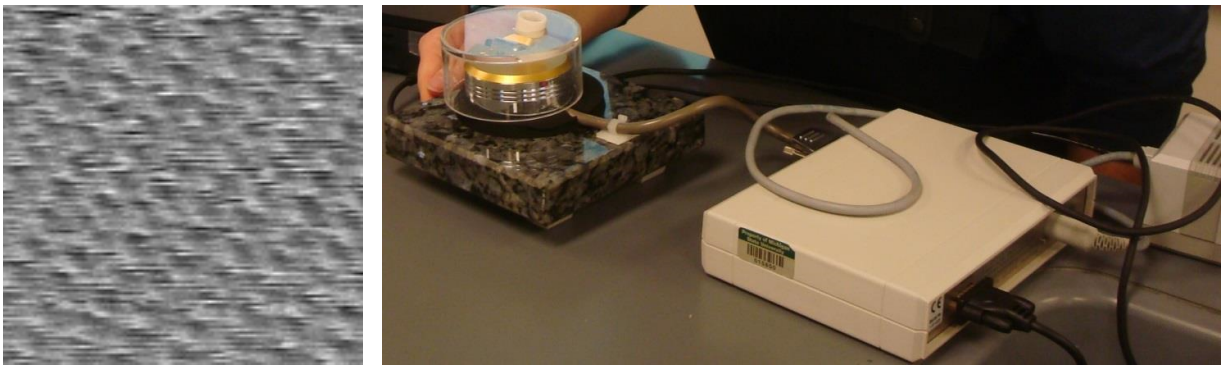

Figure 3.4: Left: Graphite lattice imaged using the tabletop EasyScan STM at an outreach event. Scan size is 1.95 nm × 1.95 nm. (+ 0.1 V, 1 nA) Right: Photograph of the tabletop STM *in situ* in a high school classroom.

3.2 STM Calibration

Due to time or applied voltage, the piezoelectric material used in the piezotubes will depolarize to some extent, that is, extend or contract less for a given applied voltage [30]. For this reason, the cryogenic-capable STM used in this study was recalibrated.

Calibration of the correspondence between voltage applied to the scanning piezotube's quadrants and actual distance in nanometers along the sample traversed by the tip in the X and Y dimensions was done on a sample of graphite at room temperature. The microscope was mounted on a dewar suspended off the ground using bungee cords to decouple it best from floor vibrations. Knowing the lattice parameters of graphite and measuring the apparent

distances between atoms in an atomic-resolution scan of graphite such as that in Figure 3.5, the conversion factors of 17.15 nm/V in the X direction and 20.88 nm/V in the Y direction were obtained. Atomic resolution STM scans of graphite only show half of the atoms on the top surface of the graphite; the bright spots in the atomic resolution image in Figure 3.5 are those atoms on the surface without another graphite atom immediately beneath them. The layers which comprise graphite are stacked on top of one another in such a way that every other atom in a given sheet is atop an atom in the sheet below it, while the other atoms do not have a Z-direction neighbor until two layers below them. Care should be taken when performing the XY calibration via atomic resolution on graphite, lest an artifactual hexagonal pattern be mistaken for the actual lattice structure (see Appendix B and Reference [46]).

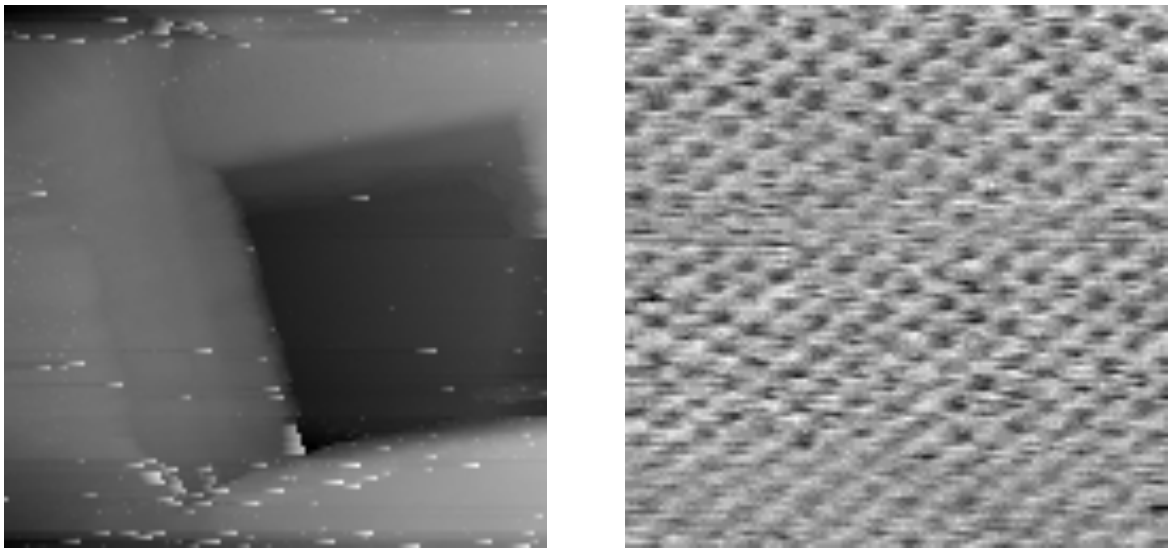

Figure 3.5: Left: Most of a platinum pit, imaged primarily to calibrate the scanning piezotube extension in the Z direction for a given voltage. The effect of a multiple tip can be seen by the inverse ziggurat shape of the pit. Streaky specks are due to particulate debris on the sample surface. Right: Hexagonal graphite lattice imaged with atomic resolution to obtain the XY calibration for the scanning piezotube. (+ 0.1 V, 1 nA)

The Z calibration was determined by scanning a grid of pits 180 nm deep etched out

of a silicon substrate and coated with platinum (see Figure 3.5), giving a Z calibration of 4.60 nm/V. To check the Z calibration, single steps of graphite were observed and checked against the literature values for graphite layer spacing [47].

3.3 Cryogenic Temperature

STM and, particularly, spectroscopy experiments were done primarily at 77 K, liquid nitrogen temperature. These measurements were done with the microscope submerged in a dewar capable of containing liquid helium but used in this instance with liquid nitrogen. The dewar was on wheels with taped cardboard shims for balance and stability, as seen in the apparatus photographs in Figure 3.6. After initially pumping out the microscope and stick area to a vacuum on the order of a few to tens of microtorr, the microscope and stick area were backfilled with nitrogen gas to act as an exchange gas for temperature equilibration. The microscope was slowly lowered into the dewar while monitoring the microscope temperature with an Allen-Bradley carbon resistor thermometer [48, 49] to ensure that thermal changes were gradual enough to prevent microscope damage.

When cooled to 77 K, the range of the piezoelectric elements in each direction decreases by a factor of approximately 3 [30]. In order to determine this factor with more precision, atomic resolution images of graphite were obtained at 77 K, and the XY calibration was redetermined at this temperature. Using the known spacing between points on the graphite lattice of 0.246 nm [47], conversion between apparent and actual atomic spacings gave a thermal contraction conversion factor

$$\textit{actual} \text{ distance at } 77 \text{ K} = 0.356 \times \textit{apparent} \text{ distance} \tag{3.1}$$

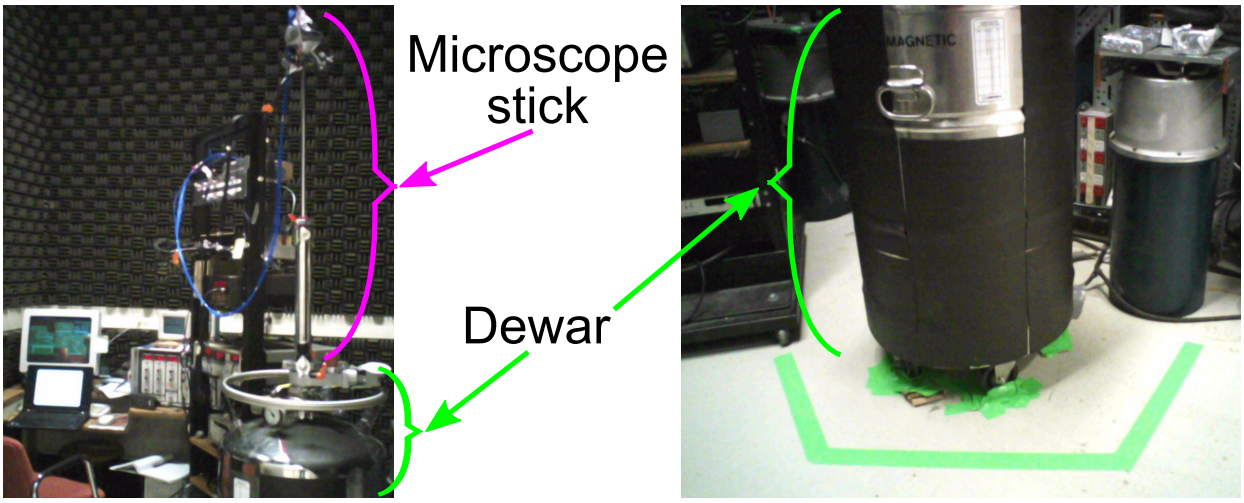

Figure 3.6: Left: Data acquisition setup for STM and spectroscopy. The microscope is at the bottom of the long stick and is submerged in the dewar (partially submerged, in this example). The dewar extends below the bottom edge of the photograph. Right: Lower part of the dewar, showing the shims and adhesive used for stability. The bright green tape is a safety measure to warn passersby against bumping into the apparatus.

under the fair assumption that thermal contraction affects all directions of the piezotube equally.

3.4 Cypher Scanning Probe Microscope

Further room temperature measurements for verification of the STM and spectroscopy results, as well as AFM investigations of topography and deposition characteristics, were performed using an Asylum Research Cypher scanning probe microscope. While the Cypher is predominantly used as an atomic force microscope, it is capable of a variety of scanning probe measurement techniques, including STM and basic point tunneling spectroscopy.

3.4.1 AFM

Observations were made of the pili deposited on different materials such as gold and thermally-oxidized silicon using amplitude modulation atomic force microscopy. This is referred to by

Asylum Research for their equipment as "AC Mode." This mode can work in either the non-contact (soft tapping) or intermittent-contact (hard tapping) regimes for interacting with the surface. Most of the AFM topographic images, such as those seen in Figure 3.7, were obtained using intermittent-contact scanning which, while interacting more strongly with the sample surface, gives higher resolution of the sample topography and more accurate determinations of feature widths. The AFM tips used for this imaging had cantilever spring constants of nominally either 2 N/m or a few tens of N/m.

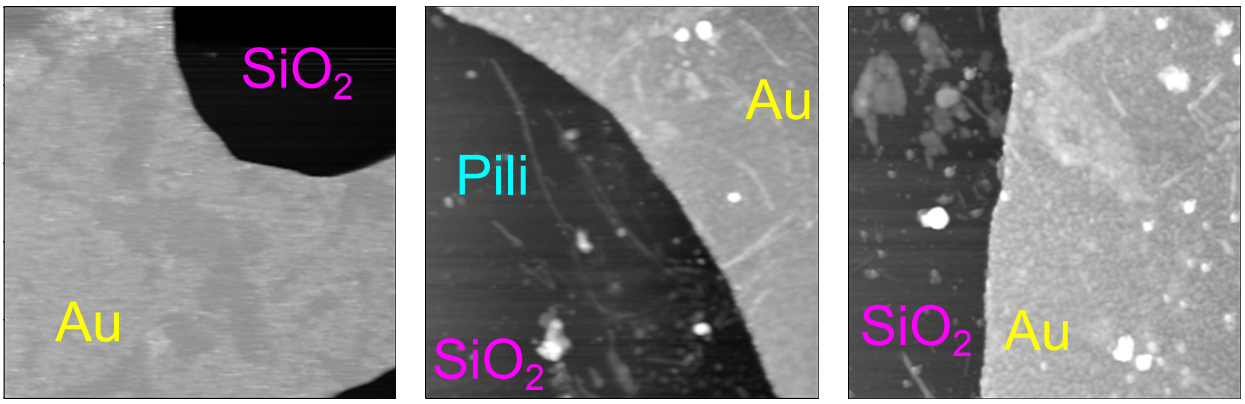

Figure 3.7: AFM topographs obtained using the Cypher. Fabrication of these samples is discussed in Appendix E. Left: 10 μm $\times$ 10 μm scan size. Center: 4.5 μm $\times$ 4.5 μm scan. Right: 5 μm $\times$ 5 μm scan. All scans shown here have a z range grayscale extent of 55 nm.

3.4.2 STM

The implementation of STM on the Cypher, as of software version 111111 which was the stable version at the time this research was performed, did not allow some of the most useful conventional methods of STM tip recovery but had a far faster tip change procedure compared to the cryogenic-capable STM. The tip holder could be removed, the tip could be recut or replaced, and the tip holder could be repositioned all within two minutes. By contrast, tip replacement on the cryogenic-capable STM took longer, generally on the order

of fifteen minutes, predominantly because of soldering time and logistical considerations. This is not solely a matter of convenience; it is also desirable to minimize the amount of time the sample spends outside of the inert nitrogen atmosphere.

There are a few main advantages of the cryogenic-capable STM over the Cypher STM. The Cypher enclosure, while it can be purged with nitrogen, cannot be pumped out to achieve vacuum. This means the nitrogen atmosphere is achieved through mixing and displacement of the ambient air inside the enclosure, which is slower than pumping out the air and replacing it with nitrogen gas, as was done with the cryogenic-capable STM. Similarly, it cannot be cooled to cryogenic temperatures. This means that this complete temperature-dependence study could not have been performed using the Cypher. Furthermore, the numerical dI/dV curves were often prohibitively noisy. Consequently, the room temperature dI/dV curves obtained using the cryogenic-capable STM were more useful than those obtained using the Cypher STM. Partially counterbalancing these disadvantages, the Cypher STM tip change procedure is fast, as previously mentioned, and requires neither epoxy nor soldering. Additionally, the sample can be moved more reproducibly over longer distances, leading to improved sample positioning.

3.5 Overview of Sample Preparation

A brief description of sample preparation for the experiments presented in Chapter 5 is given here. For a more detailed discussion of the sample preparation, including refinement of the deposition protocol, see Appendix C.

Geobacter pili were purified by Dr. Sanela Lampa-Pastirk of the MSU Department of Microbiology and Molecular Genetics. 10 microliters of a suspension of purified pili in doubly

deionized water were deposited on a freshly-cleaved graphite substrate. The substrate was mounted on a stainless steel disk attached to stainless steel ramps, discussed above in the context of sample translation, in order to deliver bias voltage to the sample. After leaving the droplet to physisorb onto the surface for ten minutes, the droplet was wicked dry. Two sequential rinses of 10 μL of doubly deionized water were deposited onto the surface, left for five minutes, then wicked dry. The sample was then dried under a stream of nitrogen gas. Despite this, the sample remained slightly hydrated due to the persistence of water on surfaces [50]. Although the experiments were not done in solution, the samples were most likely covered with a few-nanometer layer of water [50], resulting in a hydrated environment relevant to the natural state of the protein.

Chapter 4

Biological and Theoretical Context

To provide context for the measurements presented in Chapter 5, it is important to have a basic understanding of the pilus structure of *Geobacter sulfurreducens*. The structure of the pilin subunit plays an important role in determining the density of states of the entire pilus. To this end, density functional theory calculations performed by Professor Gustavo Feliciano on the *Geobacter* pilin are introduced for comparison to the measured dI/dV results.

Geobacter sulfurreducens is an anaerobic bacterium initially discovered in hydrocarbon-contaminated near-surface sediments in Oklahoma in 1994 [10]. The bacterial cell itself is two or three micrometers long and approximately 0.5 μm wide [10]. As part of its respiration, it breaks up substances such as acetate and develops an excess of electrons internal to the cell. If the cell membrane is in direct contact with an electron acceptor in the environment, this excess charge can be transferred through the cell membrane into the electron acceptor. If the cell is not in direct contact with an electron acceptor, for example if it is a cell stacked in the middle of other cells in a biofilm or if the only available electron acceptors are insoluble and far away, it must find other methods of ridding itself of these excess electrons. If electron shuttles, molecules which serve as intermediaries by diffusing through the environment, becoming reduced by bacteria, and in turn reducing other electron acceptors in the environment [17], are present in the environment, *Geobacter* will take advantage of them [18], but *Geobacter* does not produce its own electron shuttles [19]. Instead, *Geobacter* grows electrically conductive type IVa-like pili to contact electron acceptors in its environment.

The aim of this overall research program is to investigate the electronic properties of these pili both from a materials science perspective and to address biological questions about the mechanisms of long-range electron transfer through conductive proteins. This line of inquiry is pursued in this work through investigation of the electronic structure of these pili.

4.1 Pili Expressed by *Geobacter sulfurreducens*

Like other Gram-negative bacteria, bacteria which have a membrane outside of their cell wall, *G. sulfurreducens* grows type IV pili [26]. Unlike many such pili found in other organisms, but not uniquely, the pili that *G. sulfurreducens* grows are electrically conductive, both along their lengths [25] and transversally across the diameter of the pilus [3], which is the subject of the research described here. In other bacteria, pili with similar structure are used for propulsion or anchoring or for gene transfer between bacteria [20]. *Geobacter* appears to use its pili primarily for electron transfer, to attach the cells to electron acceptors [3], and to link cells together to stack in sturdy biofilms [21]. Additionally, *Geobacter* and similar species [4, 5] use these pili for electron transfer to spatially-distant electron acceptors. These pili grow up to many microns in length and are formed from pilin subunits polymerized by a molecular motor in the cell membrane and assembled into a helical pilus.

4.1.1 Pilus Structure

Pili are composed of subunits, called pilins, which interlock with one another in a helical structure, generally with four pilins per coil of the helix; each coil repeats every approximately 4 nm [51]. The pilins are assembled by the bacterium in its inner cell membrane and pushed through a pore in the outer cell membrane, through which they can then be retracted and

disassembled again to recycle the pilins, if so desired by the bacterium, at considerable speeds—for the structurally similar, but electrically insulating, *Pseudomonas aeruginosa* pili, at rates of approximately 0.5 μm of pilus extension or retraction per second [6]. Figure 4.1 shows an artist's rendition of individual pilins being inserted onto an assembled pilus. Each bacterium can produce multiple pili, particularly when grown under conditions with a large fuel source and limited access to electron acceptors in the environment. A single pilus is sufficient to discharge a *Geobacter* bacterium [24, 25] if it can contact an electron acceptor.

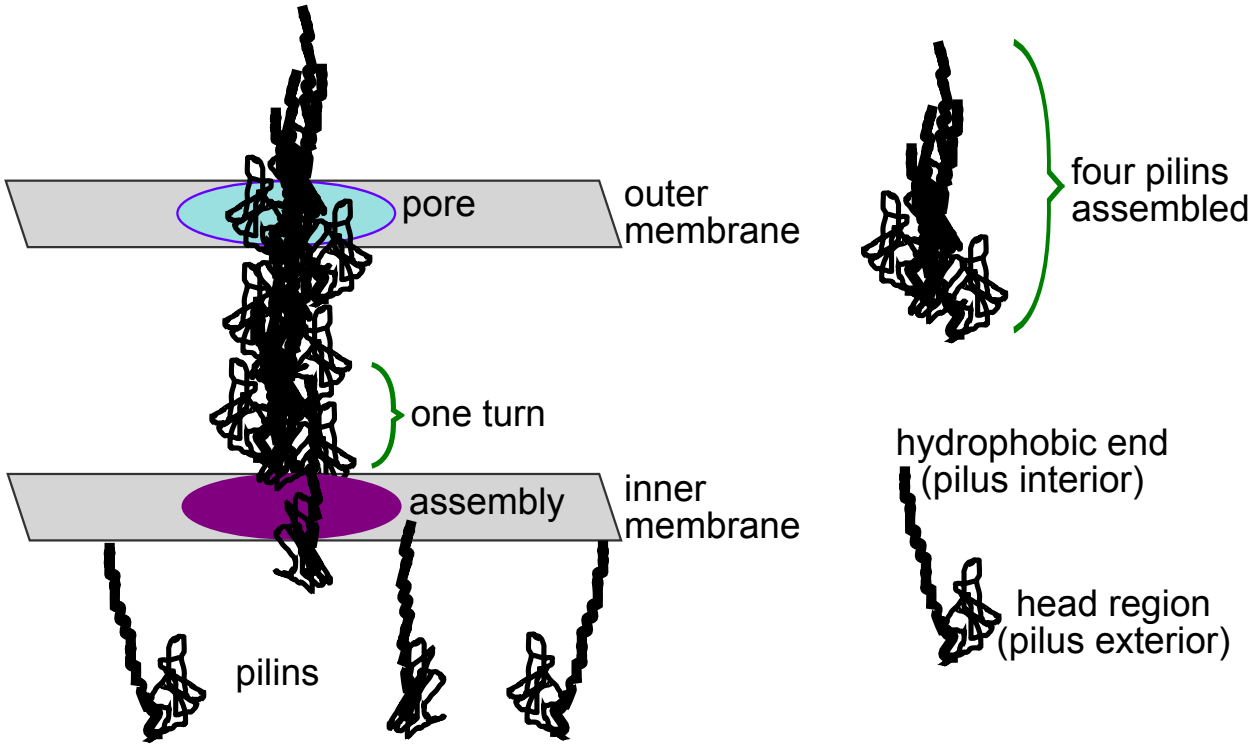

Figure 4.1: Artist's conception of pilus assembly and extension at the cell membrane, inspired by and simplified from [6]. For simplicity, proteins are represented schematically. Pilin subunits dispersed throughout the inner membrane area are assembled by another protein into a helical structure, then pushed through a pore in the outer cell membrane. The hydrophobic center of the assembled pilus is a tube formed by the long α-helices of the pilins, leaving a hollow core to the pilus, and the heads of the pilins remain on the outside of the pilus to interact with its environment. In *Geobacter*, the globular head which other pilins have is replaced by a short, barb-like shape [8, 52, 53].

The structure of the individual pilins has very recently been solved using NMR [52, 53],

but it is primarily known through theoretical studies [8, 54]. In contrast to other type IVa pilins, which are a close analogue to *Geobacter*'s pilin structure, the pilin subunit of *G. sulfurreducens* pili does not have a large globular head but instead has only a small barb protruding at an angle from the α-helix comprising most of the body of the pilin, as seen in Figure 4.2, which is based on the published coordinates of the theoretically calculated structure from Reference [8]. Because it is not obstructed by a large globular head, the pilin's native dipole moment remains discernible (the positive part of the dipole is inside the assembled pilus), although that is modified somewhat by the surrounding water in its environment [8].

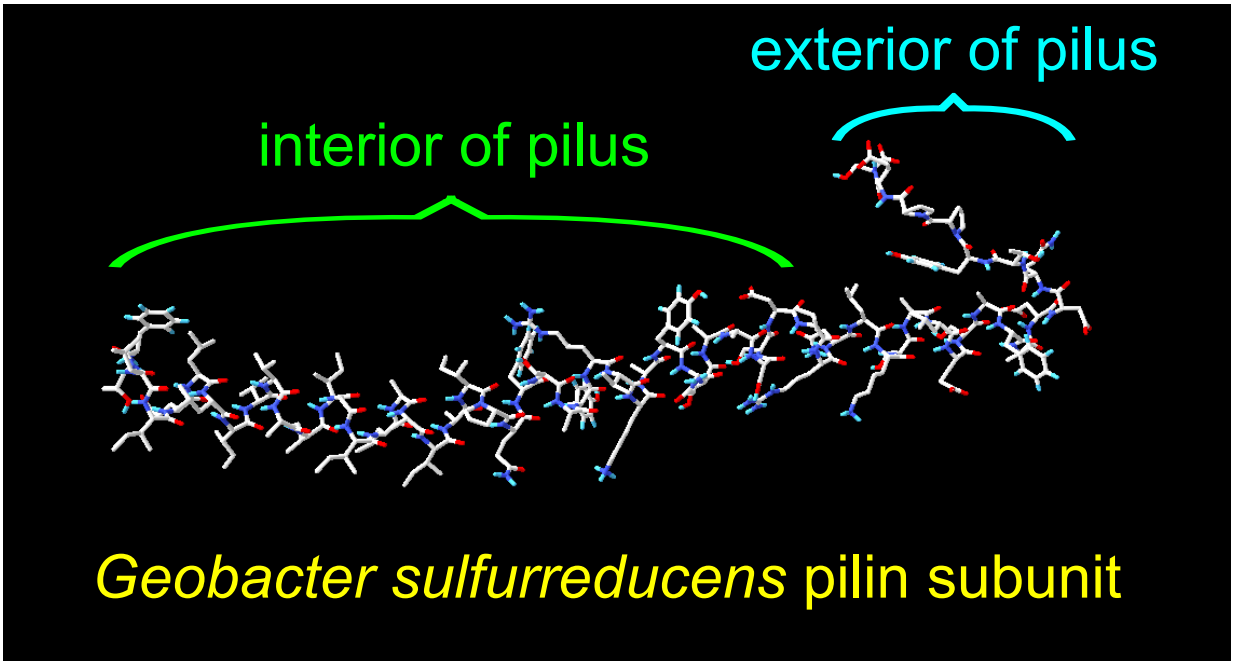

Figure 4.2: Structure of the *G. sulfurreducens* pilin subunit based on a homology model. Coordinates were obtained from Reference [8] and displayed using DeepView (Swiss-PdbViewer) version 4.1.0 [7]. The α-helix tail of the pilin is buried inside the assembled pilus, while the small barb-like head remains on the outside of the pilus.

A recent study which used NMR to determine the *Geobacter* pilin structure at room temperature in solution [52] determined several relevant properties of the pilin which may even-

tually shed considerable light on the specific pathway of charge transport through *Geobacter* pili. Two parts of the pilin in particular were found to be rather flexible—NMR measurements are averages over ensembles of many molecules, so they explore the physical configuration space of the molecules, and this measurement observed a variety of relative angles between the barb and the α-helix.

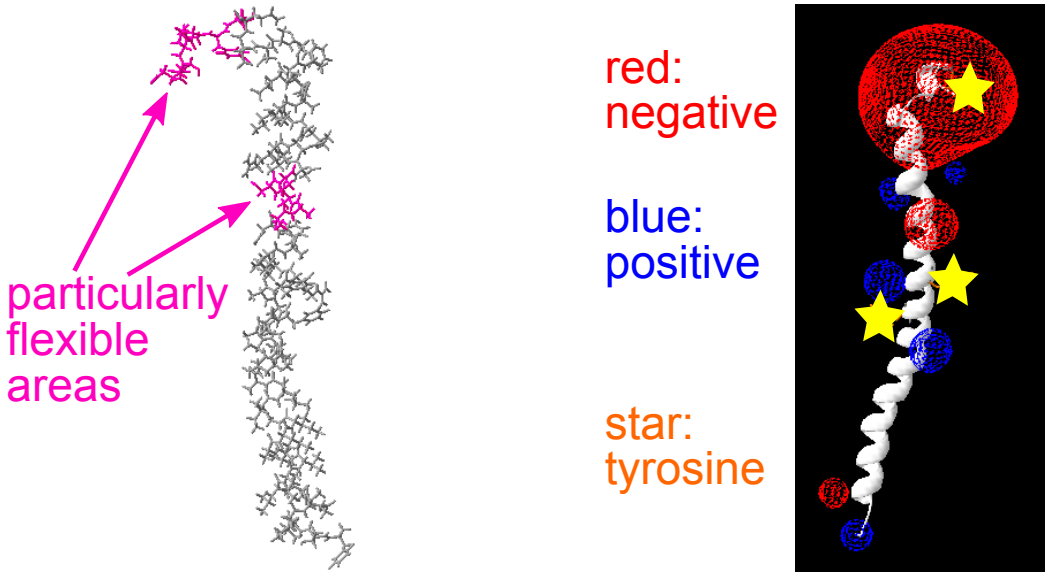

Figure 4.3: Structure of the *G. sulfurreducens* pilin subunit based on solution NMR [52]. Coordinates were obtained from Reference [53] and displayed using Swiss-PdbViewer [7]. Left: The NMR measurements yielded several slightly different conformations for some parts of the pilin, suggesting flexibility in these regions [52]. Right: Same pilin, viewed from a different angle. Electrostatic potentials due to charged amino acids are superimposed on the pilin structure. Electrostatic potentials were calculated in DeepView using the Coulomb interaction and assuming a dielectric constant of 80 for the surrounding medium and 4 for the pilin, as in Reference [25]. Tyrosine amino acids are marked with stars.

4.1.2 Implications of Pilus Structure for Experimental Design

Pilins have a net charge of -2e, where e is the magnitude of the electron charge, at pH 7, the nominal pH of water [8]. Type IV pili in general are known to form aggregates, or bundles, due to interactions between patches of static charge distribution on the surfaces of nearby

pili [51]. Commonly on the samples used throughout this research, pili would tend to form clumps, out of which only a few individual tendrils would extend, or to entwine with another in rope-like structures. In addition to the STM and AFM observations of large aggregates as in Figure 4.4, optical microscopy also showed the presence of even larger conglomerations of sample substance. For the experiments described here, then, it was necessary to take steps to break up such large aggregates. Suspensions of pili in doubly deionized water were stirred by pipetting the solution up and down multiple times before deposition. A general discussion of sample preparation is given in Appendix C.

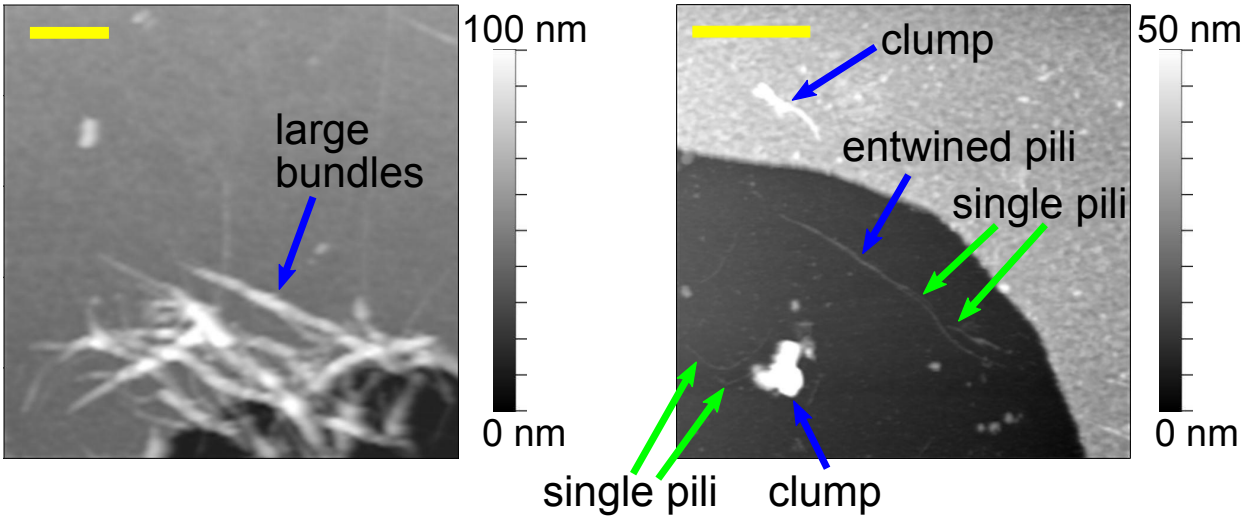

Figure 4.4: Fibrous bundles, likely predominantly composed of aggregated pili and perhaps also incorporating trapped fluid or contaminants. Left: A large "haystack" of bundles on gold, with a small region of silicon dioxide surface in the lower right corner of the image. Right: Expanded view of the image shown in Figure 1.2 showing both clumping and entwining types of bundling. Both scans are atomic force micrographs. Scale bars are 1 μm.

4.2 Charge Transport Mechanisms in Proteins

The motion of charged particles through proteins can follow different paradigms in different materials. It is not yet concretely established what the charge carrier is in *G. sulfurre-*

ducens pili, although one experiment showed increased electrical conductivity of biofilms when pH was lowered—more positively ionized hydrogen ions were added to the environment, hence attracting away electrons from the pili—suggesting that holes, rather than electrons, are the charge carriers in these nanowires [32]. Additionally, proton conduction is also a common concept in the biological and molecular chemistry electron transfer community; since positively-ionized hydrogen atoms are the smallest non-electron component of proteins, if any part of the protein structure must detach itself to move, these will be the ions to do so. In another form of charge transport seen in proteins, particularly in proteins in which tyrosine amino acids are important contributors to the charge transport [55], positively-ionized hydrogen atom (proton) motion can be associated with electron motion in charge transport in the process known as proton-coupled electron transport, in which either both an electron and a proton move at the same time or the transfer of one lowers the potential energy barrier for the transfer of the other [56]. For the purposes of this discussion, the charge carriers in pili will not be positively identified as electrons, holes, or other, but simply considered in a generic sense. Extensive speculation will not be ventured as to the nature of charge transport through the pili, since the work presented here focused most strongly on observing the electronic structure.

In the end, no matter what the underlying charge transport mechanism is in the pili, STM and tunneling spectroscopy are sensitive to the density of states at the tipwards surface of the protein, so many of the transport-related details will not impact the measurements discussed here. The chief observable result of different charge transport mechanisms in proteins in these measurements is due to the temperature-dependence of the study; at 77 K, the temperature-dependent transport mechanisms will contribute much less to the available energy levels at the protein's surface than they would at 300 K. Density of states experiments like those

presented here give information about the available energy levels in a sample; transport measurements would address *how* the charge carriers would reach those energy levels.

4.2.1 Tunneling

One way in which charge carriers can move from site to site through a protein is by means of quantum tunneling through the potential barriers between sites. This process does not depend on the temperature of the system, provided that the barrier is high enough or the temperature is low enough that the thermal energy does not allow the charge carriers to travel "over" the barrier in the classical sense and they must instead tunnel "through." This does not include superexchange, or thermally-assisted tunneling, which is in part a temperature-dependent process. Since the probability of tunneling depends exponentially on distance, this process is limited to short distances on the order of the diameter of the pilus. Single-step tunneling across 2 nm distances is not overly improbable but instead is a biologically-relevant process [57]. Since the diameter of the pili is on the order of this value, it is not beyond belief that a pure tunneling pathway could exist between "top" and "bottom" of the pilus breadth.

4.2.2 Temperature-Dependent Charge Transport

Multiple mechanisms for charge transport through proteins exist which can be "helped along," or even made at all feasible, with the addition of thermal energy from the environment. This can either provide the charge carriers with enough energy to "hop" over potential barriers between sites on the protein (charge hopping) or, by providing virtual intermediate states, extend the range of distances over which tunneling processes can occur

(superexchange, or thermally-assisted tunneling). In many proteins upon which temperature dependence of conductivity studies have been performed at room and cryogenic temperatures, charge transport rates decrease upon cooling of the protein to cryogenic temperatures [58]. By contrast, increased conductivity of a different protein electron transfer system upon decrease in temperature to 170 K was attributed by the authors of that study to the protein compactifying when it was cooled [57]. This serves as a reminder that many factors, not least including protein conformation changes with temperature, can contribute to the conductivity through these systems. Since proteins are generally less stable in their structure than most traditional metallic or semiconducting nanowires—in ambient conditions, protein structures often fluctuate slightly—the transport properties depend in part on the protein structure *at a given temperature*.

Recent work from Malvankar *et al.* proposes a model by which *G. sulfurreducens* nanowires are conductive in the same way as a metal is [32], where the charge carriers are delocalized, in contrast to the charge transfer mechanisms discussed above, wherein charges move from locale to locale through the nanowire. This is based on observations of increased conductivity through *G. sulfurreducens* biofilms and mats of purified pili similar to those shown in Figure C.2 as the temperature was lowered to 200 K, which the authors interpret as evidence that charge carriers were able to move for greater distances without scattering off of phonons from room temperature heating of the pili [32].

Since these temperature-dependent charge transport mechanisms are multitudinous in form and are significantly decreased in relevance at the cryogenic temperature of most interest to the research presented here, the following discussion generally considers them generically as temperature-dependent processes rather than delving into the details of the specific temperature-dependent charge transport mechanism(s) involved in pilus conductivity.

4.2.3 Marcus Theory

Charge transport through pili can be, at least to a first approximation, described by Marcus theory, which is a typical starting point for considerations of charge transport in proteins. This describes charge transport as a product of the contributions from tunneling and temperature-dependent processes. The famous "Marcus equation" is given in Equation 4.1, in terms of the electron transfer rate k_{ET}, which is proportional to the current.

$$k_{ET} = \frac{2\pi}{\hbar}|H_{DA}|^2 \frac{1}{\sqrt{4\pi\lambda k_B T}} \exp\left[-\frac{(\lambda + \Delta G^0)^2}{4\lambda k_B T}\right] \tag{4.1}$$

In this equation, $|H_{DA}|$ describes the coupling of the donor and acceptor, which, in this case, would be different components of the pilus. The tunneling part of the Marcus equation, $\frac{2\pi}{\hbar}|H_{DA}|^2$, is independent of temperature, neglecting any conformational changes to the pilus, thus it will underlie both the 77 K and the room temperature conductivity in the system studied here. In contrast, the latter part of the Marcus equation, all that is not tunneling, depends strongly and explicitly on temperature.

At room temperature, akin to the natural thermal environment of the pili when attached to living bacteria, both tunneling and temperature-dependent processes can contribute to the conductivity of the pili. In order to determine whether tunneling is a meaningful contributor to the conductivity, a substantial change in temperature is necessary. Cooling the pili reduces the contribution of temperature-dependent processes to the overall conductivity but does not affect tunneling. This simplified description neglects conformational changes which may change the distances over which tunneling would occur.

Besides temperature, the adjustable parameters in the Marcus equation are the reorganization energy λ describing the energy needed for the nearby charges in the protein and

in its surrounding water to move to accommodate the new electrostatic scenario once the charge has transferred [56] and the driving energy of the reaction ΔG^0. For the purpose of this temperature dependence estimate to investigate implications for the research program discussed here, the reorganization energy λ is taken to be a constant of temperature. If the reorganization energy increases upon cooling, the effect of cooling on the significance of temperature-dependent mechanisms will become even greater. The value of 0.2 eV for λ used for this estimate is obtained from a study on *Shewanella oneidensis*, a similar organism which produces more or less similar protein nanowires [59]. The free energy ΔG^0 is taken to be zero, since it is small compared to λ in the discussion of *Shewanella* nanowires [59]. Note that k_BT is 25 meV at room temperature and 6.6 meV at 77 K. It has long been known and shown that freezing proteins to cryogenic temperatures changes the reorganization energy and the free energy driving the charge transport reaction [60]. Thus in addition to the explicit temperature dependence on k_BT, both λ and ΔG^0 are affected by the freezing of the protein and the thin layer of water surrounding the pilus, and the free energy changes because the entropy decreases with temperature [60].

The current through the pilus is proportional to the electron transfer rate, $I \propto k_{ET}$. Therefore, with reference to Equation 4.1,

$$\frac{I_{77K}}{I_{295K}} = \frac{k_{77K}}{k_{295K}} = 0.007 \tag{4.2}$$

Thus $I_{77K} = 0.7\%\ I_{295K}$—under the aforementioned assumptions, the predicted tunneling current will be lower by two orders of magnitude at 77 K than at room temperature.

Temperature dependence studies of materials using STM and tunneling spectroscopy tend to focus particularly on systems which have some form of transition and to make small

temperature steps around that transition temperature, whether it is a transition between normal metal and superconductor [39], metal and insulator (or better-conducting semiconductor and poorer-conducting semiconductor) [40], charge (or spin) density wave behavior change [61, 62], and so forth. It is not expected that there is a discrete transition temperature at which temperature-dependent conductivity mechanisms in proteins turn off completely. Marcus theory, for example, describes a smooth decrease in temperature-dependent conductivity as the sample is cooled. Consequently, such fine-detailed temperature gradations around a transition temperature as are common in the aforementioned type of studies are not necessary, and two widely-spaced temperatures, 77 K and room temperature, are sufficent for sampling the electronic structure of *Geobacter* pili.

4.2.4 Experimental Signatures

The change in current through the pilus with temperature, estimated above using Marcus theory, could potentially affect the ability of the pilus to be conductive enough at 77 K to be imaged stably using STM. The upper limit on the resistance of an object to be imaged is set by Ohm's law, with the resistance of the sample in series with the effective resistance of the tunneling gap, as in Equation 4.3. The total resistance between the tip and the sample must be sufficiently small that the applied bias voltage will induce a tunneling current detectable by the electronics, as sketched in Figure 4.5, for values of "small" in the tens of gigaohms. Early STM studies on protein-coated DNA [63] substantiate the claim that the tunneling resistance in this type of measurement is dominated by the tip–sample gap resistance and that charge was conducted through the bulk of the protein-coated DNA, analogous to the pili in this research, rather than around the outside [63]. This suggests that pili would still be imageable using STM at 77 K, and the experiments described here would be feasible.

$$\frac{V_{bias}}{I_{tunneling}} = R_{tunneling} = R_{pilus} + R_{gap} \tag{4.3}$$

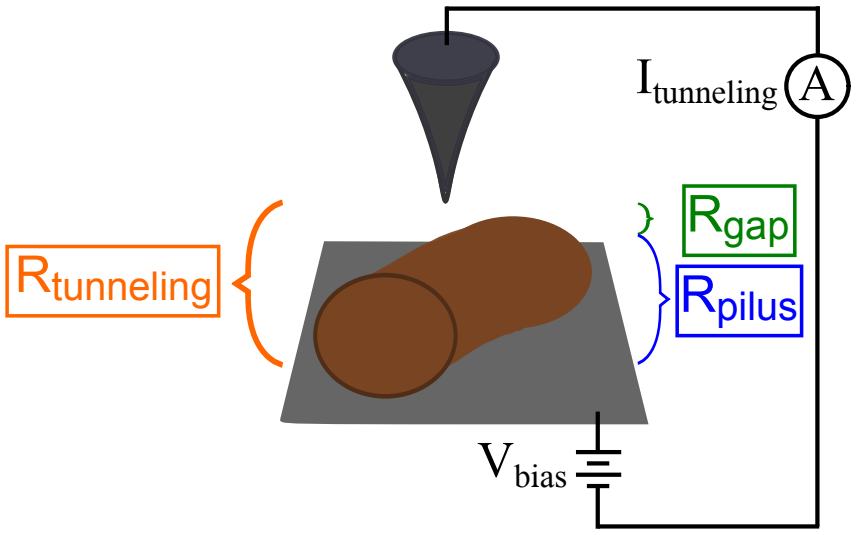

Figure 4.5: Diagram of an STM experiment on a pilus. The total tunneling resistance is the sum of the resistances of the tunneling gap and of the pilus itself.

If the temperature-dependent conductivity mechanisms are incoherent, which is likely, and thus distributed across all relevant energies set by the bias voltages in the dI/dV curves, they will contribute equally to the conductivity. This will serve to offset the dI/dV measurements uniformly up the ordinate axis at room temperature as compared to cryogenic spectroscopy, rather than to change the shape of the dI/dV curves. Since the scaling along the ordinate axis is arbitrary, with the exception of zero dI/dV, this will be essentially undetectable using this technique unless it serves to raise a cryogenic value of zero dI/dV to a value of greater than zero dI/dV. For this reason, more detailed theoretical investigations are valuable to aid in interpretation of the data.

It has long been recognized that energy levels in proteins can be treated analogously to those in more traditional condensed matter sytems [64]. At a basic level, the pilus nanowires can be treated as unified objects. Further insight into the underlying scientific processes

driving the results requires a more finely-grained treatment of pilus structure. In order to interpret the results on the sub-pilus scale, theoretical assistance was obtained from Professor Gustavo Feliciano of São Paulo State University. Dr. Feliciano performed density functional theory calculations to determine the electronic structure of a pilin subunit in order to provide insight into density of state characteristics of the pili.

4.3 Molecular Dynamics Calculations

Because of the prohibitively large number of atoms involved in the structure of *Geobacter* pilins (over 940 [8, 65] for the pilin alone, not even including surrounding water), calculations were made by Dr. Feliciano on a single pilin subunit rather than on an entire pilus. A sense of the complexity of the calculations can be gained from observing Figure 4.6. This is a snapshot of Dr. Feliciano's simulation of a *Geobacter* pilin at 77 K. The initial pilin structure coordinates were obtained from one of the experimentally-determined structures [52, 53], and it was allowed to evolve through time with periodic boundary conditions. The water molecules are deliberately faded in color in Figure 4.6 to gain visibility for the pilin, which is surrounded by water in three dimensions.

In order to calculate the density of states of the pilin under as near to the experimental conditions as feasible, Dr. Feliciano first determined the most likely conformation of the pilin, surrounded by simulated water with a small number of ions to neutralize the pilus [8]. This was done by means of molecular dynamics calculations using the GROMACS code [67]. At this point in the calculations, the temperature dependence was included. The effect of temperature on the calculated properties of the pilin was in the pilin and water conformations at the level of the molecular dynamics simulations; temperature dependence

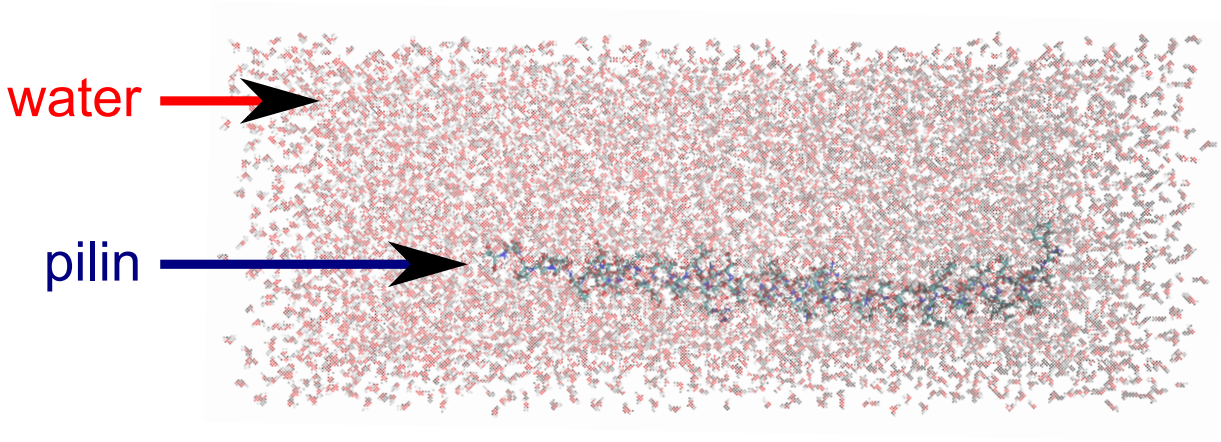

Figure 4.6: Snapshot from a molecular dynamics calculation by Prof. Dr. G. Feliciano of a *Geobacter* pilin subunit, beginning from an NMR-determined structure [53], immersed in water at 77 K. Displayed using the program VMD [66].

did not enter into the subsequent density functional theory calculations. At 300 K, the pilin structure fluctuated [8]. As expected due to the low temperature, however, the pilin did not significantly fluctuate in conformation at 77 K. Because the conformation at 77 K was similar to the multitude of conformations seen at 300 K, and because the temperature dependence of the density of states calculations depends solely on the structure as determined by the molecular dynamics simulations, this means the calculated density of states using the 300 K pilin conformation can be used also to describe the low-temperature results as well, as is done here. This suggests that further physical input to the model besides the physical structure of the pilin and its surrounding waters may need to be incorporated in order to explain the differences between the 77 K and the 300 K dI/dV measurements shown in Chapter 5.

Once the physical conformation of the pilin and its surrounding water was simulated, the electronic structure could be calculated using density functional theory.

4.4 Density Functional Theory

Density functional theory (DFT) is one of the most popular quantum mechanical calculation frameworks today, particularly popular for calculations of band structures and binding energies [68]. The name thoroughly describes the approach—everything about the ground state of a system (energy, wavefunction, and backdrop potential) is a functional of the ground state spatial number density. For simplicity, only the density of electrons will be discussed here, although the theory is more general. Occupied and unoccupied electronic states can be determined, as can excited states of the system [68]. The "density" in "density functional theory" refers to the number density of electrons in a given area. This reflects the overall wavefunction of the system, including the underlying potential describing the non-electron parts of the system which provide the context or backdrop for the electrons' experience with one another [68]. This particle number density is the "functional" in the theory's name.

The functionals themselves are properties such as the ground-state energy of the system, determined by the function chosen to describe the density of electrons in the system. For clarity of terminology, a descriptive sketch showing the density functional describing the number of electrons in a system is shown in Figure 4.7. Choosing the correct function to describe the charge density of a system, represented in the figure by "n," permits discernment of functionals of "n" which are the properties of interest.

While DFT itself is an exact theory, tractable calculations and descriptions of all but the very simplest systems require some type of approximation, in no small part because the correlations between the electrons in the calculation are not easy to pin down to a definite description. One of the most convenient formulations of these is the generalized gradient approximation. The "gradient" part of the name comes because this approximation at-

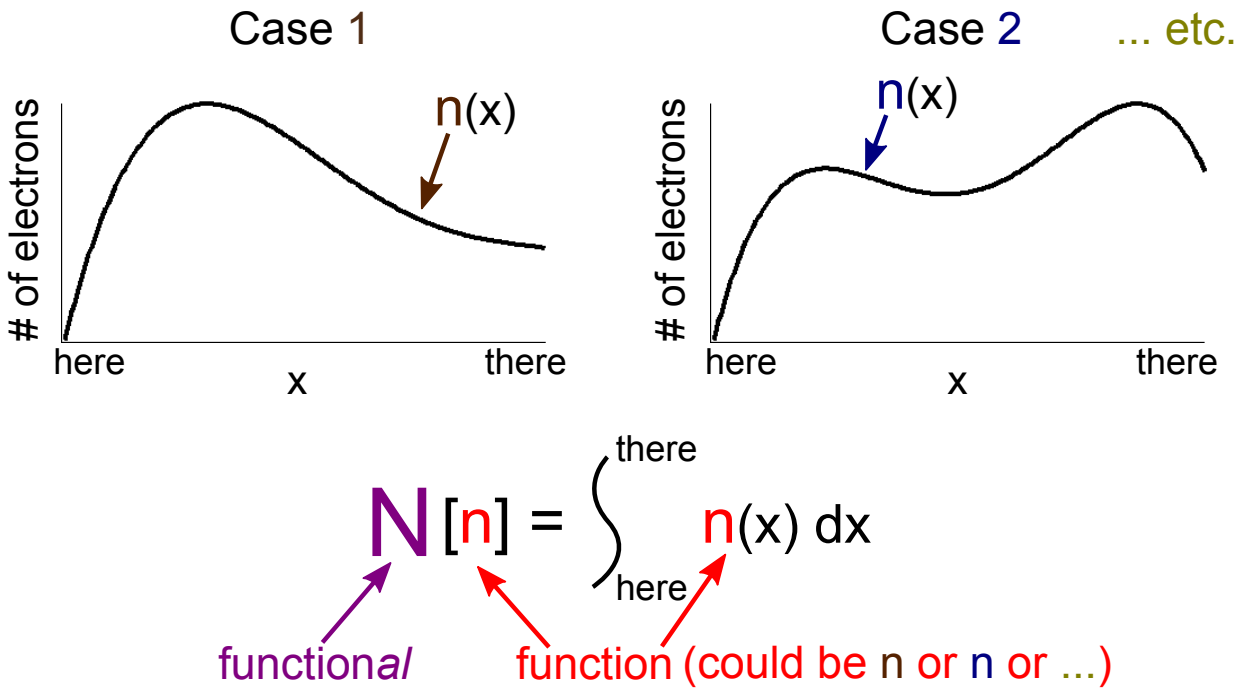

Figure 4.7: The relationship between functions and functionals. Functions have different outputs for different variable inputs describing the immediate circumstances where they are applied. Function*al*s have different outputs for different functions used to describe the paradigm of the underlying scenario.

tempts to deal with spatial variations in the electron density [68]. Density functional theory, particularly using the generalized gradient approximation (GGA-DFT), is well-known to underestimate band gaps due to difficulties treating exchange correlations [8], so calculations of the *Geobacter* pilin density of states would be expected to predict smaller gap widths than observed in tunneling spectroscopy. However, since the measured density of states of the pilus is a combination of the influences of many pilins within the vicinity of the tip, the actual measured dI/dV may rightly have a *smaller* gap than that predicted by theoretical calculations. This may come about because the detected tunneling current which may vanish due to a gap in the density of states of one pilin may be supplemented and hence nonzero by "leakage" from nearby pilins. The density of states is not constant over the whole pilin length [65], so the available energy levels from the "head" part of a nearby pilin may

be available as well as the energy levels from the "tail" part of the target pilin. For this reason, consideration of the density of states of the entire assembled pilus, calculated as a whole, is both very important and computationally demanding, thus must wait for further computational advances.

The particular implementation of DFT used for the quantum mechanical calculations on the *Geobacter* pilin [8, 54, 65] is the SIESTA code [69], which uses GGA-DFT. For this application, the PBE version of GGA-DFT, which is more physically inspired and less empirical than some others [70], is used. Since computation time using SIESTA scales linearly with the number of particles considered, rather than to a power of that quantity, SIESTA is well-suited to simulations containing a large number of particles, such as the *Geobacter* pilin in water [54]. The outcome of these theoretical calculations by Prof. Dr. Feliciano of the density of states of a *Geobacter* pilin is compared to experimental data in Chapter 5.

Chapter 5

Results and Interpretation

Geobacter sulfurreducens pili were investigated at room temperature and at 77 K using scanning tunneling microscopy (STM) and point tunneling spectroscopy ("spectroscopy"). Measurements were performed on multiple samples in order to ensure the reproducibility of results, and the room temperature measurements served as controls for the 77 K experiments. This work expanded upon that of Veazey *et al.*, Reference [23], which investigated the topography and spectroscopy of *Geobacter* pili at room temperature using a control of the non-conductive *Pseudomonas aeruginosa* strain K pili [22]. Results obtained at room temperature and at 77 K are presented here and their salient features discussed, along with a comparison to theoretical calculations and suggestions for further investigations.

In brief, *G. sulfurreducens* pili were found to remain conductive at 77 K via acquisition of stable STM topographs. At 77 K, the pilus density of states displayed a distinct gap, as observed by point tunneling spectroscopy. Nonzero density of states began at energies easily reached by metabolically-relevant potentials, however. At room temperature, the pseudogaps in the density of states were shallower and less abrupt than were the gaps in the 77 K dI/dV spectra. This indicates that additional electronic states are made available at higher temperatures. Additionally, the density of states characteristics varied with position across the pilus breadth.

5.1 Topography of *G. sulfurreducens* Pili

Building on previous investigations of *Geobacter* pilus topography by J. Veazey [22, 23], the topographic characteristics of pili were examined at room temperature. The twin aims of this portion of the experiment were to determine whether the use of buffer in the previous work's sample deposition suspension had any effect on the electronic properties or topographic characteristics of the pili and to determine whether pili were amenable to STM measurements at 77 K. While it was not anticipated that any residual buffer would introduce artifactual effects, it was important to verify this assumption in order to compare experimental results using these different sample preparations, as was done in Reference [25]. Topographic similarity of the pili deposited from suspension in doubly deionized H_2O, as described in Appendix C, to the results obtained by Veazey for pili deposited from suspension in PBS buffer [22] was verified, and further topographic studies were performed. Pilus topography at 77 K was found to be similar to room temperature topography. The topographic investigation was extended to the ends of pili or pilus fragments using room temperature STM, as discussed in Appendix D, and the long-term structural persistence of deposited pilus networks was observed using AFM.

5.1.1 Topographic Characteristics of Pili

In STM topographs, the pili had an apparent height of approximately 1 to 5 nm and an apparent cross-sectional diameter on the order of 10 to 20 nm at positive bias voltages, consistent with the tip-broadening effects discussed in Reference [22]. Recall that, for STM topography, the apparent topographic values for the image are a convolution of height and electrical conductivity. A line section across a typical topograph is shown in Figure 5.1.

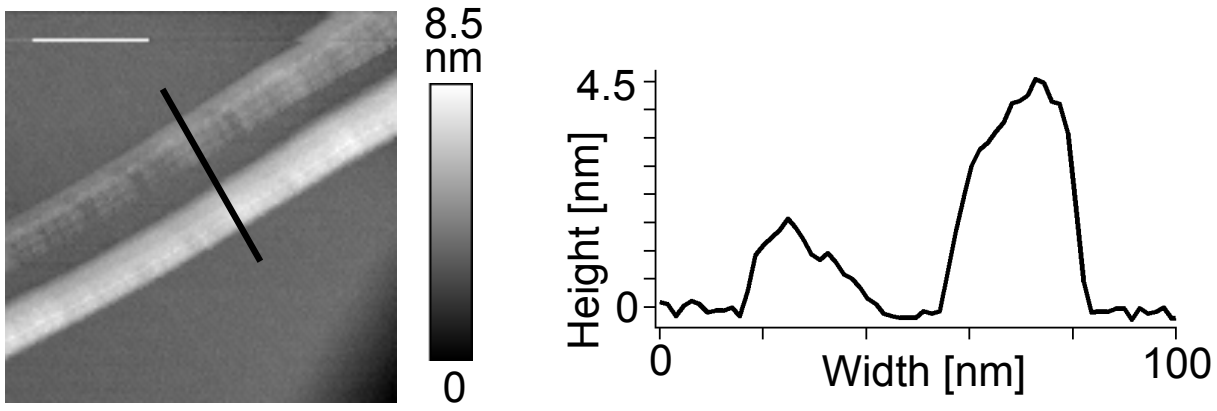

Figure 5.1: Left: Room temperature STM topograph. Scale bar is 50 nm. Right: Line section through the area of the scan marked with the black bar. (+ 0.5 V, 0.08 nA)

The pili do not appear perfectly cylindrical, as can be seen in the topograph and cross-section in Figure 5.1. Leaving aside the convolution between sample and tip shapes which makes the pili appear so much wider than they are tall, the slanted character of the cross-sections displays pilus substructure. At certain values of positive bias voltages (see Reference [22] for voltage-dependent imaging of *Geobacter* pili), including the + 0.5 V which was the typical scanning bias in this work, and when the tip sharpness and sample–substrate adhesion were sufficient to obtain sub-pilus resolution, cross-sections of pili displayed a distinct "ridge–scallop" structure. This consisted of a sharper, cliff-like ridge on one side of the pilus breadth and a less-distinct other side which trailed off to meet the substrate at a smaller angle. The trailing edge appeared scalloped because of a longitudinal periodicity.

Early STM scans of protein-coated DNA, which had dimensions similar to the pili studied here, observed periodic structure [63]. Similarly, a periodic structure was resolved on the pili, as demonstrated in Figure 5.2. This longitudinal pattern was comprised of periodic nodules of increased brightness in the image, generally separated by ~ 6 nm. The increased brightness could be attributed to either increased height or increased local density of states, which are convolved with one another due to the nature of STM topography.

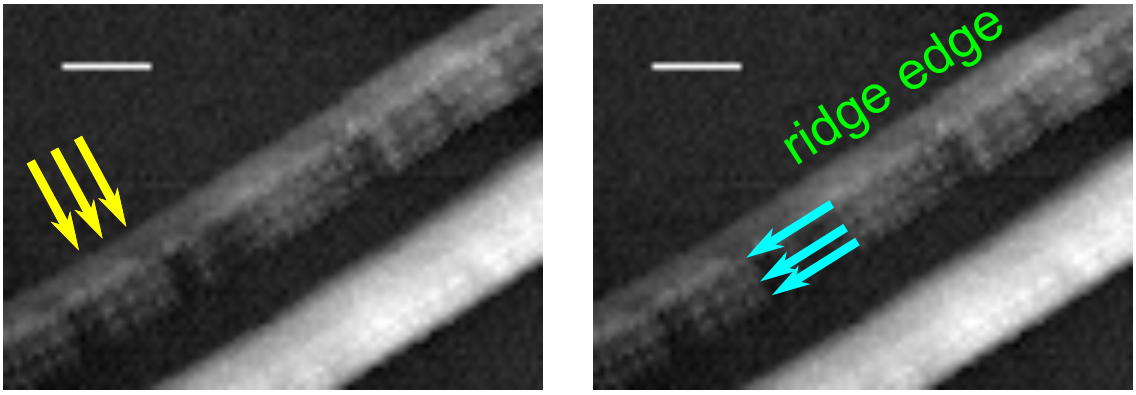

Figure 5.2: Portion of the filament also seen in Figure 5.1. Scale bar is 20 nm. Left: Highlighting the longitudinal pitch. Three of the nodule sets which comprise this pitch are marked with arrows. Spacing between arrows is $\sim$ 6 nm. Right: Highlighting the transverse ridge–scallop structure. The three nodules which comprise this periodic structure are marked with arrows. Spacing between arrows is $\sim$ 5–8 nm. (+ 0.5 V, 0.08 nA)

In addition to the longitudinal periodicities, a transverse periodicity is also observable across the breadth of the pilus. Either two or three distinct repetitions of the nodules can be observed in many STM topographs of filaments. The brightest line of these nodules forms the ridge structure, and the two less-distinct, possibly sometimes smeared into the appearance of one, nodules form the scallop structure. In Figure 5.2, the spacing between the ridge and the center nodule is approximately 6–8 nm, and the spacing between the middle nodule and the scallop-side nodule is approximately 5 nm. Because the periodicity was more apparent in the image at the top of the scan in Figure 5.2, that image was used for this determination. The scalloping of one edge is due to the longitudinal periodicity of the transverse pattern.

These periodic structures were also observed in the work by Veazey [22], showing that any residual buffer salts in the previous research did not attach to the pili in sufficient quantity to obscure topographic variations in the pilus. Therefore, choice of water or PBS as the material in which to suspend the pili is equivalent with respect to the small-scale topography of the

pili, so the earlier results using samples deposited from PBS are extendable to the case of pili on bacteria in a subsurface environment rich with groundwater, applications in which pili not associated with bacteria are in an aqueous environment, or other work done with samples deposited from water [25].

Because STM is a convolution of geometric and local density of states information, the nodule-like bright spots in the STM topographs could be due to structural periodicity in the helical pitch of the pilins assembled to make the pilus, or they could be due to enhancement of the local density of states caused by tyrosine amino acids in close proximity to one another [52], as discussed further below. The longitudinal spacing between nodules is the same order of magnitude as either of these effects [52], but it is not close enough to either to make attribution definite, and measurements with higher spatial resolution are needed to investigate this further.

5.1.2 Pilus Topography at 77 K

Well below the temperatures in the neighborhood of 300 K which are relevant to the bacteria's lives, the relative importance of different mechanisms of pilus conductivity can alter significantly. Temperature-dependent charge transport mechanisms such as those relying on motion of parts of the protein will be abated when the pilus is at 77 K and its surrounding water is frozen. If the pili were to become electrically insulating at 77 K, it would be difficult to establish a stable tunneling current, and the pili would not be easily imaged by STM at this temperature. Before spectroscopy was attempted on the pili at 77 K, then, it was important to establish that the pili were amenable to STM measurements at this temperature. As seen in Figure 5.3, pili could be imaged by STM at 77 K. The bias voltage commonly used to get reliably stable STM images with a tunneling current setpoint of approximately 80 pA at

room temperature, + 0.5 V, was also sufficient for stable imaging at 77 K, as in the example in Figure 5.3. This is likely far greater than the minimum voltage required for the pilus to conduct well enough to be imaged by STM; it was chosen as a compromise between a bias voltage so low that the pili might not be sufficiently conductive and a bias voltage so high that it might perturb the loosely-bound pili on the surface. The value of the pilus resistance could have been determined by pressing the tip into the top of the pilus and thereby using the STM tip as a contact in a two-terminal transport measurement, but the resulting damage to the tip would make subsequent imaging and spectroscopic measurements infeasible.

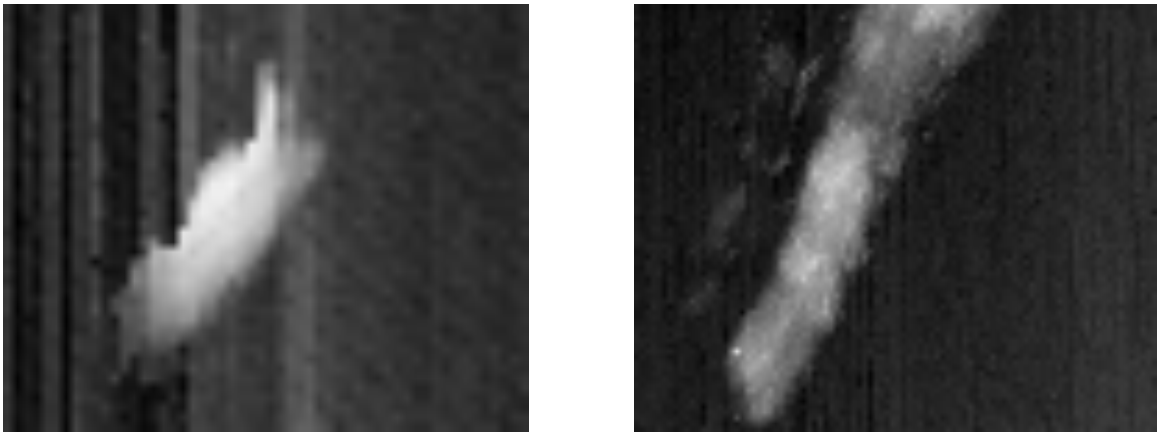

Figure 5.3: Left: Portion of a pilus scanned at 77 K. Right: Portion of a different pilus scanned at 300 K. A multiple tip is responsible for the apparent faint "shadow" to the upper left of the actual pilus. Both scan sizes are 50 nm × 50 nm. (+ 0.5 V, 0.08 nA)

Another example of topography at 77 K is given in Figure 5.4. The speckles in the image are indicative of locally unstable imaging, but since a nearby graphite step edge also showed speckles, this is likely due to an instability on the tip rather than on the sample. The smearing-type alteration between scans in Figure 5.4 can be attributed to loose coupling of biological material to the graphite substrate; the feature in the lower left of the scans appears to have been displaced by the tip.

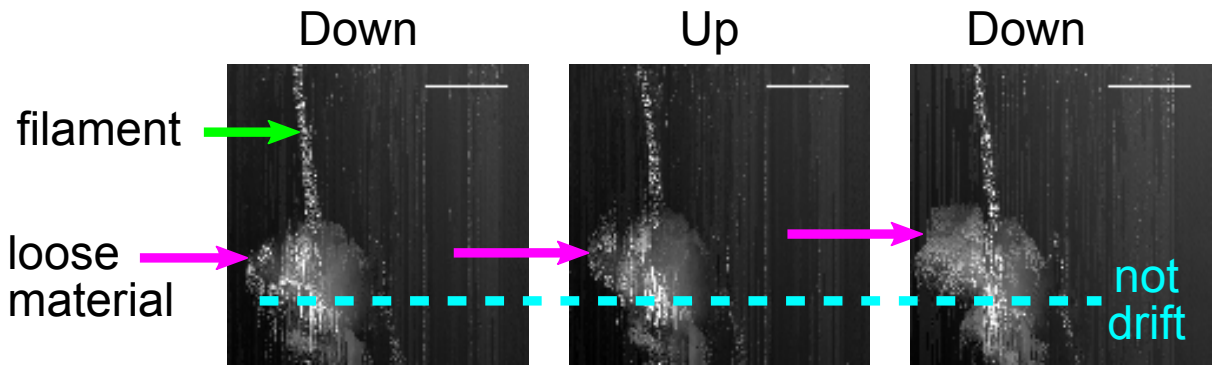

Figure 5.4: Tip-induced displacement of material. Left: Scan of the area with tip moving in the downward direction. Center: Acquired near-simultaneously with the left image but with tip moving upward. Right: Scan of area again with tip moving downward. The motion of the loosely-adsorbed material during scans is not due to drift, as can be seen by observing that the brightest portion of the scan stays in place. Scans performed at 77 K. Scale bars 50 nm. (+ 0.5 V, 0.5 nA)

Both at 77 K and at room temperature, acquisition of stable pilus topography was complicated by the lack of rigorous coupling between the pili and the graphite substrate in many cases, as evidenced by the apparent appearing and disappearing of pili mid-scan and between scans seen in Figures 5.5 and 5.6. When a feature which was previously imaged disappears partway through the scan, it can either have physically moved during scanning, or it can have lost its electrical connection to the bias voltage source.

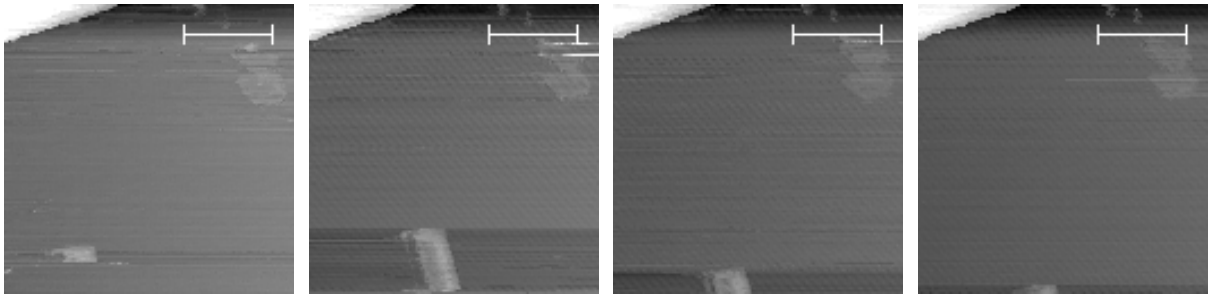

Figure 5.5: Four scans of a filamental fragment at 77 K, done immediately successively in the same position. Verification that the disappearance of segments of the object was not due to drift can be observed via the conserved position of the patch in the upper right of the image. Scale bars 200 nm. (+ 0.5 V, 0.1 nA)

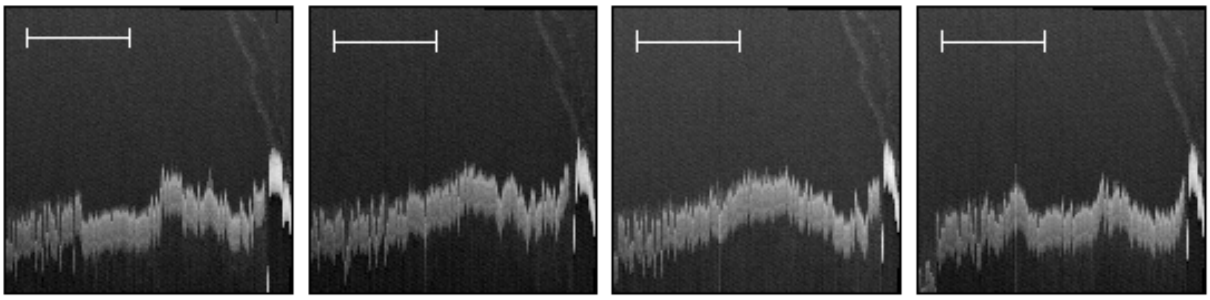

Figure 5.6: Four scans of a filamental fragment at 300 K, done immediately successively in the same position. Portions of the pilus move back and forth between scans. All scans shown were in the downward direction. Scale bars 50 nm. (+ 0.5 V, 0.08 A)

A layer of water likely existed between the pili and the graphite. The ambient air to which the graphite was exposed between cleaving to expose a fresh surface and depositing the sample is known to create an adsorbed water layer on graphite [50]. More tellingly, the sample was deposited from a suspension of pili in doubly deionized water. Since the pili were suspended in water, it is entirely plausible that a thin layer of water could have been trapped between the adsorbed pili and the graphite surface, which then froze when the temperature was lowered. The water layer surrounding a protein can contribute significantly to the charge transport characteristics of said protein [71]. Indeed, the water layer adsorbed onto the sample surface in a moderately humid environment has enabled STM studies, using specialized equipment, of biological materials on insulating substrates, where the bias was delivered to the sample through the water layer [72]. Making measurements when the sample had been reduced from atmospheric conditions to a vacuum of a few or a few tens of μtorr is not sufficient to remove all the water, including the last adsorbed water monolayer, from the sample [50]. Consequently, the pili may be considered to be in a hydrated state for the measurements at room temperature. At 77 K, all water which may remain on the sample will exist in a frozen state. Since pili were not necessarily well-coupled to the graphite

substrate at room temperature as well, as shown in Figure 5.6, ice formation alone is not responsible for sample–substrate connectivity issues. Water is not the only substance which can cause lessened electrical contact between the sample and the graphite substrate; some studies suggest hydrocarbons present in the air can cause changes to the work function of the graphite surface over time, even in vacuum [73]. Several studies have shown "patchy" areas in work function mapping [73] and mechanical properties [74] of graphite surfaces investigated either in high vacuum or in ambient conditions, suggesting that areas of the graphite surface may have different surface properties which could affect where the pili tend to adsorb well.

Since the pili investigated here were deposited from a suspension in doubly deionized water and the pili previously investigated at room temperature were deposted from a suspension in phosphate buffered saline [22] (PBS, or sometimes colloquially, if redundantly, "PBS buffer"), additional measurements were performed at room temperature to provide a control better reflecting the conditions under which the cryogenic results were obtained, rather than simply using the previous results as the control. Conventional imaging of biomolecules, *e.g.,* DNA by AFM, often takes place in a buffer solution to neutralize the charged biomolecules so that they will more easily lie on a charge-neutral surface [75].

Many of the STM topographs and endpoints of spectroscopy voltage sweeps in the previous work on *Geobacter* pili deposited from PBS [22] were obtained at 1 V bias. It was empirically determined during this work that such a voltage tended to induce more instability in the imaging and spectroscopy. In order to obtain more stable, hence more reproducible, results which applied less electrostatic force to the sample, most topographs and spectroscopy voltage sweeps here were obtained at a bias magnitude of 0.5 V. The general decrease in imaging stability at 1 V compared to the previous work [22] could speculatively be attributed to pilus–substrate contact differences due to the suspension fluids used in the experiments.

5.1.3 Structural Longevity of Pilus Fibers

If pili are to be used in device applications separate from their originating bacteria, they must maintain their characteristics over time. Proteins are conventionally preserved by chemically fixing them with substances such as glutaraldehyde, which causes topographic changes in the pili as observed by STM [22] and may also change the conductive properties of the pili. In the interests of determining the longevity of the unfixed pilus nanowires studied here, a sample was prepared of pili deposited on SiO_2 with gold electrodes also present, as part of the longitudinal conductivity study discussed in Reference [25]. The sample was then stored, spending much of that time under a gentle overpressure of nitrogen gas. This sample was scanned using the same AFM immediately after deposition and again 22.5 months later; example scans from this comparison are shown in Figure 5.7.

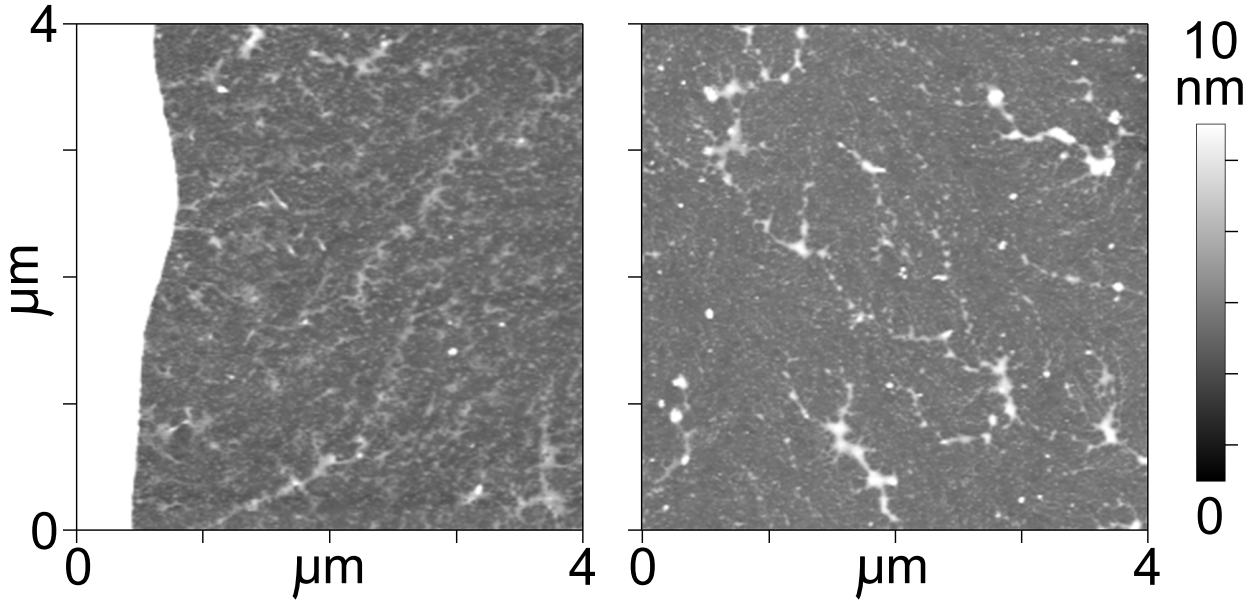

Figure 5.7: Left: AFM topograph of a freshly-deposited sample of pili on SiO_2. Right: Same sample rescanned after 22.5 months, showing no degradation of the sample.

The pilus fibers remained structurally intact over this duration, as can be seen in Figure 5.7, where the distribution of pili follows a conventional pattern in both images. Addi-

tionally, the slightly bulbous appearance of the bundled pili, whether due to windings of pili around one another or to trapped fluid between pili, was retained over this length of time, as seen in the smaller scan-range topograph in Figure 5.8. Conductivity properties of the pili were not investigated over time, nor was the lifetime of pili on conductive substrates such as graphite probed over such a duration. Both would be useful further studies. The observation that the pili remained structurally intact, at least to 1 nm resolution, on an insulating substrate over a minimum span of nearly two years is a promising sign for applications of pili in devices with realistic lifespans.

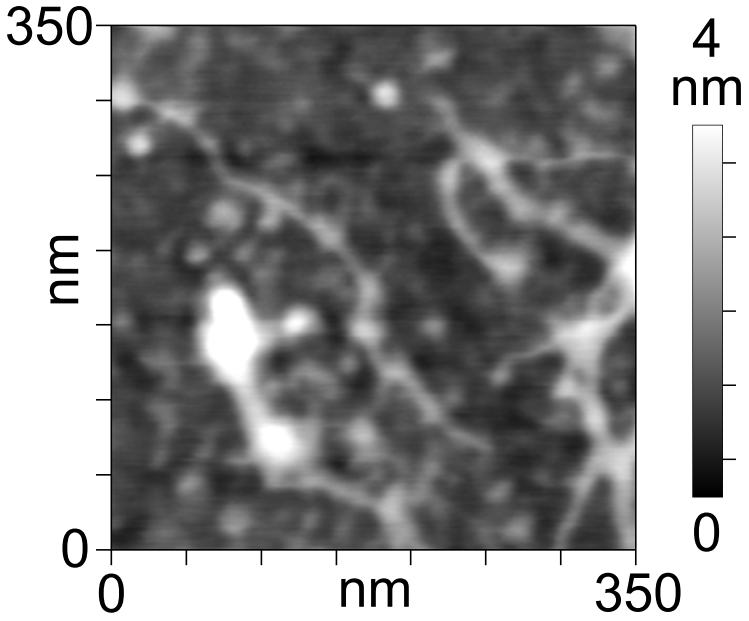

Figure 5.8: 350 nm × 350 nm AFM topograph of the 22.5 month old sample showing intact individual pili and pilus bundles.

5.2 Room Temperature Spectroscopy

Point tunneling spectroscopy was performed at room temperature to act as a control for two different experiments. First, and primarily, it was to act as a control for the cryogenic

spectroscopy that was the prime focus of this work. Second, it was to verify that no changes were introduced to the electronic properties of the pili due to the purification procedure and deposition in doubly deionized water rather than PBS buffer. While room temperature spectroscopy had been obtained by Veazey [22, 23, 65], the sample purification procedure and sample deposition method had evolved since those experiments. The room temperature results of Veazey [22, 23, 65] were verified using both the cryogenic-capable STM and the Cypher scanning probe microscope in STM mode, so there are no microscope-dependent effects on the results. Because the tip was prone to acquiring contaminants between spectroscopy measurements, a control measurement was generally performed on graphite before and after on-pilus measurements.

An example of room temperature dI/dV on a pilus is shown in Figure 5.9. Spectroscopy was performed on the lower edge of the brightest filament shown in Figure 5.1 with graphite control spectroscopy before and after. The process of obtaining the numerically-differentiated dI/dV curves is discussed in Appendix D.

In the main, dI/dV curves obtained on the surfaces of pili at room temperature showed pseudogaps in the vicinity of zero applied bias. Unlike a standard bandgap in the delocalized charge carriers paradigm or HOMO–LUMO gap in the molecular orbitals paradigm, the bottoms of these pseudogaps in the density of states did not entirely reach zero dI/dV. For this reason, the pili could be described as pseudo-semiconductors at room temperature. The other criterion for semiconducting behavior, that of being susceptible to doping, can be achieved by creating mutant strains with different amino acids [25] or by changing the pH of the surroundings [32]. The finite dI/dV at room temperature for all voltage values probed highlights the conductivity of the pili at even very small applied voltages.

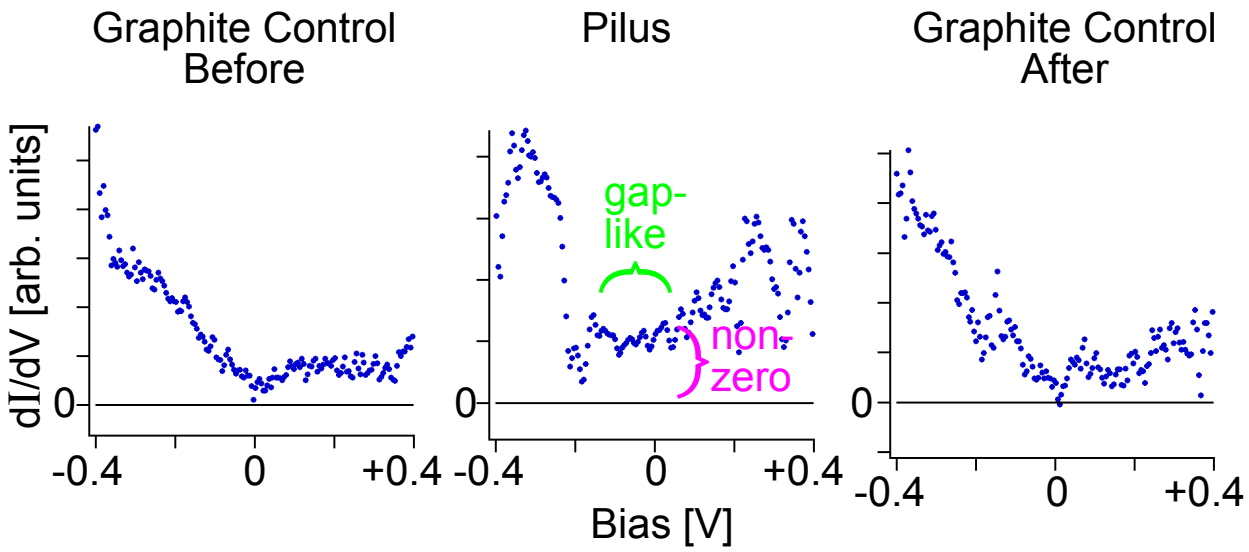

Figure 5.9: dI/dV on a pilus at room temperature. Left: Graphite control. Center: Edge of pilus. Right: Graphite control. Because of higher levels of scatter in the data, the pilus dI/dV was smoothed again after differentiation using a 3-point binomial smoothing, in addition to the procedure described in Appendix D.

5.2.1 Positional Dependence of Room Temperature Spectroscopy

As was previously observed by Veazey [22], the density of states characteristics of pili at room temperature depended on where across the breadth of the pilus the spectroscopy point was positioned. Briefly, the center of the pilus had a density of states which was more graphite-like, while spectroscopy performed on either the ridge or the scallop edges of the pilus showed more structure.

The varied characters of spectroscopic measurements taken over different parts of the pilus could possibly be attributed to summation of the densities of states of multiple pilins in the assembled pilus. Since pili are composed of a spiral pattern of pilins, neighboring pilins will have different parts of their structure beneath the tip. As the calculated density of states has a spatial dependence along the pilin [65], pilins can supplement their neighbors' densities of states to varying extents depending on where above the pilus the tip is positioned.

The zero-bias point on the dI/dV spectrum was not necessarily in the center of the

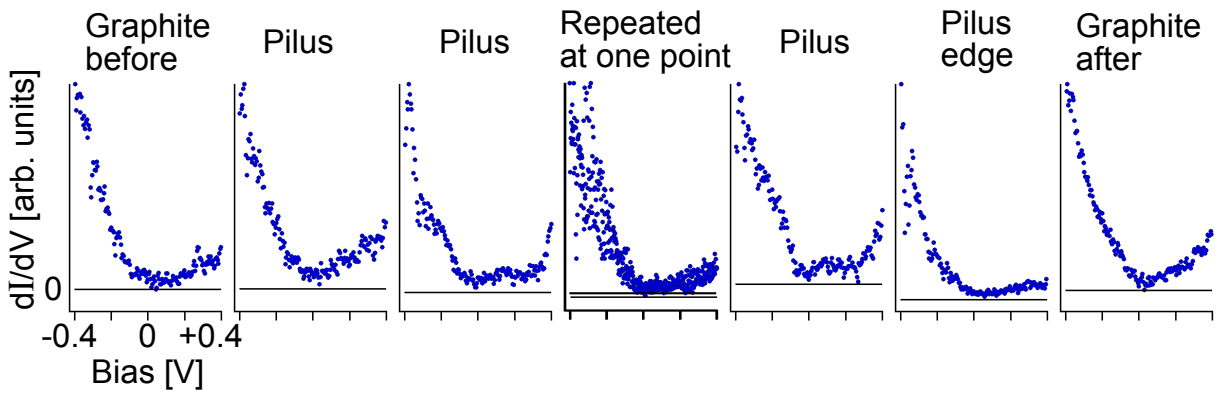

Figure 5.10: dI/dV on a pilus at room temperature. Left: Graphite control. Center: dI/dV obtained in several locations transversally across the breadth of the pilus. Right: Graphite control. All abscissas are from - 0.4 V to + 0.4 V. Horizontal lines are $dI/dV = 0$.

pseudogap, as also observed in the cryogenic spectroscopy discussed below. This could be interpreted as a diode-like asymmetry in the onset of conductivity; in the interests of circumspection, this assertion is not made conclusively. An experimental source of similar results could be "Fermi level pinning" due to non-pilus materials present on the sample. For example, a lesser quality of electrical contact between the sample and the substrate could act as though it were a dopant decreasing the net overall conductivity, or the substrate itself could dope the nanowires [28]. This does not speak against the results presented here, since results were reproduced on more than one pilus, and it is unlikely that identical contaminants would be uniformly present.

5.2.2 Reproducibility of Room Temperature Spectroscopy

Similar spectroscopy was obtained on several pili at room temperature. Because of the gradualness of many of the pseudogap edges, pseudogap widths were difficult to assign definitively. Further, the position-dependence of the spectroscopy across the breadth of the pilus introduced scatter in the comparison between samples. Despite these caveats, the pseudogaps at room temperature were found to have an average width of 0.4 V, with a standard deviation of

0.1 V. This value was obtained by averaging pseudogap widths from seven objects on which spectroscopy could be obtained. The difference between pseudogap widths on different sides of the pili was not statistically significant, in large part due to the variation in pseudogap width determinations. With these room temperature spectroscopy results in mind, results of spectroscopy at 77 K can be put in a firmer context.

5.3 Spectroscopy at 77 K

The primary novel thrust of this research was investigation of the density of states of *G. sulfurreducens* pili as seen in dI/dV measurements from tunneling spectroscopy at 77 K. Similar results were obtained on multiple samples, as in Figure 5.11, indicating that the results were reproducible and not artifactual. The gross features of the spectroscopy were the same across samples, although the matter is complicated based on the variability of dI/dV curves depending on the exact position along the pilus at which they were obtained, as observed at room temperature and even more pronouncedly at cryogenic temperature.

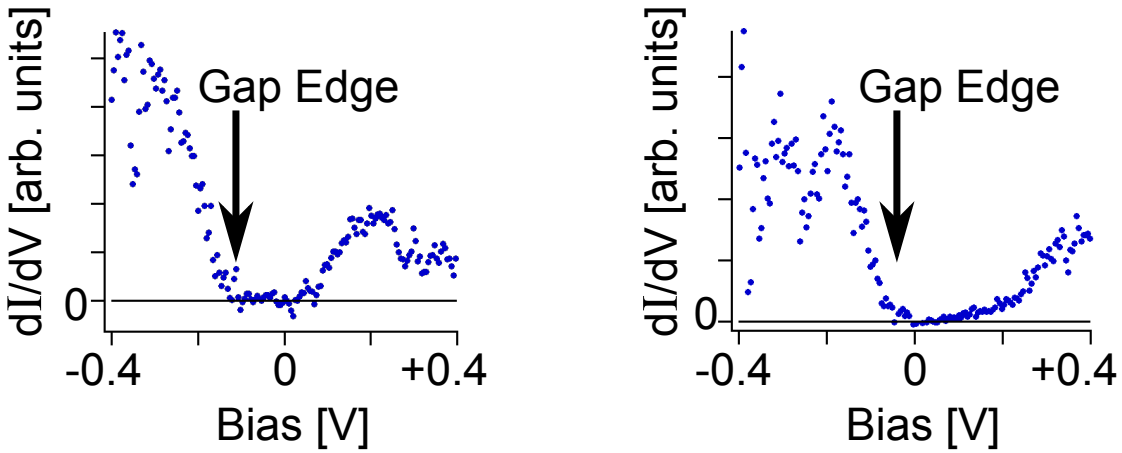

Figure 5.11: Spectroscopy performed on two separate pili, using two different tips and two separate sample depositions. The left edge of the gap is similar, and both spectra encounter $dI/dV = 0$ inside the gap.

For dI/dV curves such as those in Figure 5.11, determination of gap widths was done from numerically-differentiated I–V curves which had been smoothed by a 47-point Savitzky–Golay smoothing. Since five voltage sweeps, yielding five I–V curves, were generally obtained sequentially at a given point on the sample, the gap widths were determined independently for each of the five curves. The onset of the gap was identified as the voltage at which the dI/dV curve began to ascend steeply from its baseline value. The chief source of uncertainty in gap width determinations at a given point on the sample was slight, non-systematic differences between sequential curves acquired at the same point. For this reason, gap widths are quoted only to one significant figure.

5.3.1 Salient Features of Cryogenic Spectroscopy

Certain features were reproducibly observed in 77 K spectroscopy of the pilus nanowires. For simplicity, these features will be discussed with reference to one data point in particular, and the dependence of spectroscopic features on position across the pilus will be discussed as a subsequent topic.

Figure 5.12 presents dI/dV spectroscopy on a pilus at 77 K, bookended by control spectroscopy on the nearby graphite surface before and after the spectroscopy performed on the pilus. The absolute values along the ordinate axis are not relevant; it is the *relative* heights of peaks and valleys on the curve that matter. It is accepted practice in this type of measurement to give the ordinate axis in arbitrary units.

As discussed in Chapter 2, zero is the only meaningful value along the ordinate axis, as it means there are no electronic states available over that entire voltage range for which dI/dV is zero. This, in turn, means that adding electrons by increasing the magnitude of the voltage does not correspondingly alter the current response, which is a sign of a

semiconductor or insulator. The gap width of 0.2 eV, as shown in Figure 5.13, is an order of magnitude smaller than that for proteins which aren't used for charge transport, such as *Pseudomonas* pili [22]. This means the *Geobacter* pilus has electronic states available for very little energy investment.

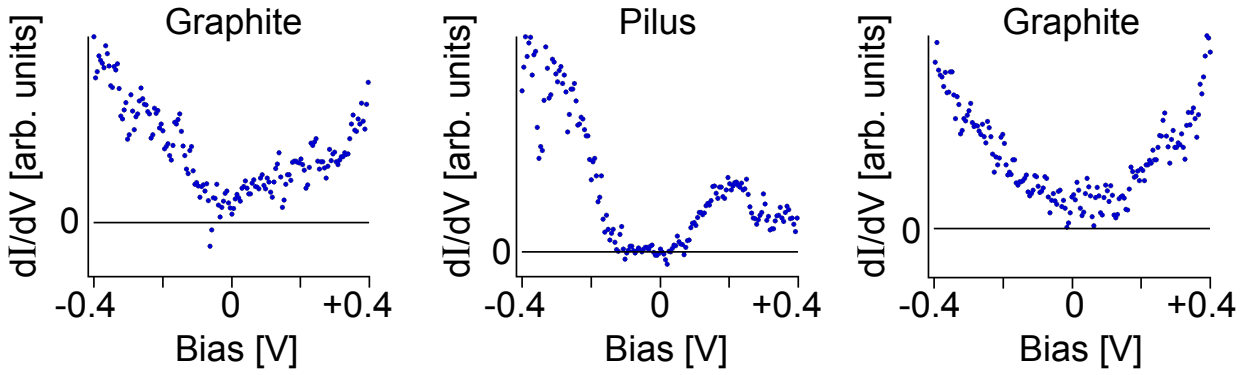

Figure 5.12: Immediately-sequential point tunneling spectroscopy performed on a pilus and nearby graphite. Left: Graphite spectroscopy before pilus spectroscopy. Center: Pilus spectroscopy. Right: Graphite spectroscopy after pilus spectroscopy. Horizontal line is at $dI/dV = 0$.

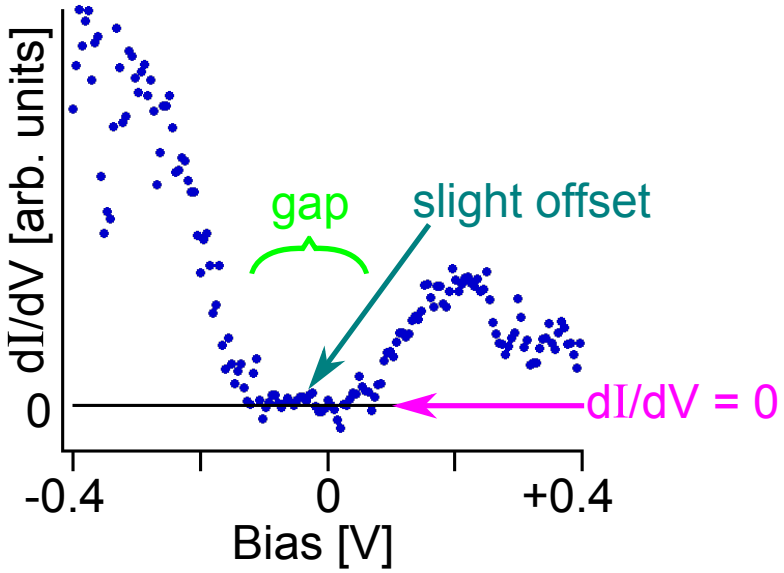

Figure 5.13: Detail of pilus spectroscopy from Figure 5.12. Gap width is 0.2 eV. Bottom of gap is at $dI/dV = 0$. Center of gap is slightly more negative than 0 V.

5.3.2 Positional Dependence of Cryogenic Spectroscopy

As in the room temperature spectroscopy results, the shape of the dI/dV curves on pili at 77 K depended on where along the breadth of the pilus the spectroscopy point was positioned. The spectroscopy in Figure 5.14 was obtained on the same pilus as that in Figure 5.12, but its gap is significantly wider, 0.4 eV. The repeated before-and-after graphite control spectroscopy shows that this is not due to tip contamination. The bottom of the gap is still at $dI/dV = 0$.

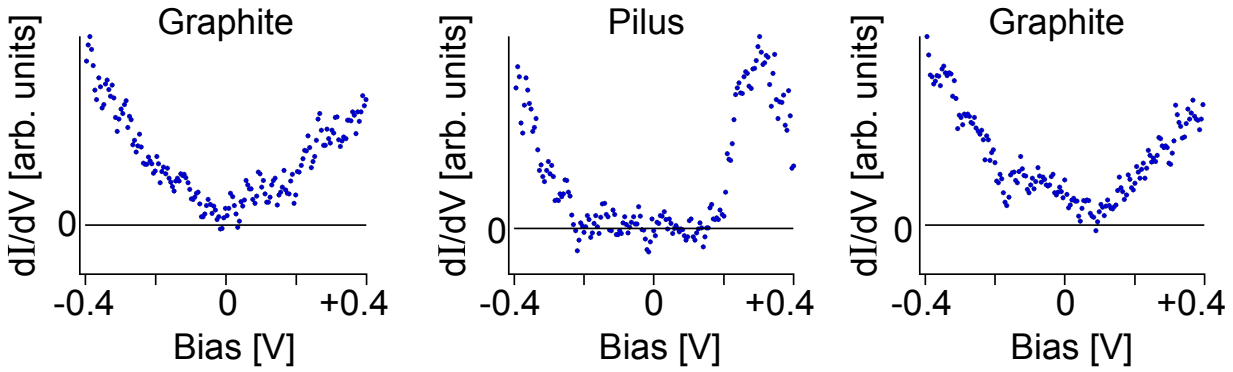

Figure 5.14: Immediately-sequential point tunneling spectroscopy performed on a different part of the pilus from Figure 5.12. Left: Graphite spectroscopy before pilus spectroscopy. Center: Pilus spectroscopy. Right: Graphite spectroscopy after pilus spectroscopy.

For the particular pilus in Figures 5.12–5.14, additional dI/dV curves were obtained in different locations on the pilus and are shown in Figure 5.15. All pilus spectroscopy in Figure 5.15 was preceded and followed by graphite control spectroscopy. Since this not only reproduces the room temperature finding, originally observed in Reference [22], that position-dependent spectroscopy is a characteristic of *Geobacter* pili but enhances the differences considerably, it suggests that the position-dependent dI/dV arises because of the density of states of the pili.

The peculiar shape of the dI/dV curve in the center of Figure 5.15 cries out for control measurements. While the dI/dV above the middle of the pilus is unusually shaped, the

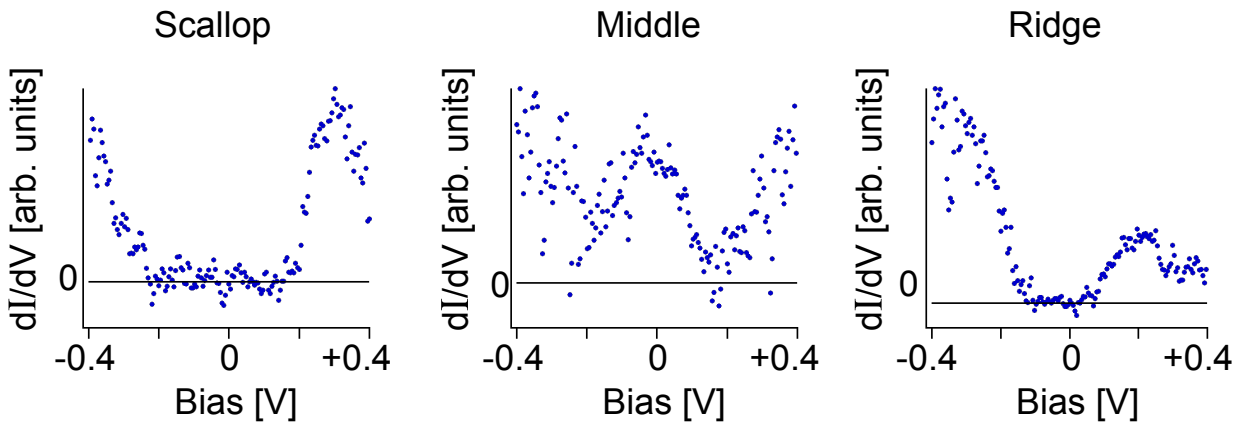

Figure 5.15: On-pilus spectroscopy, labeled by the estimated location across the diameter of the pilus at which the spectroscopy was taken. Left: dI/dV on the more diffuse side. Center: dI/dV towards the middle. Right: dI/dV near the more separate area of the pilus. Bottoms of gaps are at $dI/dV = 0$.

control measurements of graphite immediately before and after that data are acceptably interpretable as graphite, as can be seen in Figure 5.16. Perhaps the shape is due to interplay between density of states contributions of neighboring pilins. This was only clearly observed on this particular pilus, so it remains to be convincingly reproduced and is presented here as a matter of interest rather than the subject of substantive claims or interpretations.

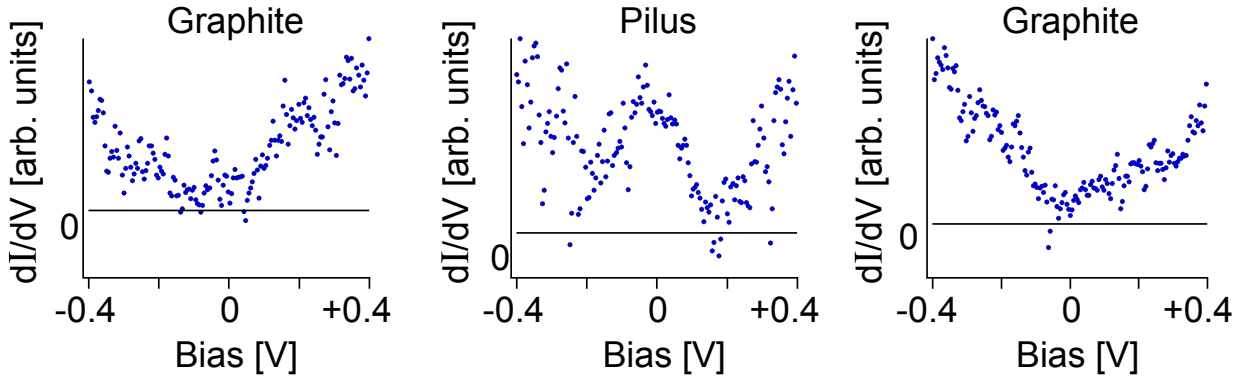

Figure 5.16: Immediately-sequential point tunneling spectroscopy performed on the middle part of the pilus from Figure 5.12. Left: Graphite spectroscopy before pilus spectroscopy. Center: Pilus spectroscopy. Right: Graphite spectroscopy after pilus spectroscopy.

5.3.3 Reproducibility of Cryogenic Spectroscopy

As in the room temperature spectroscopy, the position-dependence of the spectroscopy at 77 K led to a variation in gap width for spectra obtained at different positions across the breadth of the pilus, although gaps in the spectroscopy at 77 K were easier to determine due to more abrupt gap edges. The gaps at 77 K were found to have an average width of 0.3 V, with a standard deviation of 0.2 V. This value was obtained by averaging gap widths from six objects on which spectroscopy could be obtained at 77 K. The larger standard deviation in the 77 K spectroscopy compared to that at room temperature is in part due to the small widths of gap-like features such as those in the spectroscopy on the middle of the pilus in Figure 5.16. Gaps and pseudogaps at 77 K and at room temperature were consistent in width with one another.

5.3.4 Comparison to Room Temperature Spectroscopy

Overall, the dI/dV spectroscopy obtained on *Geobacter* pilus nanowires at 77 K was comparable to that obtained on pili at 300 K, with two important differences, shown in Figure 5.17. The cryogenic spectroscopy had more abrupt gap edges. This includes accounting for the difference in spectroscopy at different locations transversally across the breadth of the pilus, and even accounting for thermal broadening effects at room temperature, which almost—but not quite—soften the gap edges enough to make up the difference and are discussed further below. Secondly, the gaps in the dI/dV at 77 K genuinely reached zero density of states, with gap widths on the order of 0.2–0.4 eV, which is narrow-gap semiconductor-like behavior. Pseudogaps in the room temperature spectroscopy did not quite reach down to zero differential conductance. Room temperature spectroscopy was in general slightly less

stable, perhaps because at 77 K, most contaminants were frozen into greater stability. Despite these differences, however, the cryogenic and room temperature dI/dV spectra were recognizably similar in character to each other, displaying either semiconductor (77 K) or reminiscent-of-semiconductor (300 K) dI/dV.

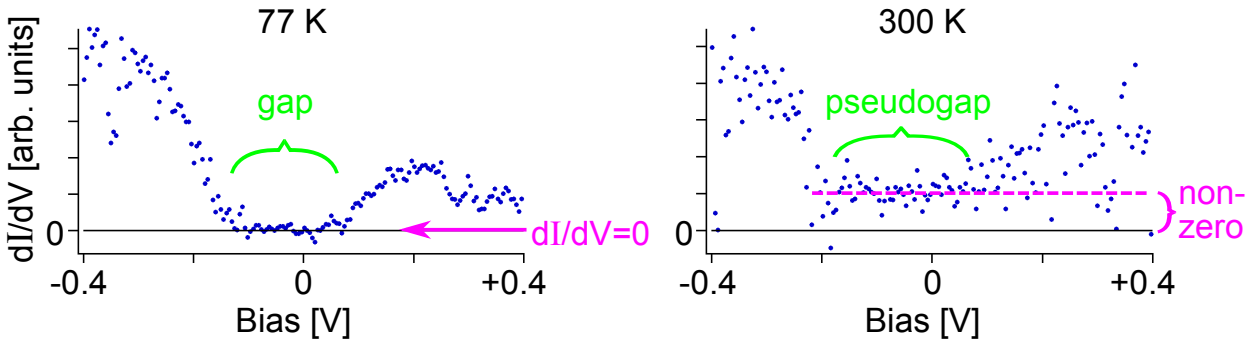

Figure 5.17: Comparison between cryogenic and room temperature dI/dV. Left: 77 K spectroscopy. Right: 300 K spectroscopy. Dashed line is a guide to the eye indicating pseudogap bottom.

5.3.5 Effect of Thermal Broadening

Thermal broadening of the density of states contributes to the measured dI/dV. At temperatures above 0 K, temperature-induced fluctuations in the occupation of the available states will smear out the ability of a dI/dV measurement to discern the pure density of states. For this reason, when comparing 77 K and 300 K results, it is useful to set forth the expected contribution of purely thermal broadening, statistical effects so this can be qualitatively disentangled from effects on the spectroscopic results due to different temperature-dependent processes. An example of a case in which such thermal broadening effects can mimic or obscure the effect of more exotic physical processes on a system's temperature dependence is discussed in Reference [76].

Previous room-temperature spectroscopy on *G. sulfurreducens* pili [22] showed pseudo-

gaps in the density of states where the conductivity was consistently minimal, slightly above zero, for small magnitudes of the applied voltage. From this, it could be predicted that such gap-like features would widen and deepen as the temperature was decreased. As an example of this, assume an idealized semiconductor which has perfectly straight bandgap edges when the density of states is measured, as shown in Figure 5.18. Raising the temperature to 300 K and considering only thermal effects would amount to convolving the function which describes the shape of the density of states with the derivative of the Fermi function, because the charge carriers in this system obey Fermi-Dirac statistics, at each voltage value. This is done in Equation 5.1, where the specific voltage value for which the thermal broadening is evaluated is represented by V_0 in units of mV. Additionally, all energy units, conventionally in electron volts, have been converted to mV to match experimental quantities, and values of V are expressed in units of mV to correspond to the voltage range relevant to this experiment, recalling that at room temperature, $k_B T = 25$ meV.

$$\begin{aligned} dI/dV\,_{300\mathrm{K}}(V_0) &= \int_{-\infty}^{+\infty} DOS(V) * f'(V - V_0)\; dV \\ &= \int_{-\infty}^{+\infty} DOS(V) * \frac{1}{25}\; \frac{\exp[(V - V_0)/25]}{\{\exp[(V - V_0)/25] + 1\}^2}\; dV \end{aligned} \tag{5.1}$$

As can be seen in Figure 5.18, the statistical effect due to an increase in temperature to room temperature is insufficient to erase the bandgap of this hypothetical material; it only softens the edges somewhat. Thus cooling the samples, especially only down to 77 K, will not open up tenths-of-eV-scale gaps in the density of states of the pili by decreasing thermal broadening. Since the effect of thermal broadening is noticeable in the idealized semiconductor in Figure 5.18, it is valuable to repeat this calculation to see the effect of thermal broadening on actual dI/dV data. The results of this are shown in Figure 5.19. For

these calculations, the dI/dV at 77 K is assumed to be equal to the density of states; since there is some minor thermal broadening already present in the 77 K data, the actual thermal broadening will not be quite as pronounced as that seen in Figure 5.19, which nevertheless does not remove the gap structure sufficiently to match the measured dI/dV at 300 K.

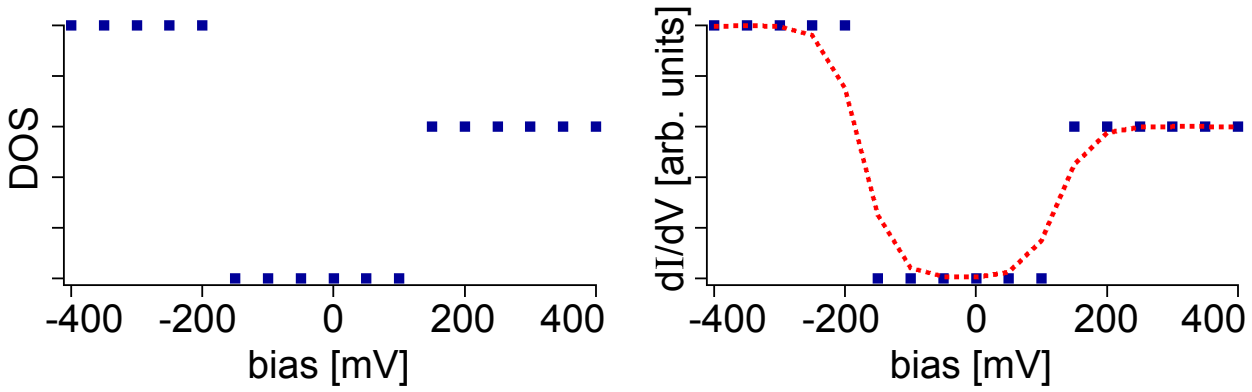

Figure 5.18: Effect of thermal broadening, given by Equation 5.1, on a hypothetical semiconductor with sharp bandgap edges. Left: Density of states. Right: Thermally-broadened DOS which would be measured as dI/dV of this semiconductor at 300 K, overlaid on the DOS. dI/dV is plotted as a dashed line as a guide to the eye; actual point spacing for both plots' computations is 50 mV.

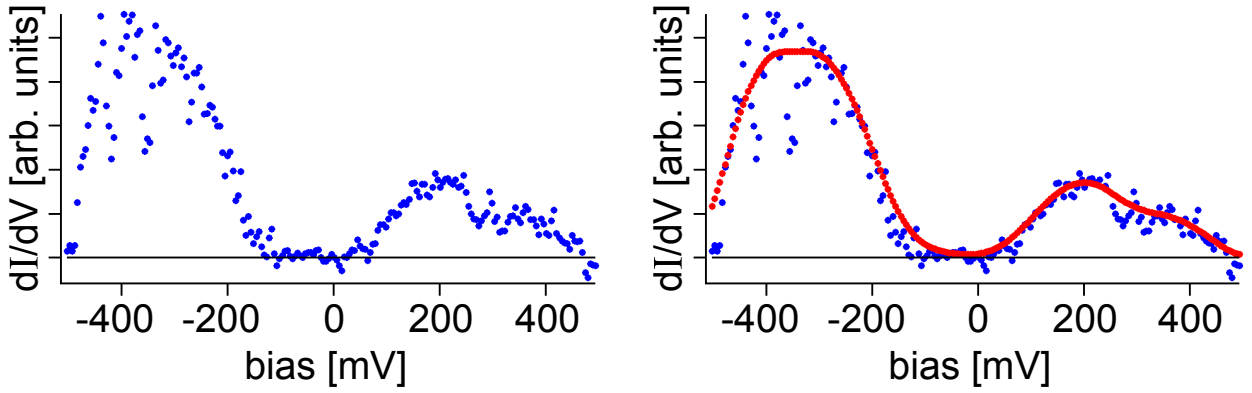

Figure 5.19: Effect of thermal broadening, given by Equation 5.1, on actual pilus data obtained at 77 K. Left: dI/dV at 77 K. For the purposes of this calculation, this is assumed to be equal to the density of states, thus the effect of thermal broadening will be slightly smaller than shown here. Horizontal line is $dI/dV = 0$. Right: Data thermally broadened by 300 K, overlain in red. Feature edges and small oscillations in the dI/dV appear smoothed.

5.4 Results in Context

Using the room temperature spectroscopy measurements as a control, STM and point tunneling spectroscopy on *G. sulfurreducens* pilus nanowires at 77 K showed that the pili are transversally conductive and have a semiconductor-like density of states when probed at cryogenic temperatures. The edges of this gap, energies at which electronic states become available, are at some few tens or hundreds of mV, which is on the order of biologically-relevant potentials involved in *Geobacter* metabolism [77]. It can be instructive to put these findings in a larger context, particularly by comparison to theoretical insights.

5.4.1 Comparison to Theoretical Calculations

Theoretical investigations by means of *ab initio* calculations can provide a physical context for interpretation of the observed dI/dV of the pili. As discussed in Chapter 4, the temperature dependence of the calculated density of states enters the calculations at the level of the molecular dynamics simulation, where the physical shape of the pilin is determined at a given temperature, surrounded by water, since the pili remained hydrated even after the experimental drying process [50]. The density of states itself is temperature-independent; how many and which of these states are actually filled at a given applied voltage—the independent variable in dI/dV measurements—depends in part on temperature-dependent processes in the system.

Calculation Parameters

It has long been known for semiconducting proteins that adsorbed water on the protein greatly affects its conductivity [78]. Proteins deposited from water and wicked dry, even

when placed in a high vacuum microscope, will be surrounded by at least a small amount of water [50]. For this reason, considering some water molecules in conjunction with the protein itself is important; also, pili *in vivo* are surrounded by water, and water affects the conductivity properties of proteins, so it is more realistic to consider pili surrounded by water. Furthermore, the relationship of the water and dissolved ions to the pilin subunit accounts for much of the propensities of its calculated electronic structure.

Beginning from the homology model [8] for the approximate configuration of the atoms in the *Geobacter* pilin molecule, Prof. Dr. Gustavo Feliciano performed classical molecular dynamics simulations at 300 K to determine the configurations the pilin and its surrounding waters would take [8, 65]. These atomic positions at different "snapshots" in time were then input into the *ab initio* quantum mechanical SIESTA [54] code to perform the density of states calculations [8, 65]. The density of states calculations simulated the electronic structure of the pilin in the context of its surroundings, based on atomic charges and atomic positions determined by the molecular dynamics simulations. Because the pilin at 300 K sampled such a large variety of conformations in the course of the molecular dynamics simulation [8] and the pilin at 77 K was found to remain essentially in its initial configuration, it could be assumed that the 300 K calculations could also describe the 77 K density of states.

Calculated Density of States

Simulations of *Geobacter* pilins at room temperature show a gap in the density of states in which the differential conductivity goes completely to zero. This gap is much narrower than the few-eV gap seen in most proteins [8, 65], as expected, since *Geobacter* pilins are part of electrically-conductive pili, by contrast to most proteins, which are electrically insulating. However, this calculated gap is wider by a factor of two to four than that observed in

experimental spectroscopy. This is interesting in light of the expectation that GGA-DFT would be expected to underpredict the gap width [68], although published calculations on a room temperature pilin also overpredict the gap [8]. For a broader perspective, the calculated density of states is shown in Figure 5.20 over twice the voltage range used to display most of the experimental data. This shows the shape of the non-gap density of states; restriction to the experimentally-probed voltage range would show very little beyond the gap. In general, the character of the calculated density of states is closely akin to that of the experimentally-determined dI/dV, although the calculated gap is wider. A slight offset of the center of the gap from 0 V can be observed in some of the calculated curves, as can be compared to the experimental data in Figure 5.13, indicating that Fermi level pinning is not the only mechanism by which experimental curves could be offset in energy. Specific peaks in the theoretical curves are not easily correlated with peaks in experimental curves.

The density of states presented in Figure 5.21 is formed from an average of five normalized density of states calculation results. The five component curves, among those shown over a larger voltage range in Figure 5.20, are density of states calculations using density functional theory, obtained for different conformations of the pilin, ions, and water at statistically independent snapshots of the molecular dynamics calculation; density of states calculations were performed by Dr. Feliciano. Both experiment and theory show a gap which reaches to zero on the ordinate axis; the calculated gap is wider.

Discussion of Theoretical Calculations

Discrepancies between measured and calculated densities of states in this system could be attributed to several possible origins. The calculated density of states for each individual simulated spectrum in Figure 5.20 is based on the physical structure of the pilin and

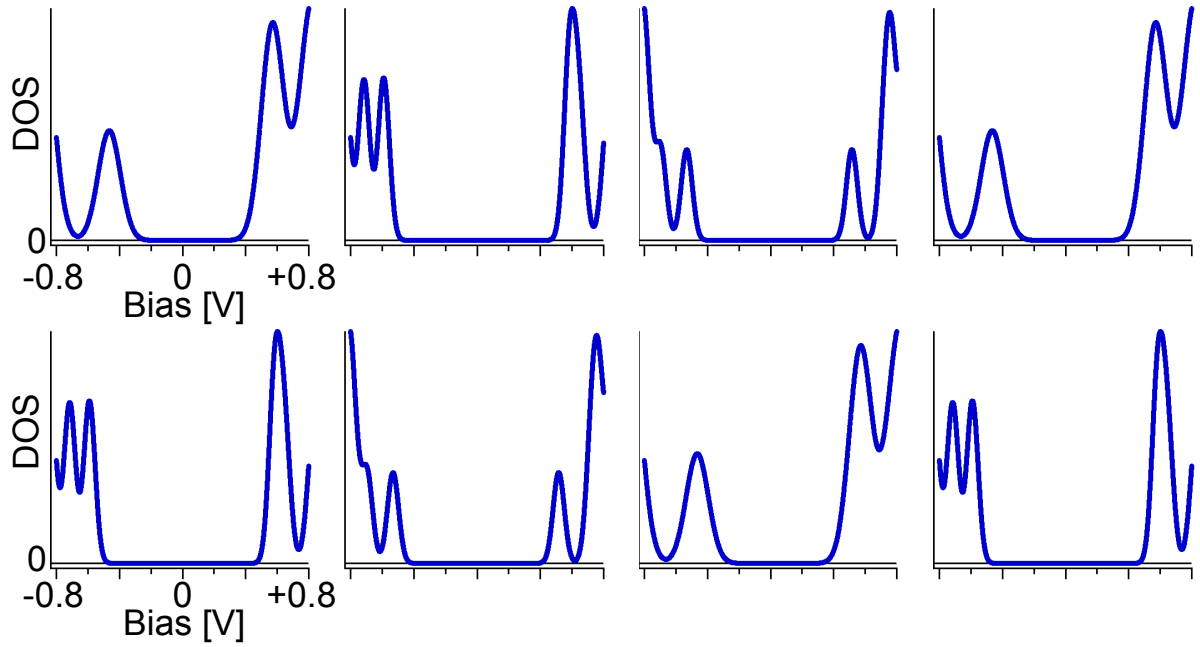

Figure 5.20: Calculated density of states for a *Geobacter* pilin [65]. Eight snapshots of pilin and solvent conformations, shown individually to display the variation in density of states among configurations. All calculations plotted here are displayed over twice the voltage scale of the experimental data to show more of the structure of the density of states. Molecular dynamics and density functional theory calculations were performed by G. Feliciano.

water at one snapshot in the molecular dynamics simulation and does not include the motion of the protein. Proteins reconfigure, at least slightly, in response to their electrostatic environments—this contributes to the reorganization energy λ in Marcus theory, as discussed in Chapter 4. Considerations of small motions of components of the pilus due to the electronic interaction with the STM tip are neglected in the experimental interpretation. Similarly, the theoretical calculations consider the pilin density of states to be determined by its structure and interactions with the water but do not include interactions with the tip, which can be important but difficult to quantify [79].

Perhaps more significantly, the calculations are only computationally tractable at the pilin level at the moment, and the measurements were done on fully-assembled pili. Since the majority of the pilin structure is buried within the assembled pilus, this can not only

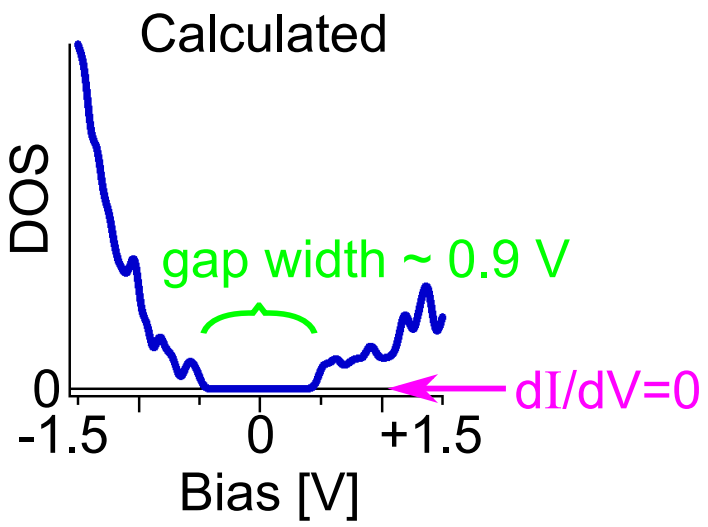

Figure 5.21: Calculated density of states for a *Geobacter* pilin [65]. Five snapshots of pilin and solvent conformations are averaged together. Molecular dynamics and density functional theory calculations were performed by G. Feliciano.

have implications for the conformation of the pilins [52] but also for the electrostatic and hydration environment of the pilins. The model shown in Figure 4.6 is evaluated with periodic boundary conditions, thus essentially describing a chain of pilins surrounded by boxes of water rather than assembled with one another. Since the interior of the pilus is hydrophobic, the α-helices are less exposed to water in the assembled pilus than they are in the calculated scenario as shown in Figure 4.6. As postulated in Chapter 4, "leakage" of available electronic states from pilin to pilin within the assembled pilus could act to decrease the gap width as the electronic structures of adjoining pilins overlap. Further calculations in progress from Dr. Feliciano begin from the very recently-determined NMR pilin structure [52] rather than the homology model [53], and efforts are currently underway to simulate a portion of an assembled pilus.

The difference between calculated and experimental results is not significantly impacted by thermal broadening to 77 K, at which the experimental data were obtained. This can be extrapolated by reference to Figure 5.19, which shows a more extreme case of thermal

broadening than is present in this particular example. This indicates that further detail in the model is needed to account for differences between the 300 K and the 77 K experimentally-observed dI/dV. Freezing of the pilus and water as they are cooled to 77 K decreases the ability of the pilus to move. Protein motion and reorganization of surroundings are important factors in the way biological molecules react to charge transfer processes, as discussed in the context of of Marcus theory in Chapter 4, and it can be speculated that the room temperature gap is raised to a non-zero density of states in the experiment due to small motions of the pilus or surrounding water below the spatial resolution obtained during this experiment. Since parts of the pilin subunit were found to be particularly flexible, as displayed in Figure 4.3, which the authors of that study suggest may impact the ability of the assembled pilus to accommodate bending [52], these regions of the pilin could be promising locations to consider further for this purpose.

In both theory and cryogenic experiment, the density of states is zero for a gap extent on the order of a few hundred millivolts. The unexpectedly wide gap in theoretical calculations could potentially be addressed by future calculations of an assembled pilus. The raising of the room temperature dI/dV above zero in the pseudogap region will likely require the incorporation of other physical processes into the model. In all, the calculations for the pilin subunit are not identical to the experimentally-determined dI/dV curves, but they share their most profound feature, a semiconductor-like gap in the density of states.

5.4.2 Biological Relevance

The pili have been previously proposed to behave as molecular rectifiers [22, 65]. In this scenario, there is a preferential direction for current to travel along the pilus, which could help prevent undesirable transport of electrons in the "wrong" direction into rather than

away from the bacterium. The offset of the gap center from 0 V indicated in Figure 5.13 demonstrates a smaller positive than negative voltage needed to reach the nonzero density of states region beyond the gap. Thus an electric potential established in one direction across the pilus would find the pilus more amenable to conductivity by providing more available electronic states, while a potential established in the opposite direction would need to be slightly greater in order to have electronic states available to use for conductivity. On the opposite edge of the pilus as shown in Figure 5.14, an asymmetry is also present between the positive and negative biases required to observe nonzero density of states. For that edge of the pilus, however, the gap is reproducibly slightly wider. This is consistent with the rectifying picture [22, 65] wherein current travels in a spiral direction along the pilus length. To address questions of current pathways directly, transport measurements such as those in Reference [25] are crucial. The pili were found to conduct ohmically in the longitudinal direction at room temperature [25] within the voltage regime considered in this work, suggesting that pseudogaps in the local density of states at room temperature do not seriously diminish pilus conductivity.

5.4.3 Potential Further Investigations

While significant progress has been made over the past several years on the properties of the pili in *Geobacter sulfurreducens*, there remain many more details to be dived into. In particular, the questions of what specific parts of the pili are most responsible for the conductivity can be addressed by futher scanning probe microscopy studies. Directed mutagenesis to produce pili which lack components which are suspected of being keys to charge transport in *Geobacter* pili, combined with transport measurements [25], as well as other sub-pilus studies can narrow down the most important contributors to conductivity in these pili. In

addition to suggestions of further research directions, potential improvements to the STM and conductive AFM [25] experimental configurations are discussed here.

Role of Tyrosines

A recent study [52] overlaid the experimentally-determined *Geobacter* pilin structure [53] onto a known pilus structure from another bacterium to model an assembled *Geobacter* pilus. This pilus model demonstrates that tyrosine amino acids from multiple pilins, shown for an individual pilin in Figure 4.3, are concentrated together periodically throughout the pilus, as can be seen in Figure 5.22. Since tyrosines are traditional culprits for biological charge transport [55], this strongly suggests that pili should have alternating spots of higher and lower density of electronic states. The pilin calculations by Prof. Dr. Feliciano show variation in the local density of states along the pilin [65]. This may be related to some of the periodic bright spots in STM images of the pili, and comparison between this model and data presented both here and in Reference [22] is presently in progress.

Higher-Resolution Imaging

While STM is capable of atomic resolution with relative ease, as shown in Figure 3.5, atomic resolution of the surface of protein structures such as the pili investigated here remains temporarily out of reach. In large part, this is due to the difficulties involved in sample stabilization. The pili in these experiments did not always thoroughly stick to the surface, sometimes losing contact with the substrate mid-scan, as in Figure 5.5. Adhering the pili more strongly to the surface could help stabilize them for high-resolution imaging [27]. This was not done in this work because a substrate for the pili with a well-known density of states was desired, as well as the minimum possible chemical perturbation to the pili. Often in

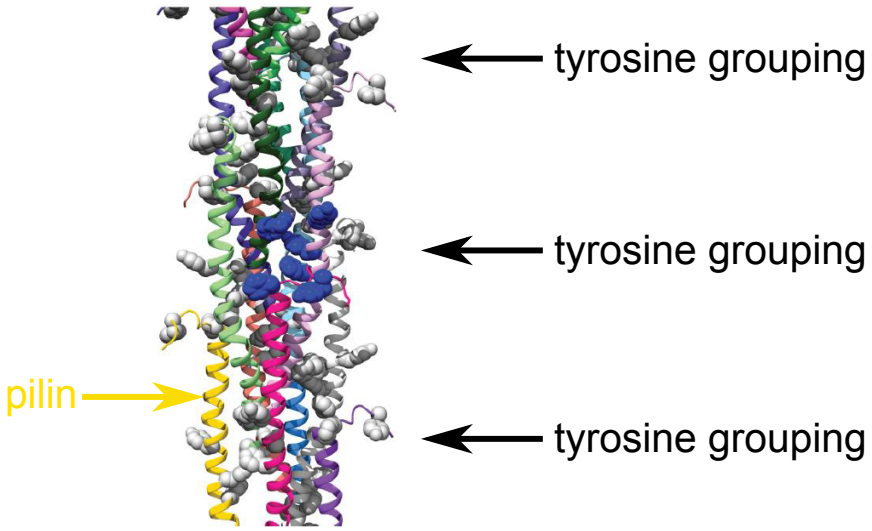

Figure 5.22: Periodic clusters of tyrosine amino acids in the assembled pilus model adapted from Reference [52]. This research was originally published in The Journal of Biological Chemistry. P.N. Reardon and K.T. Mueller. Structure of the Type IVa Major Pilin from the Electrically Conductive Bacterial Nanowires of Geobacter sulfurreducens. 2013; in press. Copyright the American Society for Biochemistry and Molecular Biology.

similar experiments, such substance which binds both to the protein and to the substrate is incorporated into the protein under study [80], although physisorption as was done here is also a common deposition strategy [75]. Now that initial work has been done on these pili such that their density of states in different circumstances is broadly predictable, adding other molecules to the sample to attach the pili to a substrate for higher-resolution imaging can be ventured.

Higher spatial resolution for spectroscopy on pili which stay in place on the surface could help disentangle relative contributions of separate pilins to the spatial dependence of the pilus density of states. If *G. sulfurreducens* pili prove to be molecular rectifiers (diodes) as proposed in References [22] and [65], it would be interesting to investigate whether these pili, without their originating bacteria to control their motion, tend to counteralign when forming bundles—in other words, whether the pili themselves have an electric dipole moment which would cause them to associate opposite to one another, much as magnets counteralign their

poles when brought close together—or whether they tend to align such that a bacterium with several pili intertwined in effect has a bundle of wires in parallel, hence decreasing the effective resistance of the bundle.

Temperature Dependence

While the present study focused on creating a large contrast between the two temperatures probed, 77 K and 300 K, in order to exacerbate temperature dependence for visibility of effects, future work can focus on smaller-scale temperature changes. Of particular interest is further observation of the freezing process and the effect of frozen versus liquid water on pilus properties. Since *Geobacter* bacteria are often found in sediments containing groundwater which could freeze, the behavior of pili under frozen-water conditions is environmentally relevant. It can be predicted that the density of states of the pili as observed in the 77 K frozen water scenario and presented in this work will be observed to be the same for all temperatures at which water is frozen, after accounting for thermal broadening effects as discussed above. If so, the metabolically-surmountable gaps observed in 77 K spectroscopy indicate that the pili could continue to participate in charge transport in the bacterial environment even when groundwater is frozen. This prediction can be tested by investigating the pili as the sample is slowly cooled in the temperature range around the freezing point of water, perhaps using, *e.g.,* a Peltier thermoelectric cooling mechanism.

Electrode Fabrication

Further tuning can be performed on the pilus longitudinal conductivity study of Reference [25]. In the interests of enhancing pilus–electrode contact, flakes of multilayer graphene could be used as an interface to the gold. In this vision, schematically sketched in Fig-

ure 5.23, flakes of graphene would be deposited onto the standard substrate of silicon with a 300 nm thermally-grown oxide layer as is commonly done for studies of graphene itself [81], comprised of different thicknesses and widths and scattered in no particular pattern on the SiO_2 substrate, then larger-scale gold electrodes would be sputtered through a shadowmask onto the substrate and graphene flakes. The sputtered electrodes would provide electrical conductivity to some of the graphene flakes on the substrate. Sputtering through a shadowmask, in which the material is laid down on the substrate everywhere except where blocked by a physical mask, obviates the need for the photolithographic procedure described in Appendix E. The conductive AFM measurement can then proceed as before [25].

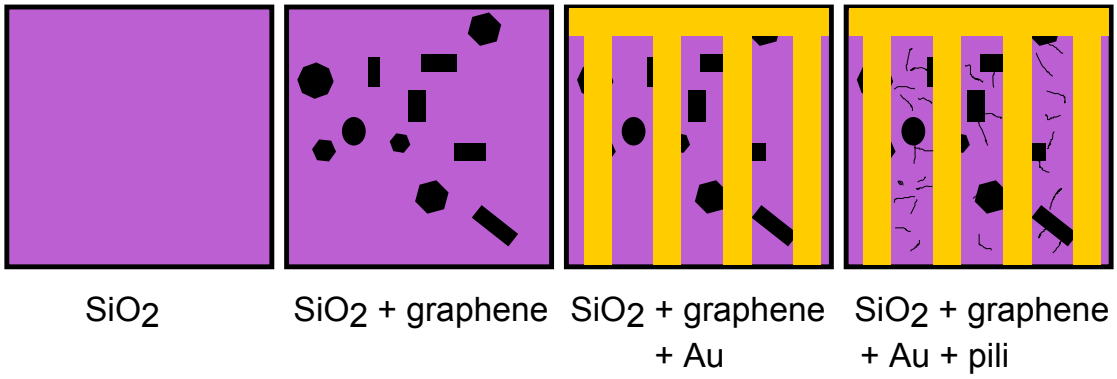

Figure 5.23: Suggested new electrode scheme for pilus longitudinal conductivity experiment [25]. The graphene flakes provide a more pilus-friendly interface to the gold electrodes. Diagram is not to scale.

Several advantages to this design can be envisioned, including the shorter height of few-nanometer graphene compared to 25 nm electrodes, the opportunity for pili to be wedged under the graphene flakes as a secondary method of achieving electrical contact. The chief advantage comes from the history of study of *G. sulfurreducens* pili on graphite surfaces, *e.g.,* [3, 22], and thus the better-established characterization of the pilus–electrode interface, as furthered by the research discussed here.

APPENDICES

Appendix A

Operation of an Atomic Force Microscopy User Facility

The MSU Center of Research Excellence in Complex Materials (CORE–CM) purchased a Cypher atomic force microscope/scanning probe microscope from Asylum Research, which was installed in September 2011. This Cypher AFM/SPM was to be operated as a user facility under the general supervision of Reza Loloee, but the opportunity existed for another person to take a strong role in the day-to-day operation of the facility, training users and providing first-line technical support. This Appendix documents some of the components of this work, as well as presenting a technique developed to extend the range of measurements for which the Cypher could be used.

A.1 Installation and Characterization

As a user facility instrument, this Cypher needed to be situated in a freely-accessible space. It was housed in an available small room until noise characterization measurements established that a more traditional lab space was necessary, at which point it was moved to its long-term home in B138 Biomedical and Physical Sciences Building. Since noise levels were the primary reason for moving the instrument, characterization of the noise was important to quantify the benefits of each location.

Since the scanning probe microscopy techniques pertinent to the research presented here are extraordinarily sensitive to the separation between the tip and the sample, it is extremely important to minimize vibrations of the system that could affect the tip–sample separation distance. The natural frequency of building structures, even in basements, is on the order of a few tens of Hz [30]. The scanning probe microscope should be vibration-isolated in such a way that this range of frequencies is damped out.

The sensitivity of the scanning probe measurement to ambient vibration depends on the measurement technique being used. The simultaneous operation of other equipment in the same lab as the Cypher was observed to disrupt STM measurements but did not significantly impact amplitude modulation AFM scans. For this reason, noise characterization tests are done with the AFM tip in mechanical contact with the surface. As an example, a portion of a noise characterization test is shown in Figure A.1. The Asylum Research control software for the Cypher monitors the motion of the cantilever due solely to noise while the tip is on the surface, and it plots the amplitude and the frequency distribution to aid in diagnosing noise sources. Noise in the frequency range of a few tens of hertz can generally be attributed to mechanical vibration [30], while electronic noise displays itself in a narrow band at 60 Hz and its higher harmonics, since this is the frequency of mains current in the United States.

A.2 Technique Development

The range of motion of the z piezo on the Cypher scanner places a limit on the heights of features that can be measured by this microscope. For the scanner on this particular Cypher, the z piezo range was measured to be 6.2 μm. A significant proportion of potential facility users, however, desire to measure heights ranging from several to several tens of μm.

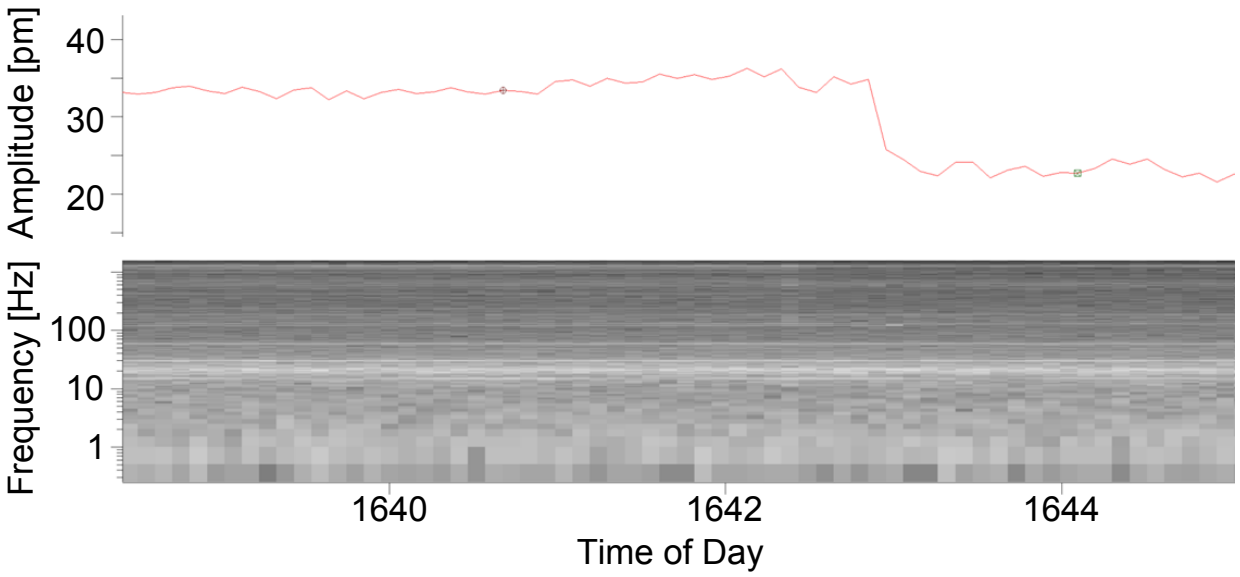

Figure A.1: Few-minute subset of a noise test. Top: Amplitude of the noise in picometers. Noise amplitude decreased when nearby equipment was turned off. Bottom: Frequency distribution. Mechanical vibration is evident in the broad band of noise around 20 Hz.

A workaround method to determine large heights was devised in collaboration with Scott MacLaren of the University of Illinois at Urbana–Champaign and members of the Asylum Research scientific staff, as worked out on the Asylum Research Forum [82].

The method, dubbed the Giant Step Height tool, involves focusing the optical microscope inside the Cypher on the top and underneath the sample. This is done most simply at an edge of a sample or at a trench scratched into a sample so that the sample mounting disk surface or the substrate underlying the sample can be focused on as the bottom surface. For transparent samples, the underlying substrate seen through the sample can be used for this measurement, although the index of refraction of the sample must then be considered. The optical encoder counts corresponding to the position of the focal point of the Cypher's internal optical microscope can be read out from the control software. These encoder counts are accurate to 200 nm [82], although scatter in visual determination of the in-focus locations of the sample top and bottom was empirically found to be the limiting source of uncertainty. Consequently,

the μm accuracy of the display on the Engage Panel within the software is sufficent for this method. For samples shorter than several μm in height but still uncomfortably tall for AFM, greater precision can be achieved by mounting a tip in the Cypher tip holder, as sketched in Figure A.2.

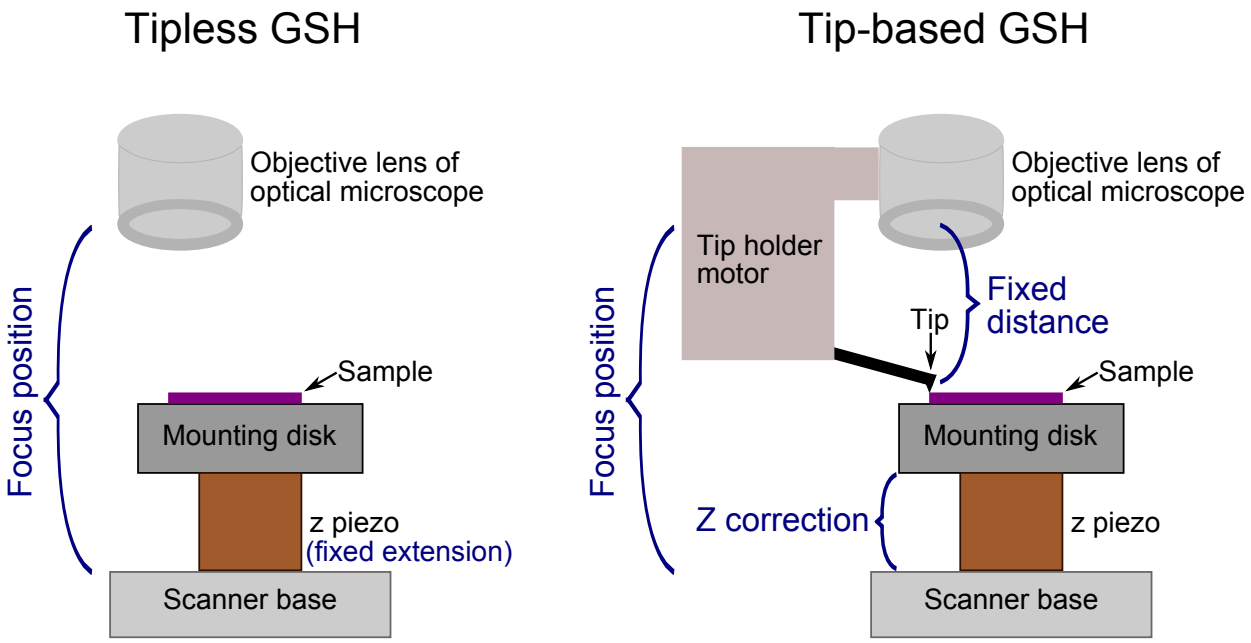

Figure A.2: Left: Diagram of optical-only GSH. The objective lens of the optical microscope is focused on the top and bottom of the sample, and the motor position of the objective is recorded at the point at which each comes into focus. Right: GSH with a tip in place. The focus of the objective lens of the optical microscope remains set on the tip, while the tip + objective is moved as a unit until the tip comes in contact with the surface of the sample. The motor position of the tip + objective is recorded. Because the tip–sample contact involves extension or retraction of the z piezo, the z piezo extension or retraction can be an important correction factor on the order of a micron, but involving the tip can give more precise measurements of few-micron heights.

Initially, a test of the procedure was done by measuring the height of a glass slide, correctly determining its height of 1.2 mm. Portions of screenshots used for the first GSH measurement are shown in Figure A.3.

The primary test of this method on a scientifically-relevant sample was done with the collaboration of Nathaniel Leonard from the MSU Department of Chemical Engineering and

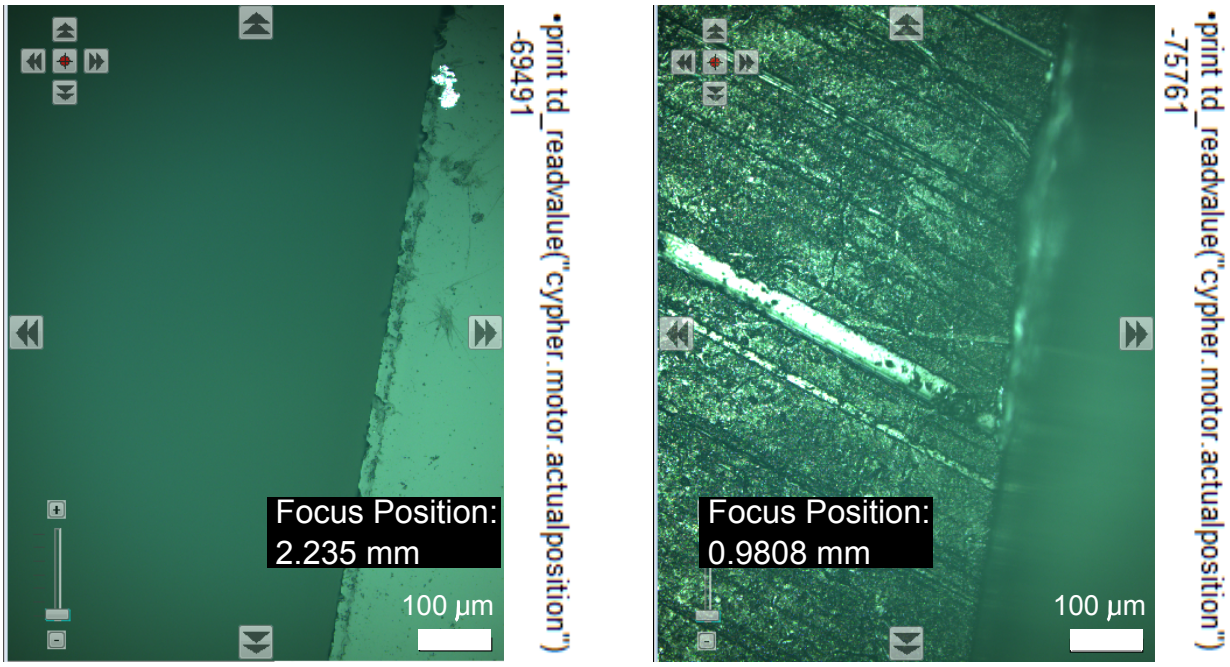

Figure A.3: Demonstration of the GSH method on a glass slide. Left: Focus on top of slide. Right: Focus on sample disk underneath slide. Difference between focus positions is 1.2 mm.

Materials Science. Mr. Leonard studies catalysts comprised of a pyrolyzed combination of iron, nitrogen compounds, and a porous carbon support, working towards a replacement for platinum-based catalysts for oxygen-reduction applications [83, 84]. The sample inks were created by dispersing catalyst in a Nafion + ethanol solution by sonication, using ethanol to dilute the solution to have different densities of the catalyst + Nafion system in the ethanol. After deposition of 5 μL of the solution onto a glassy carbon rotating ring-disk electrode [83, 84], the ethanol was permitted to evaporate. Before measurement, a razor blade was used to apply pressure laterally to the film, swiping it away from the glassy carbon electrode surface and leaving a crisp edge to use for the height measurement.

The samples were prepared by Mr. Leonard, and the determination of "in focus" was made initially by concurrence between the two experimenters to decrease the effect of personal perception. The scatter in perceived heights was greater than the 200 nm resolution of the

detector encoding the position of the optical microscope focus, yet both experimenters agreed on each focus position despite choosing slightly different surface features to focus on. Since the roughness of the sample was often in the neighborhood of a few hundred nanometers, comparable to the wavelength of the optical light being used to view the sample, this amount of height variation in focus did not materially affect the results.

Three measurements were obtained at each location on the samples, with locations selected to represent the center and edges of the films. Since the film covered the entire electrode except where it had been scraped away, the film edges were also at the electrode edges. It was observed through the optical microscope that the film was cracked in a manner reminiscent of parched ground, as seen in Figure A.4. This concurred with previous observations by the chemical engineering and materials science researchers, who had noted this as a characteristic of the films. It is therefore unsurprising that measurements taken towards an edge of the film and those obtained near the center could vary.

Table A.1 contains the data for GSH measurements of catalyst + Nafion film thicknesses. Quoted uncertainty is the standard deviation, calculated in Excel and rounded to two significant digits. After inter-rater reliability was established for the first three measurements based on independent consensus between the experimenters regarding the positions of the top and undersurface of the films, it was sufficient to have one experimenter continue the remainder of the measurements, beginning with the second 300 μg/cm^2 sample loading in Table A.1. The 200 μg/cm^2 sample loading and the first 100 μg/cm^2 sample loading in Table A.1 were done on a different glassy carbon electrode of the same type as the electrode used for all the other sample depositions.

Film thicknesses are shown in Figure A.5 as a function of sample loading. The alternate electrode average film thickness for the 100 μg/cm^2 loading was higher than, although still

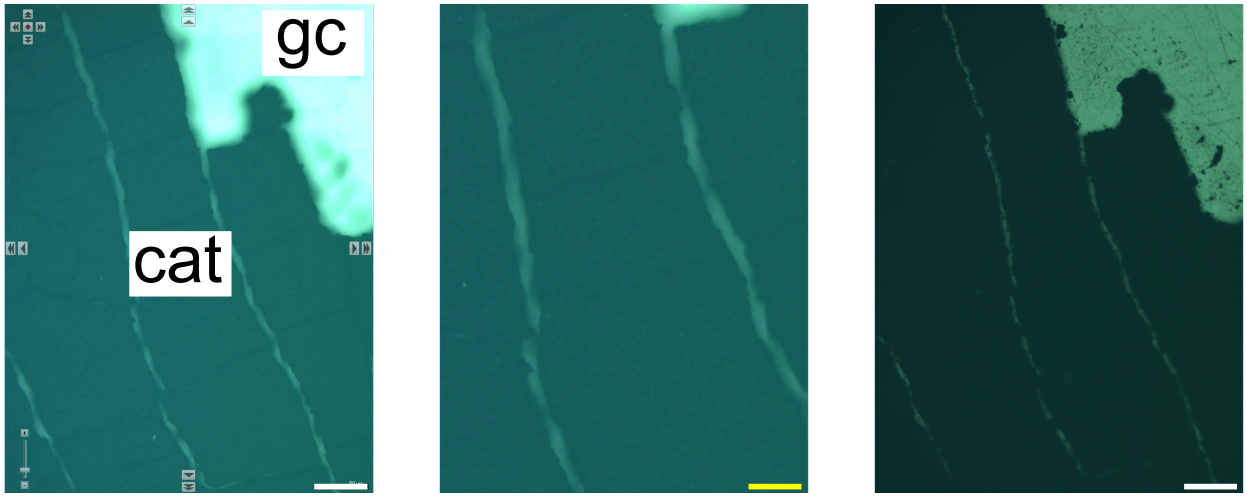

Figure A.4: Focus position determination on catalyst + Nafion films loaded onto glassy carbon rotating-ring electrodes. Left: Optical micrograph indicating the catalyst layer "cat" and underlying glassy carbon "gc" electrode. Scale bar is 50 μm. Center: Optical micrograph focusing on the top of the catalyst, digitally zoomed to twice the magnification of the left and right images for ease of discerning features during focusing. Scale bar is 25 μm. Right: Optical micrograph focusing on the underlying electrode. Scale bar is 50 μm. Brightness differences among these images are due to the light levels used to aid in focusing.

consistent with, those measured on the usual electrode. The film thicknesses for the 300 μg/cm^2 loading determined by one experimenter (lower value in the plot in Figure A.5) and by both experimenters (upper value) using two different depositions of the sample on the same electrode with the same loading were consistent within uncertainty, implying that there was a sufficient amount of inter-rater reliability in the height determination perceptions. A sample series of screenshots of the optical microscope images used for the GSH measurement is presented in Figure A.4.

The tipless, or optical focus depth, GSH measurements were confirmed for some of the samples by including the use of an AFM tip to determine the location of the surface, rather than relying on optical focusing. These methods are compared in Figure A.2. For tip-enhanced GSH, the tip was engaged on both the upper and the lower surfaces in turn, with the optical microscope set to maintain its focus on and move with the tip, and the difference

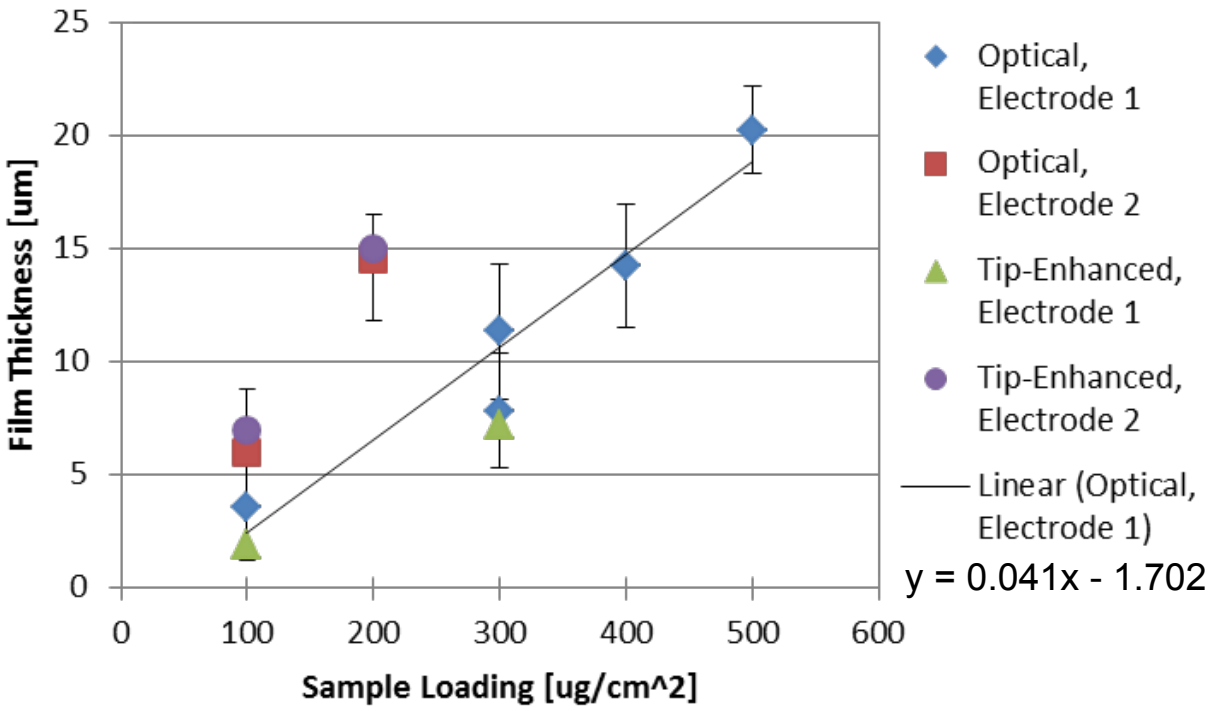

Figure A.5: Height measurements of catalyst + Nafion films loaded onto glassy carbon electrodes using both optical focus depth GSH and tip-enhanced GSH. A linear fit was made to the data acquired using Electrode 1, showing a linear dependence of film thickness on sample loading. The alternate electrode, Electrode 2, appears to have a slightly greater slope, but there were not enough sample loadings using that electrode to determine this definitively. Within statistical uncertainty, the optical and tip-enhanced methods are equivalent.

in optical microscope position was measured via encoder counts [82]. In addition, during this process, it was determined that the cantilever deflection contributed appreciably to the measured heights when using this method for film thicknesses of only a few microns, since the range of the z piezo was 6.2 μm. To calculate the correction to the height using the tip-enhanced GSH method, use

$$\begin{aligned} \text{Z correction } [\mu\text{m}] &= -(Z_{top} - Z_{bot}) * \frac{\text{z } piezo\ full\ travel\ range}{voltage\ range\ of\ \text{z } piezo} \\ &= -(Z_{top}\ [\text{V}] - Z_{bot}\ [\text{V}]) * \frac{6.2\ \mu\text{m}}{160\ \text{V}} \end{aligned} \tag{A.1}$$

where Z_{top} and Z_{bot} are the z piezo extension voltages on the sample top and the surface underlying the sample, as observed during the measurements. The correction is negative because a positive value of the z piezo extension causes a decrease in the relative objective lens–sample separation. For shorter films, this more precise tip-enhanced GSH using the optical encoder count measurement was performed and compared to the optical-only method. Results of the comparison are shown in Figure A.5, showing that tip-enhanced GSH results fall within the uncertainty determined by multiple measurements using the optical measurement. The uncertainty in the z piezo extension determination was such that only two significant figures, with some uncertainty, in the correction can be claimed, so no error bars are shown for the tip-enhanced GSH data in Figure A.5.

A.3 User Training and Troubleshooting

In addition to experimental design and technique development for the aforementioned measurements and staff-assisted sample scanning, this role included responsibility for the first line of troubleshooting on the apparatus and for interacting with Asylum Research technical support as needed.

A.3.1 User Training

The Cypher was intended to be operated as a user facility. In order to insure safe and effective operation of the microscope, users were required to undergo training, which necessitated the development and coordination of training sessions. Over the course of two years, several users were trained to a level enabling them to operate the AFM independently, not only for the standard amplitude modulation in air mode but also for more complicated modes of op-

eration. In addition, verification and validation of the independent trainings of further users was performed. An efficient and sustainable method for training needed to be developed. To this end, several instructional videos were created to aid in training future users. These were produced both independently and in collaboration with Reza Loloee or Victor Ramirez.

Assisting with experimental design is an important component of proper user training. Significant input into the experimental design was provided for experiments by users from a variety of different departments and different colleges within the university. In addition, staff-assisted scanning was performed on samples from a similar diversity of departments. This is a facility-provided service whereby researchers who only need a few samples scanned, or whose projects require advanced techniques, bring their samples to be scanned rather than becoming trained as AFM users.

A.3.2 Troubleshooting and Maintenance

Part of facility operation consists of maintaining the equipment in proper working condition and identifying and addressing issues. The Cypher controller developed a malfunction that required its return for repair. The troubleshooting process surrounding this malfunction involved disassembling and removing components of the electronics for testing in collaboration with Asylum Research technical support. This procedure provided the very interesting opportunity to interact with the "inner workings" of the Cypher control electronics.

Conductive AFM I–V measurements used the dual-gain ORCA cantilever holder, which includes one preamplifier with a sensitivity set to measure currents in the range of $\pm$ 10 nanoamperes and another preamplifier for currents in the range of $\pm$ 10 μA. It was observed that when the 10 nA preamp was saturated with current, "ears" would appear in the current reading of the 10 μA preamp, as seen in Figure A.6. This had also been independently

observed by another dual-gain ORCA user and by Asylum Research technical support [85] and was identified as cross-talk between the preamplifiers.

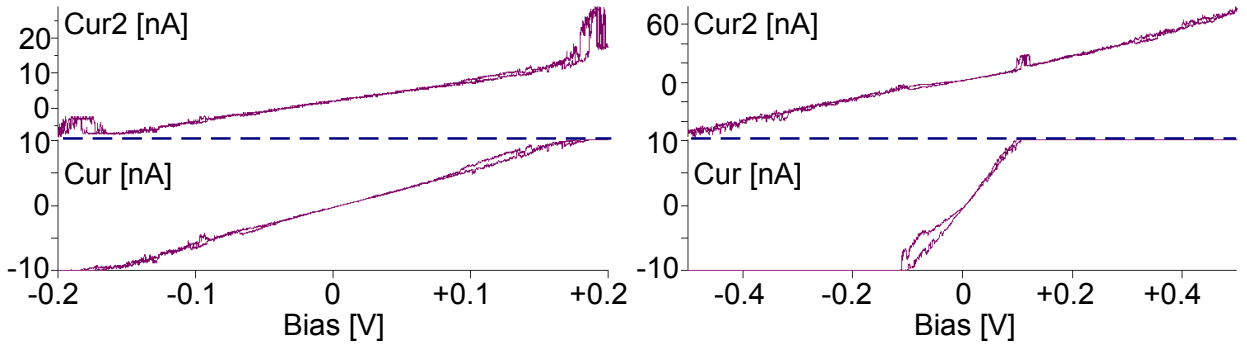

Figure A.6: I–V curves demonstrating the "ears," adapted from a post to the Asylum Research Forum [85]. Left: $\pm$ 0.2 V bias sweep. Right: $\pm$ 0.5 V bias sweep. Both: The I–V curve on top is as seen by the 10 μA preamp, and the I–V curve on bottom is as seen by the 10 nA preamp, separated by a dashed line for clarity. Horizontal lines in the lower I–V curves occur when the 10 nA preamp is saturated. The onset of this saturation corresponds to the "ears" in the upper I–V curves.

Loading [μg/cm^2]	Location on Sample	Layer Height [mm]	$\pm$ [mm]
500	1	20	0.47
	2	24	1.6
	3	16	0.94
400	1	17	1.2
	2	14	2.4
	3	12	0.0
300	1	16	2.9
	2	7	0.82
300	1	12	2.5
	2	3	0.47
200	1	21	0.47
alternate electrode	2	4	2.5
	3	19	0.94
100	1	0	1.4
alternate electrode	2	5	1.4
	3	13	1.6
100	1	5	0.47
	2	3	1.9
	3	3	1.2

Table A.1: GSH optical focus depth measurements of catalyst + Nafion film thicknesses, using the change in position of the optical microscope focus to determine the film heights.

Appendix B

Artifacts That Almost Thwarted Me

Since visual searches of data begin with a query in mind—*e.g.,* "Is there a pilus in this scan?"—before searching the image to answer the question [86], looking for pili primes the researcher to focus on pilus-like features in scans, which may be artifactual. For this reason, this Appendix presents several examples of artifacts, that they may be more easily recognized as such in future work. Just as the examples of pilus topography shown in Chapter 5 provide priming for future searches for pili on the surface using STM, these examples of artifacts can provide references to assist in pattern recognition when checking for artifacts in future work [87]. Additionally, presenting artifacts and actual pilus topography in the same document can build connections to bring to mind both genuine pili and common artifacts when observing nanowire-like filamental features, thus providing an aid to feature identification by priming the future worker to recognize both pili and common artifacts [88, 89].

While distinguishment of artifacts from genuine pili can be done to some extent based on feature topography, the proof is in the spectroscopic pudding, so to speak. This is particularly important when searching for nanowire-like objects on a graphite substrate, as graphite is known to produce nanowire-like artifacts [89]. No matter how pilus-like a feature may look, its density of states will betray its identity. Relying on the spectroscopy for object identification comes with its own requirements for vigilance; contamination or unstable behavior of the tip or sample result in uncharacteristic spectroscopy. For this reason, reproducible results are the most important safeguard against being tricked by artifacts.

Although graphite is a popular substrate for STM studies of biological materials (the first STM studies on DNA [90] used a carbon film substrate instead of the highly-oriented pyrolytic graphite, HOPG, more commonly in use today), it has a tendency to produce multifarious artifactual formations which can be highly reminiscent of biological features [89]. Since STM-on-graphite experiments have been performed for roughly three decades, the database of such formations is well-developed, even if some of the artifacts are still not fully physically explained [46].

B.1 Step Edges

The accumulation of graphitic debris along graphite step edges can lead to artifacts which appear at first glance very similar to pili. In particular, they tend to be a few nanometers in width, comparable to expected pilus widths. In addition, the instability of this debris leads to spikes in the tunneling current as the feature is scanned over, thereby masking the true height of the feature. When the step edges are distinct and have sharp edges, as in the two examples in Figure B.1, these are easier to identify quickly as artifacts. For this reason, careful nearly-real-time image processing can be a helpful practice, as short step edges may be difficult to identify as such without subtracting a background tilt of the sample.

A particularly insidious example of artifactual behavior comes with step edges which are not straight. One of the criteria that helps differentiate elongated carbon nanostructures from biological nanowires is the tendency of carbon nanostructures to be straight over longer distances, although this is not a hard and fast rule. When flakes of graphite laying atop a more uniform graphite substrate have edges which are curved, particularly edges along which debris has accumulated as described above or edges which show ridge behavior, as

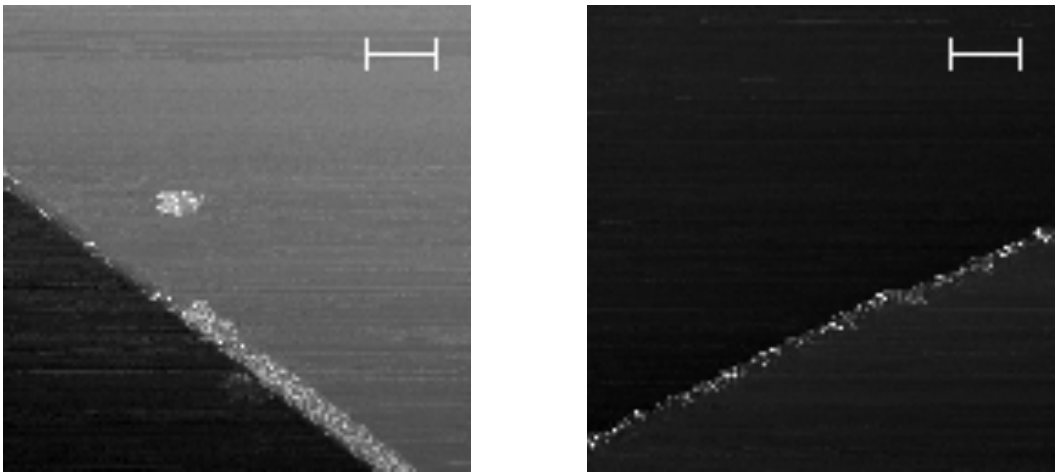

Figure B.1: Typical artifacts at graphite step edges on two different parts of a sample. These are not pili lying against the step edges but rather are graphite formations. Scale bars are 200 nm. Left scan (+ 0.5 V, 0.5 nA), right scan (+ 0.5 V, 0.4 nA)

discussed in Reference [46], the more subtle indication that the flake area is higher than its surroundings may seem less convincing evidence than the curvedness of the edge. Further, the aforementioned tunneling current spikes due to the debris can make it particularly difficult to determine the relative heights of the flake and the underlying graphite, since spikes tend to dominate the height scale in linecuts across the edges.

In addition, the density of states can be enhanced at the edges of some graphite steps due to topological effects [91]. Since STM topographs are a convolution of surface height with the local density of states of the sample, these can make the edges appear "taller" or brighter in the STM image, solely due to electronic enhancement. This is a potential explanation for the artifact on the right side of Figure B.1.

Alternatively, step edges can be stably imaged but possessed of deceptively periodic lumpy protrusions as though the edges were crimped, as is seen in Figure B.2. Despite the lumpiness, identification of this as a step edge is straightforward based on the surrounding topography–the upper right half of the images in Figure B.2 is lower than the lower left half,

with the boundary marked by the lumpy feature. The periodicity of such step edge can even mimic a chiral pattern [89], making it particularly important to detect when artifactual so as not to confuse this with pilus structure.

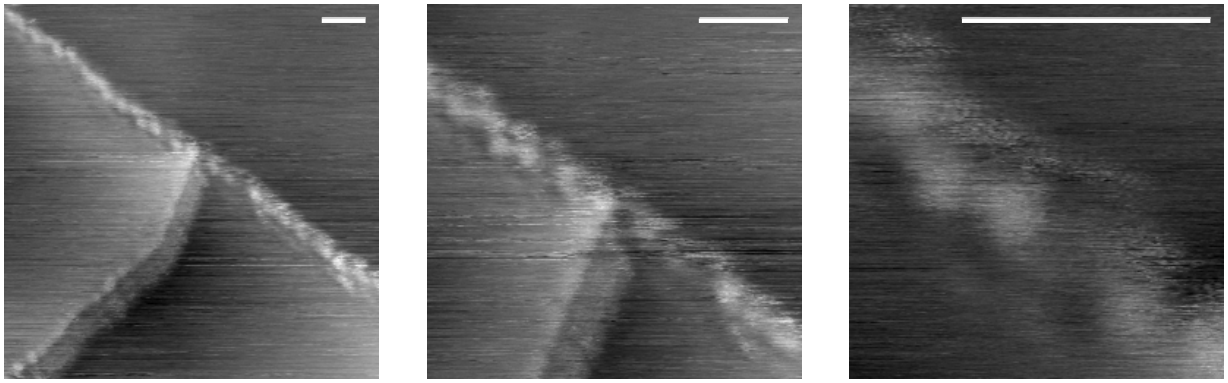

Figure B.2: Three scans of a step edge, possessed of a deceptively lumpy structure along the diagonal from upper left to lower right. The level of visible detail, obtained by decreasing the scan size, increases from left to right. Scale bars 10 nm. (+ 0.5 V, 0.2 nA)

B.2 Vertebral Shape

A more insidious artifact seen in the course of this research at low temperature bore a strong resemblance to a column of vertebrae and is shown in Figure B.3. A similar structure was observed by Veazey [22] at room temperature on a similar sample as a zipper shape. The aspect of this artifact that made it most perilously misleading was that it had a similar breadth and only a slightly shorter height to that customarily seen for pili and multiple periodic substructures, as were commonly observed in well-resolved pili. The non-pilus identity of this object was eventually realized due to its spectroscopy often appearing similar to spectroscopy on graphite and, more tellingly in this particular instance, based on the topographic merging of the feature with a nearby graphite step edge, as seen in Figure B.3. Because atomic resolution was not obtained under these specific conditions, observation of

the atomic lattice structure in the vicinity of this artifact was not possible, thus precise identification of the origin of this artifact remains in the realm of speculation. This feature may be a graphite grain boundary, where the density of states is electronically enhanced as the direction of the graphite lattice changes its angle. Grain boundaries in graphite, where two different orientations of the graphite lattice meet in a way analogous to magnetic domain walls, produce periodic structures along the boundary as the mechanical deformation due to stresses causes periodic defects which lead to an enhancement in the local electronic density of states near the Fermi level, thus causing a periodic "ridge" in the image due to electronic effects rather than actual physical height [92].

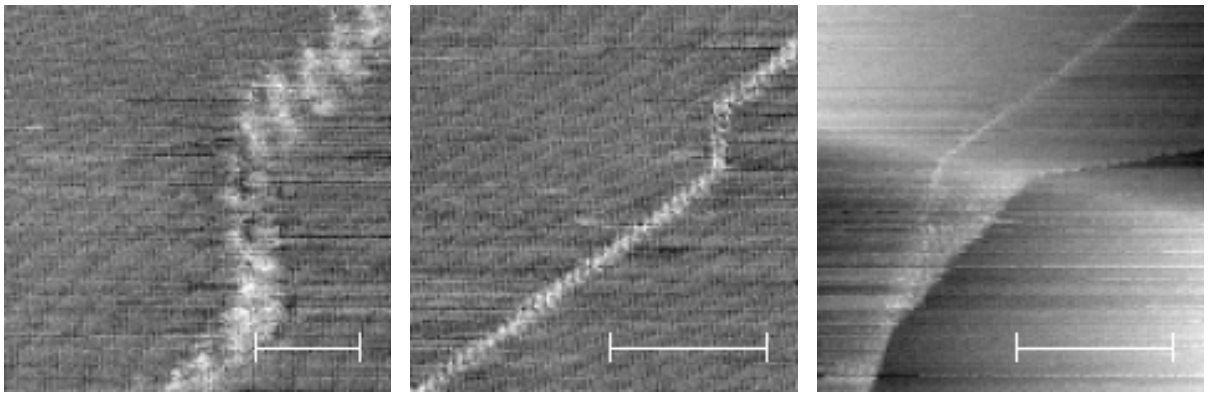

Figure B.3: Artifact comprised of periodic shapes reminiscent of vertebrae in a spinal column. Left: Close-up of comma-shaped "vertebrae." Scale bar is 10 nm. Center: Larger scan demonstrating the abruptness of the dislocations. Scale bar is 50 nm. Right: Relation of the vertebral shape to a nearby step edge. The vertebral shape apparently merges into the step edge near the bottom of the scan. Scale bar is 100 nm. (+ 0.5 V, 0.08 nA)

B.3 Tendriloid Ripples of the Graphite Surface

Tendril-shaped ripples in the graphite surface can also mimic the shape and approximate diameter of pili, although they are far shorter, often much less than a nanometer tall and

some fraction of the expected apparent height of the pili. They are not necessarily straight over long distances, and this vermiform waviness of some of these artifacts can cause additional confusion with the flexible biological nanowires. This was the most common artifact observed. The weak van der Waals attraction between the two-dimensional graphene layers that are stacked to form a graphite crystal is not always strong enough to keep the graphene layers mechanically stable with respect to one another. The perturbation due to the strong electric field between the tip and the sample, particularly pronounced due to the small area of the apex of the tip [30], can deform the graphite locally, applying shear forces in the many-megapascal regime [46]. Indeed, the tip–sample interaction is strong enough that it can be used deliberately to perturb the graphene layer atop the rest of the bulk graphite, lifting it up or folding it over [93]. These ripples are particularly prevalent in areas where the graphite has been disturbed, as is seen in the center of Figure B.4, where a perturbation in the graphite surface has has a relatively large number of ripples in its vicinity.

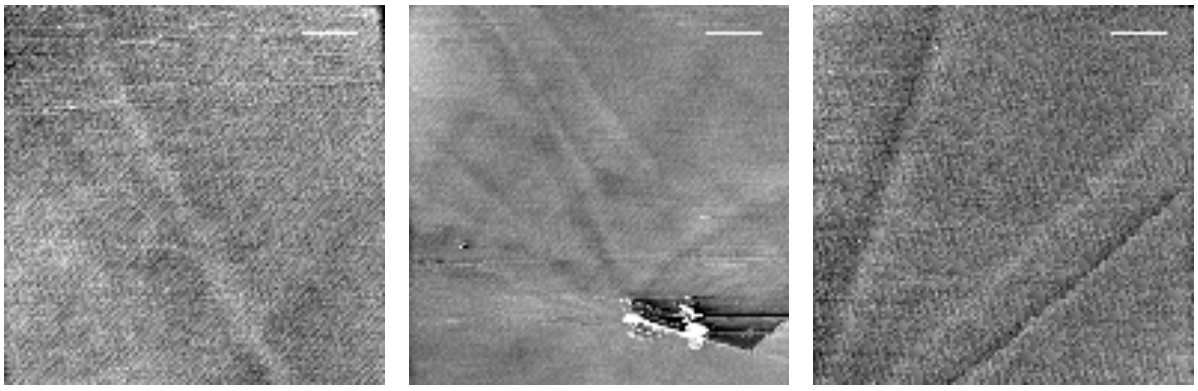

Figure B.4: Left: Tendriloid graphite ripple of approximately the apparent diameter and one half to one third the apparent height expected for a pilus on graphite. Center: These ripples can be provoked by disruptions in the graphite surface. Right: Several tendriloid artifacts, showing a variety of the shapes they can assume. Scale bars 100 nm. (+ 0.5 V, 0.08 nA)

B.4 Other Topographic Snares

In addition to the nanowire-like corrugations of the graphite surface mentioned above, graphite can show "superlattice" behavior, in which the STM image shows a pattern of bright and dark spots in the shape expected for the graphite lattice but with incorrect dimensions, due to issues during the growth or cleavage of the graphite sample [46]. It is useful to be aware of this effect to avert worries about piezotube calibrations. It is also profitable to expound further upon multiple-tip effects, as these are quite prevalent artifacts.

B.4.1 Graphite Superlattice

Graphite artifacts are not solely nanowire-like; sometimes, the distortions cause false lattice-like patterns, such as the hexagonal pattern in Figure B.5. Because of the hexagonal pattern, it is instinctive to assume initially that this is the atomic lattice of graphite; however, the apparent atomic size and spacing is too large. One could speculate that the scanning piezotube had suddenly lost resolution and was only scanning over a far smaller than instructed distance or that the tip had somehow become mechanically mired in place. The reproducibility of this image, the sharpness of the step edge as seen in Figure B.5, and the fact that subsequent scans in different areas displayed the expected nm/V resolution argues strongly against this. According to the conventional explanation, that's a Moiré pattern caused by interactions between the topmost and second of the overlapping sheets of graphene, which stack atop each other to comprise the graphite crystal. When the topmost sheet is rotated with respect to the sheet underneath it, the interactions cause the formation of a Moiré interference pattern; also, strain in the graphite lattice can cause buckling that results in a similar Moiré pattern [46].

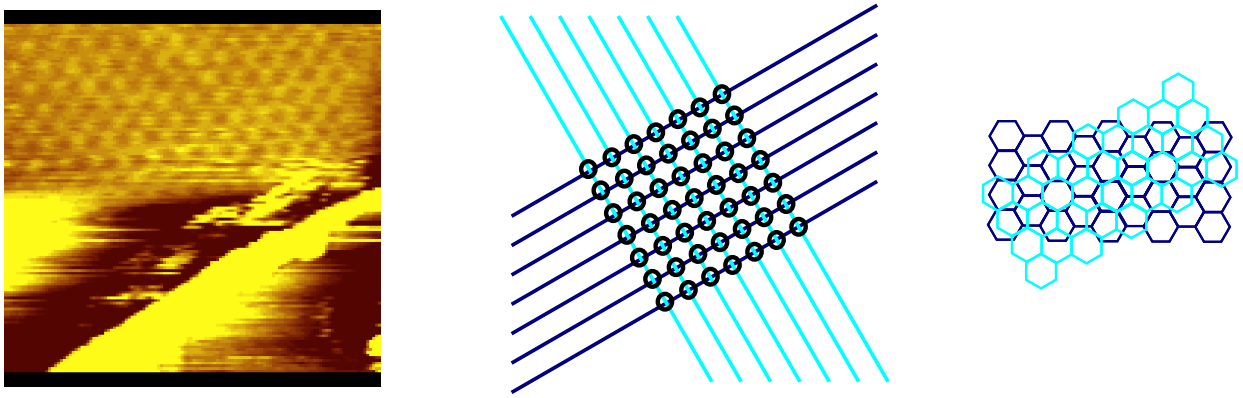

Figure B.5: Left: Hexagonal pattern on graphite due to a Moiré pattern from interference between overlapping graphene sheets. A line has been subtracted from each line of the image, and the displayed height shading range has been truncated to emphasize the hexagonal pattern. Scan size for left image is 244 nm × 298 nm. (+ 1 V, 0.08 nA) Center: Diagram of a Moiré interference pattern. Light and dark lines represent lines of atoms in two overlapping layers of single-atom thickness. Circles at the intersections indicate the locations where the enhanced electronic signal from the overlap would be detected as a pattern. Right: Diagram of a Moiré pattern for a hexagonal lattice such as graphite. Lattices have been rotated by 30° for visibility; actual rotation for the pattern observed here would have been much smaller.

In this experimental observation of a graphite superlattice, the bright-spot spacing was approximately 100 times that of the actual atomic spacing of graphite, as shown by the comparison of image sizes showing similar periodicities in Figure B.6. Following Reference [46], the rotation angle can be determined via

$$\theta_{\text{rotation}} = 2\ arcsin\left(\frac{1}{2}\ \frac{atomic\ \text{spacing}}{bright\ spot\ \text{spacing}}\right) = 2\ arcsin\left(\frac{1}{2}\ \frac{0.246\ \text{nm}}{21.4\ \text{nm}}\right) = 0.6^{\circ} \qquad \text{(B.1)}$$

showing that this observed pattern in Figures B.5 and B.6 would be due to a very small rotation angle between overlapping sheets. This could either suggest that the top layer of graphite was generally very well-matched to the underlying layers in terms of rotation or that the Moiré pattern was not caused by the relative rotation of layers of graphite but rather by some other process such as lattice strain.

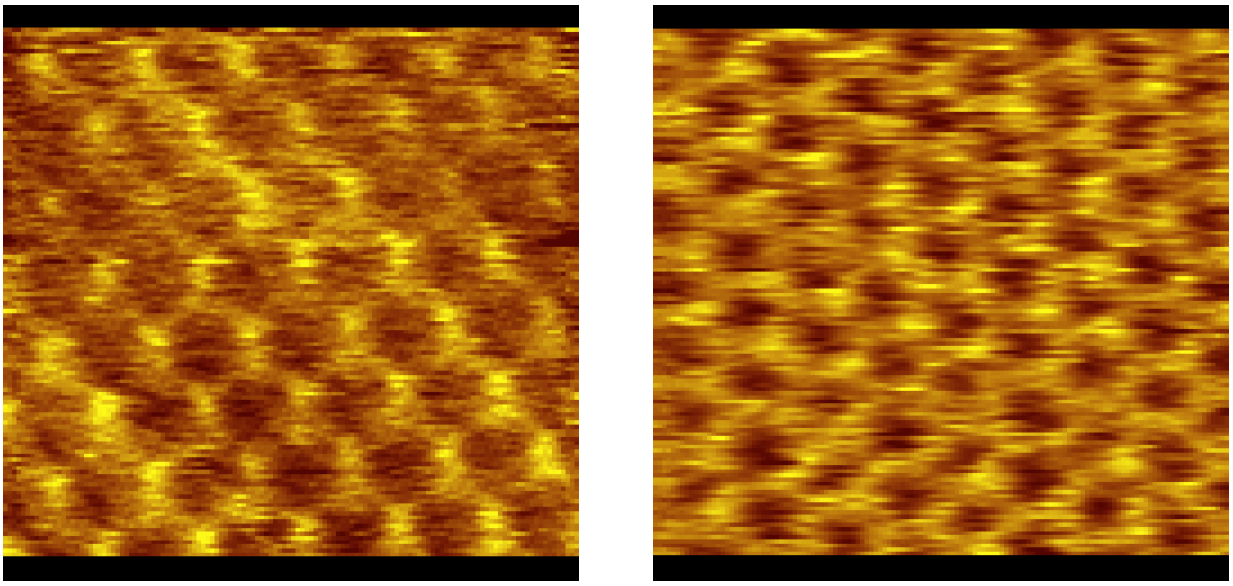

Figure B.6: Moiré pattern and graphite lattice comparison. Left: Zoom in on hexagonal pattern from Figure B.5. Image size 123 nm × 147 nm. (+ 1 V, 0.08 nA) Right: Atomic resolution scan of the graphite lattice. Image size 2.1 nm × 2.6 nm. (+ 0.1 V, 1 nA) The left image is nearly an order of magnitude larger than the right image along each direction, yet the patterns appear nearly the same size, indicating the artifactuality of the left image.

B.4.2 Multiple-Tip Effects

As mentioned in Chapter 2, multiple-tip effects can cause the illusory appearance of more features than are actually present. A frequently-seen imaging artifact in this research was a repeated apparent image of pili when found on the surface, caused by more than one nearby "minitip" at the end of the STM tip. In scenarios such as that in Figure B.7, a useful metaphor may be trying to play a phonograph record using an upside-down porcupine as the needle. Generally, due to the exponential drop-off in tunneling current with increased tip–sample separation, there are only two or perhaps three competing minitips at the end of a multiple tip. This was seen in studies using the cryogenic-capable STM and the Cypher STM, as it is one of the most common STM artifacts. A particularly egregious example of this echo-like repetition of features in a scan is given in Figure B.7. Careful observation of the bends of the objects in this image show that there are multiple tips along different

lateral directions. Confirmation that this is not the actual surface topography comes from observing the same echoing pattern on separate features in the image. Disentangling the number of minitips involved in producing this image is a task for the sharp-eyed; an attempt in one direction only is made in Figure B.7. The customary response to such a scan image is to endeavor to recover the tip or to replace it entirely.

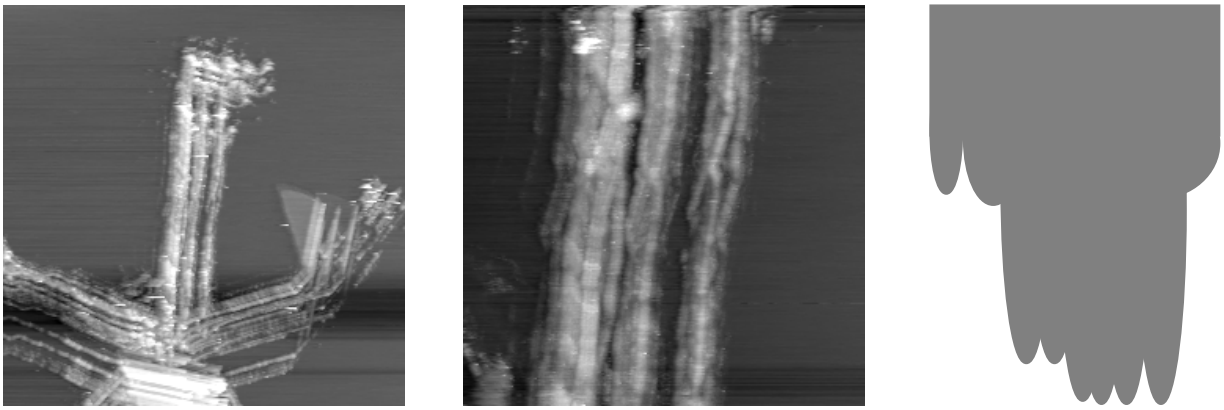

Figure B.7: A particularly dramatic example of a multiple tip. Left: Scan showing multiple repetitions of features. From this scan, it appears there are at least three tips close in height to each other and aligned approximately in the horizontal direction, slightly angled towards the upper left of the image, and several additional tips approximately along the vertical direction. Scan size 500 nm × 500 nm. Center: 150 nm × 150 nm scan near the middle of the scan on the left. The approximately-horizontal multiple tips are even greater in number, as another nearby tip is causing an overlapping echo on the leftmost of the three main feature repetitions, as well as causing two fainter echoes to the left of the three. (+ 0.5 V, 0.2 nA) Right: Artist's conception of a tip which could produce the horizontal multiplicity shown in these images; multiple tips along the other direction are not considered in this sketch. Only the protrusions near the very end of the tip are relevant—in this sketch, there are six such—due to the exponential dependence of tunneling current on tip–sample separation.

B.5 Artifacts in Spectroscopy

The health of an STM tip for spectroscopy can be evaluated by dI/dV measurements done on the graphite substrate on which the sample was deposited. A clean graphite surface with a clean, stable Pt:Ir tip should produce spectra with V-shaped dI/dV curves, like those shown

in Chapters 2 and 5. If the tip had acquired a contaminant while scanning the surface, the spectroscopy could then take on the characteristics of that contaminant.

Alternatively, if the contaminant cluster of particles were small enough, perhaps a few nanometers in diameter [94], that it acted as a small capacitor, a "Coulomb staircase" [95] could be observed in the spectroscopy. This could potentially explain the example in Figure B.8. While this spectrum is not a precise example of high-quality Coulomb staircases as may be seen in, *e.g.,* Reference [95], this could be because the formation of the Coulomb staircase is an unfortunate side effect of a mesoscopic particle cluster on the tip rather than being deliberately designed. Note that the particle cluster does not need to be an alien substance; it can simply be a slightly-detached cluster of tip atoms with only a very small, confined pathway leading to the rest of the body of the tip. The periodic peaks in the dI/dV spectra come about because the mesoscopic structure acts capacitively; it only passes the tunneling current on to the tip once its own energy levels have filled. The peaks are due to the resumption of current flow once the structure's energy levels are filled.

When a few atoms on the surface of the tip near its apex are not thoroughly connected to the bulk material of the tip and can move somewhat freely along the surface of the tip, the potential exists for these atoms to move into or out of the tunneling gap, thus changing the effective tip–sample separation distance, which can drastically change the amount of current detected. If a group of atoms farther away from the apex of the tip are not firmly connected to the rest of the tip body, this satellite chunk of atoms can wobble back and forth, changing the tip characteristics. A primary symptom of this is unstable spectroscopy, as shown in Figure B.9. The wide variety of slopes in the I–V curves in that figure shows that the tip–sample effective distance, which scales the tunneling resistance, is changing between curves. Careful examination of the zero-current line in the I–V curves in Figure B.9 shows

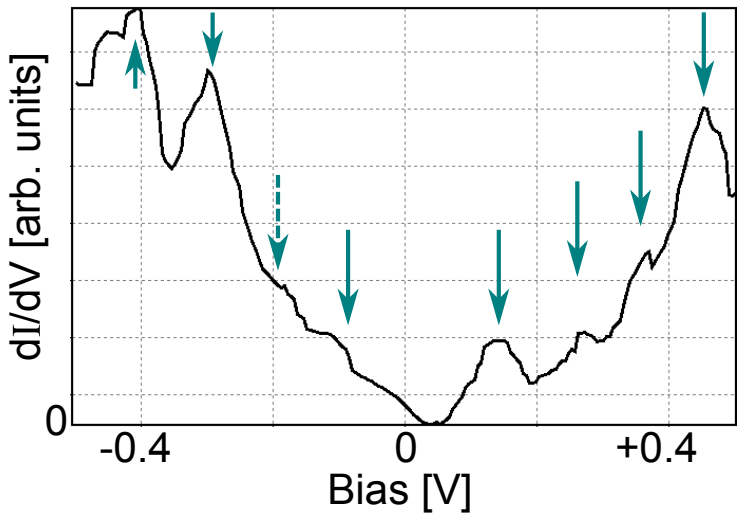

Figure B.8: dI/dV reminiscent of the Coulomb blockade effect convolved with proper graphite spectroscopy. Repeated peaks at symmetric spacings along the voltage axis are the chief diagnostic symptom, indicated with arrows. The offset of the bottom of the spectrum from 0 V could be due to Fermi level pinning due to contaminants on the surface.

that several of the curves do in fact show consistently zero current as the voltage is swept; equivalently, these curves hug the bottom of the dI/dV plot. This occurs because the tip–sample separation is set before each voltage sweep, with the voltage set at the scanning bias voltage level, and the feedback is turned off during spectroscopy. Although the tip and sample generally reach an equilibrium separation during this time, the changing voltage during the voltage sweep changes the electric field between the tip and the sample, which can tug unstable particles into different locations. This can push a few atoms at the end of an unstable tip out of the tunneling gap, thus increasing the tip–sample separation such that no current is detected, or *vice versa*.

Small portions of the sample can be adsorbed onto the tip, particularly those which are loosely bound to the surface and attracted to the strong electric field between the tip and the sample. Changes to the tip state, which can occur even in the middle of an individual scan, can have significant effects on the position of peaks in the dI/dV measurements, causing

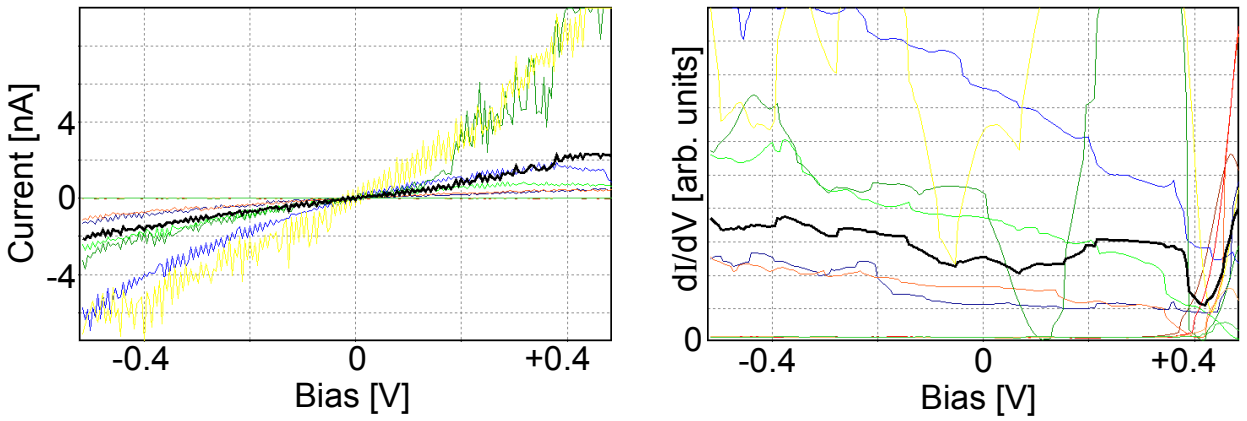

Figure B.9: Example of spectroscopy with an unstable tip. This dataset sums together two spectroscopy points on graphite, which should result in a sigmoidal shape for the I–V curves in the left image and a slightly rounded V-shape for the dI/dV curves in the right image. The thicker, black line is the average of the spectra. Left: I–V curves. Right: Corresponding dI/dV curves, obtained directly using a lock-in amplifier. The curves are not reproducible.

irreproducibility in the measurements [96]. For this reason, it is important to perform control spectroscopy measurements before and after spectroscopy measurements performed on a feature of interest in order to verify the pure quality of the tip. Figure 5.12 is convincing in no small part due to the proper graphite spectroscopy acquired immediately before and after the spectra acquired on the pilus. In multiple cases throughout this research, the "before" graphite spectroscopy looked as expected and the spectra on the pilus candidate looked non-graphitic, but the "after" graphite showed signs of looking like the pilus candidate spectra. It can be hypothesized that portions of the sample had transferred to the tip in those instances.

B.6 Multi-Characteristic Artifact

As a summary exhortation to believe a candidate feature is actually a pilus based upon dI/dV spectroscopic identity with possible corroboration from other ways of interrogating the sample, such as topography, rather than the other way around, this cautionary example is here presented. This object shared most characteristics with what were considered to

be authentic pili and was often misidentified as such upon preliminary analysis. While topographic scanning is an effective way to discover pilus *candidates*, classification of such as authentic *pili* rests on the shoulders and peaks of spectroscopy.

The topographic characteristic most prominently shared between this object and previously-observed pili is multiple nested periodicities approximating those observed for protein nanowires. Such an extensive level of topographic similarity between filamental biological objects and artifactual propensities of graphite is precedented [89]. Suspiciously, the object shown here was straight over at least 2 μm, save for dislocations where it zig-zagged as though relieving stress between mismatched lattice boundaries, as seen in Figure B.10. Enhancement of the local density of states at grain boundaries on graphite, leading to increased feature brightness in STM scans, as well as producing artifacts with small and large periods as the stress at the boundaries is relieved, is a well-known graphitic artifact that could be responsible for such an image [92].

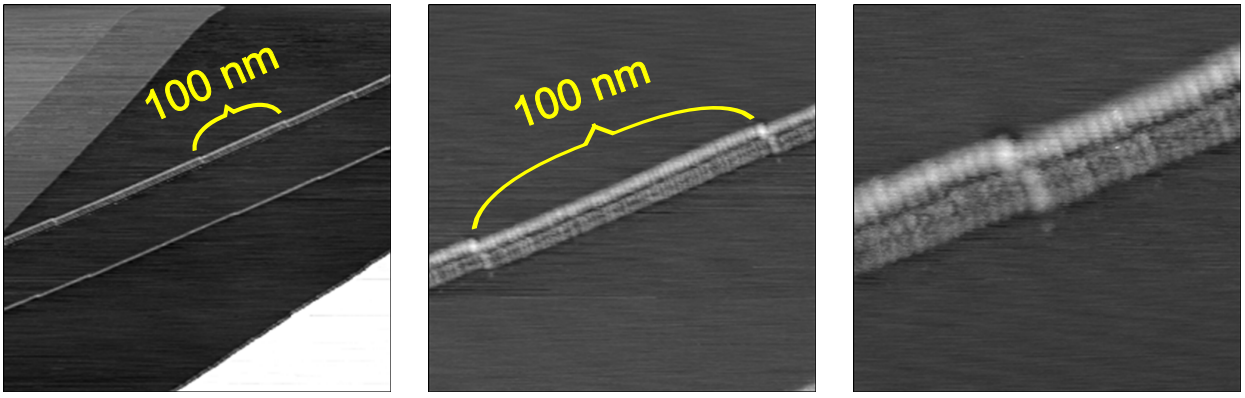

Figure B.10: STM of a periodic feature. Bright spots coincident with longitudinal zig-zags are approximately 100 nm apart. Sub-periodicity is approximately 2 nm. Left: Scan size 500 nm × 500 nm. Center: 125 nm × 125 nm. Right: 50 nm × 50 nm. (+ 0.5 V, 0.2 nA)

Adding yet further obfuscation, there is a multiple tip imaging this object. Not only is there a far-away echo of the object near the center of the left image in Figure B.10, but the smaller scan size shows that the object is shadowed by multiple image(s) of itself nearby.

Based on line sections through the brightest "strand," the object itself is likely approximately 4 nm in apparent width, with the other image(s) of the feature being multiple-tip echo(es). This is demonstrated in Figure B.11, where an alteration that was induced in the feature by the performance of spectroscopic measurements is visible not only in the location in which the spectroscopy was performed but also in the brighter view of the object above it.

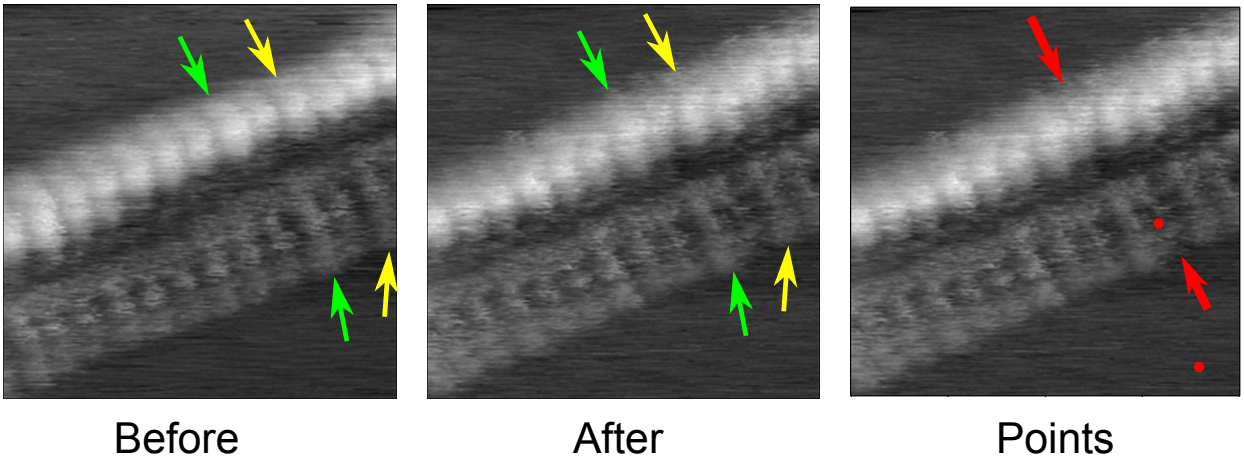

Figure B.11: STM topographs of the object before and after point spectroscopy. Indicated features in left and center scans are the same in both images, used to identify the extent of lateral drift between scans. Right: Same as center, with locations of on-object and graphite control spectroscopy marked by dots. The newly-acquired dimming of a spot on the lower filamental shape is reflected by dimming on the upper filament, marked by arrows, indicating that the filaments are a single object. Scan sizes 20 nm × 20 nm. (- 0.5 V, - 0.2 nA)

If this object is indeed an artifact, it is one which shows similar topographic characteristics to objects often identified as pili. This serves as an enthusiastic reminder that beyond-topography measurements such as tunneling spectroscopy are key to discerning the identity of sample components.

Appendix C

Sample Preparation

A primary challenge in scanning probe microscopy measurements of biological samples is appropriate preparation of said samples such that realistic insight into the native properties of the samples is obtained. Much of the difficulty lies in ensuring the sample will be sufficiently stable on the substrate surface to obtain meaningful measurements [79]. This Chapter thus discusses in detail the sample preparation used in this study.

Sample preparation for scanning probe microscopy studies of biological samples has long been recognized as key to achieving good results [63]. It is important, particularly for STM and spectroscopy which require electrical contact between sample and voltage source, that the sample is sufficiently well-connected to the substrate. Furthermore, proper treatment of the biological sample itself is important for producing samples which are amenable to the intended experiments. The purified pili used in this research were not chemically fixed, in contrast to the conventional tradition for observing biological samples, because the preceding room-temperature study had shown that chemical fixation tended to obscure periodic features on the pili [23].

C.1 Sample Substrate Mounting

Graphite was chosen as a substrate for the samples in this study for several reasons. First, it is an electrically conductive material, and STM and spectroscopy require electrical contact

to the sample in order to deliver the bias voltage. Next, it is a mostly-renewable resource due to the now-classic mechanical exfoliation method [81], which exploits the weak bonding between the stacked graphene layers which make up graphite. Adhesive tape is applied to the top of the graphite crystal and peeled away. Several layers of graphite will prefer to adhere to the tape rather than to the main graphite crystal remaining behind, thus exposing a fresh graphite surface. This makes it a fiscally feasible substrate for experiments requiring frequent redepositions of new doses of sample, as opposed to gold, which has also historically been used for STM studies on DNA [97]. One disadvantage of graphite compared to materials such as gold is that the edges of the layered flakes of graphite on the surface can show enhanced electronic behavior [91] or curl up topographically, which results in features not dissimilar in appearance to pili, as described in Appendix B and observed by other workers [22]. Additionally, the cleaving procedure can result in fragmented particles remaining on the surface, which can find their way onto the tip. Difficulties arise either when such debris is of a size to exhibit Coulomb blockade effects in the spectroscopy [95] or when it makes the tip–sample junction distance unstable, as discussed in more detail in Appendix B. Familiarity with common graphite artifacts can go some way towards ameliorating this downside.

Samples were deposited on highly ordered pyrolitic graphite (HOPG), grade ZYA. This was mounted on stainless steel sample disks in order to deliver the bias voltage to the sample. The graphite was affixed to the stainless steel using silver paint, an adhesive with silver particles dispersed within it, to provide a continuously conductive path between the graphite and the sample disk. The crystal was centered on the disk such that the STM tip could encounter the largest possible area of the graphite. Photographs of a mounted graphite substrate are shown in Figure C.1.

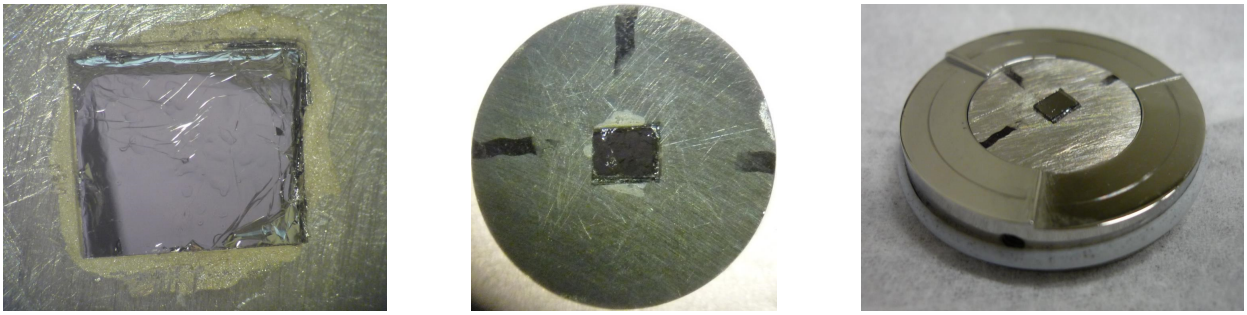

Figure C.1: HOPG mounted on a stainless steel sample disk. Left: Graphite crystal mounted on a stainless steel sample disk. The conductive adhesive used to mount the graphite on the disk can be seen extending beyond the graphite footprint. Photograph taken through an optical microscope at 20x magnification. Center: Graphite on sample disk, showing the alignment marks used to center the graphite. Right: Graphite mounted on sample disk and inserted into ramps. At this stage, the graphite sample is ready either to have pili deposited onto it or to be mounted on the STM directly.

C.2 Sample Deposition

Sanela Lampa-Pastirk from the MSU Department of Microbiology and Molecular Genetics prepared the biological sample. Pili were sheared from cultures of *G. sulfurreducens* grown, prepared, and purified by Dr. Lampa-Pastirk according to the procedure laid out in Reference [25] based on the protocol in Reference [12]. Briefly and schematically, the bacteria were grown under conditions that encouraged them to express pili, then the bacteria with their attendent pili were broken apart mechanically and via detergent, and the resulting amalgamation was separated by filtering away the other cell products through a porous gel before rinsing and drying the pili which remained. At this point, the pili were resuspended in a pH 9.5 solution to encourage deaggregation of the proteins so they would be deposited as single nanowires rather than bundles, additional contaminants were removed, and the sample was dried and frozen for storage. Before the pili were deposited for this research, they were thawed and resuspended in doubly deionized water.

For the STM and point tunneling spectroscopy experiments that were the main focus

of this work, 10 μL of pili suspended in doubly deionized water, corresponding to a density of approximately 5 mg/μL [25] were deposited using a micropipette onto a freshly-cleaved graphite surface mounted on a stainless steel sample disk that fit into the ramps in the microscope used for this study, as shown in Figure C.1. The sample was left to physisorb onto the graphite for ten minutes, then the droplet was wicked away using filter paper, and the sample was rinsed by depositing doubly deionized water of the same volume as the sample droplet. The rinsate was left to soak for five minutes and wicked away, then the rinsing process was repeated to make a total of two rinses after sample deposition. The sample was then dried under a stream of N_2 gas for approximately one hour. When the sample was not being scanned or in the process of being mounted on the microscope, it was stored in a container with a positive overpressure flow of N_2 gas to minimize its exposure to atmospheric oxygen and other contaminants. After the sample was mounted on the cryogenic-capable STM, the microscope area was pumped down to a few or a few tens of μtorr and filled with N_2 gas before cooling down to 77 K by immersion in liquid nitrogen.

C.2.1 Deposition Protocol Tuning

While the sample deposition protocol from Veazey's work [22] provided an excellent starting point, further optimization of the deposition process was warranted for the experiments discussed here. Further tuning of this protocol addressed some of the challenges faced in obtaining reproducible, conductive samples with a sufficient spatial distribution of pili to aid in timely identification of individual pili. While this protocol tuning was carried out on silicon, covered with a layer of either native oxide or 300 nm of thermally grown oxide, this was the origin of the protocol used to deposit the sample on graphite for STM.

Concerns over a possible less-conductive layer left behind on the sample after deposi-

tion stemmed from studies on pili deposited on gold electrodes formed on a silicon dioxide substrate, discussed in Appendix E. During AFM investigations of these samples, it was observed that regions of the sample appeared to be blanketed with a relatively soft and relatively non-conductive substance, unlike the bare gold that was expected. Two hypotheses for the identity of this layer were that portions of the gold were nonconducting due to a contaminant film on the surface or that the film itself was composed of pili matted together. This concern was probed in part by varying the amount and type of rinsing and drying of the samples after deposition, in case contaminants from the air had found their way into the water in which the pili were suspended during the time allotted for deposition. Figure C.2 shows a few of the scans which seemed to indicate the presence of what is perhaps a dense, near-monolayer mat of pili with trapped fluid in the interstices.

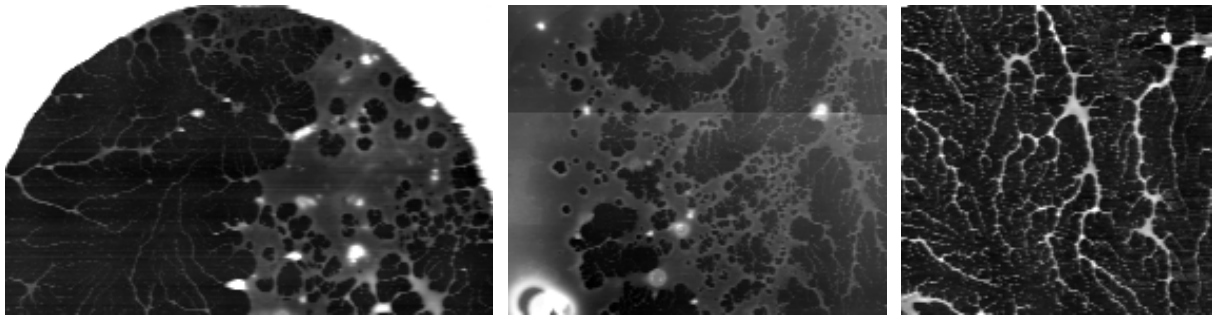

Figure C.2: AFM topographs of pili on SiO_2. Left: Pili on a circular area of SiO_2 surrounded by gold. The pili on the left of the circle follow tree-like branching patterns of bundling. The pili on the right of the circle have perhaps trapped fluid between the filaments, resulting in a "frayed blanket" look. Center: Another "frayed blanket" pilus formation. Right: Typical "neuron" structure of pilus bundles on SiO_2. All scans are 5.7 μm in the vertical direction. Left scan width 9 μm, z grayscale 40 nm; center scan width 7 μm, z grayscale 40 nm; right scan width 5.7 μm, z grayscale 15 nm.

The other primary concern in obtaining a satisfactory sample deposition protocol was optimizing the density of pili on the sample. Ideally, pili would be spread uniformly around the surface and easily found with the scanning probes without being more than a monolayer

thick; however, the density and distribution when the sample was deposited on graphite were such that this was not the case. In order to shed light on whether an insufficient number of pili were making it to the surface from the droplet in which they had been suspended, a series of deposition durations was investigated. Pili were suspended in a droplet of water or of buffer, then deposited on a clean silicon chip and left for a range of times before the droplet was wicked away using filter paper, after which the samples were either rinsed or not, with the rinsate wicked dry using the same method. The resulting samples were then imaged using amplitude modulation atomic force microscopy.

In the initial test of different deposition conditions, the pili samples were deposited onto silicon chips on which the silicon was either covered with the few-nanometer native oxide layer or with a thermally-grown SiO_2 layer 300 nm thick. Each of these was cleaned either according to a standard cleaning protocol similar to that given in Appendix E or using the "RCA 1" cleaning protocol for more stringent chip cleaning [98]. On these four different substrate preparations, then, was deposited a sample of pili suspended either in doubly deionized water or in CHES buffer to maintain a pH of 9.5. Using doubly deionized water would provide the benefit of not needing to consider possible artifactual effects in measurements due to the presence of buffer salts; using buffer to maintain a stable pH of 9.5 would provide the benefit of deaggregating the pili [25] to make individual nanowires more accessible for measurement. The amount of time the sample droplet remained on the surface was also varied in an endeavor to determine whether there would be a denser coverage of pili, or a larger amount of surface contamination from the droplet, when the droplet was left on the sample longer. Each sample was sealed using Parafilm (stretchable, wax-covered film) into a plastic petri dish in company with a piece of lens-cleaning tissue soaked with water to maintain the humid environment so the sample droplet would not evaporate. After the

allotted amount of time—30 minutes, 2 hours, 6 hours, or 12 hours—the droplet was wicked dry and, in the case of sample deposited from pH 9.5 buffer, rinsed with doubly deionized water, before AFM imaging. The predominant impression from this investigation was that, whether rinsed or not, and not strongly dependent on deposition duration, the buffered solution was prone to leaving residue on the surface, as seen in Figure C.3. Consequently, deposition from a suspension of pili in doubly deionized water was preferable. Note that the buffer used in previous STM work on *Geobacter* [22, 23] was a different type, PBS, intended to stabilize the pH around that of water, and thus this observation of buffer residue does not reflect unfavorably on the conditions in that work. Note also that the residue in the samples deposited from CHES buffer was localized; some portions of the sample appeared as expected for the substrate. No pilus candidates were seen on these samples.

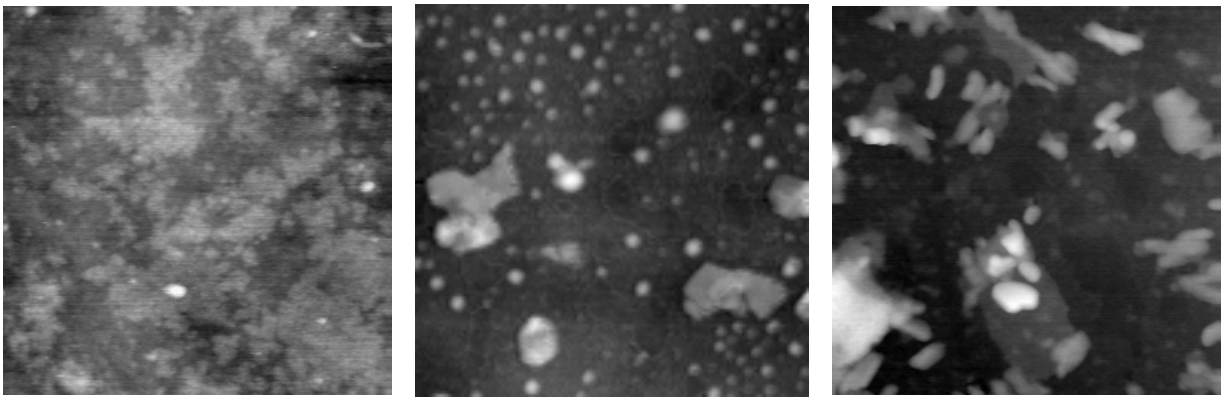

Figure C.3: AFM topography scans from the deposition duration investigation, selected to highlight features from buffer residue. All samples shown here were deposited from CHES buffer (pH 9.5). Left: 30 minute deposition time, rinsed, RCA 1 chip pre-cleaning. Center: 2 hour deposition time, solvent chip pre-cleaning. Right: 12 hour deposition time, rinsed, RCA 1 chip pre-cleaning. All image sizes are 1 μm $\times$ 1 μm. Left z grayscale 6 nm, center z grayscale 20 nm, right z grayscale 34 nm. Lozenge-shaped features are not bacteria, which would be much larger and which were removed by the purification protocol.

Next, the deposition condition evaluation was repeated for only the 2 hour deposition duration to reduce the number of variables. The pili, suspended in either doubly deion-

ized water or CHES buffer at pH 9.5, were deposited on silicon chips with either a native or thick oxide layer, cleaned either using a standard solvent cleaning procedure or using the RCA 1 process. Several of these preparations resulted in pili on the surface which were imageable by AFM; a few scans of the most thoroughly piliated sample from this evaluation are shown in Figures C.4 and C.5. Networks of pili, superficially similar in appearance to neural networks, were frequently seen, and intersections between pili in these networks resulted in nodules larger than the sum of the pili sizes in the intersection. These nodules are perhaps due to additional material, such as buffer salts or water, being trapped between the overlapping pili. Furthermore, AFM phase imaging, which is sensitive to differences in sample adhesion or softness as discussed in Appendix D, showed the presence of a film-like material between the pili in these networks, as can be seen in Figure C.5.

The difference in distribution of pili on silicon dioxide compared to that on the graphite surface used for the primary research project discussed here could potentially be attributed to the hydrophobicity of graphite versus the hydrophilicity of the oxide-covered silicon—even the nanometer-scale native oxide layer is sufficient to make silicon chips hydrophilic [98]—and the consequent interaction with the droplet. While the hydrophilicity of the silicon dioxide surface made it better suited for adsorption of proteins in general [79] than the graphite surface, its lack of metallic conductivity made it unsuited for the STM-based experiments discussed here. The silicon dioxide substrate would introduce complications to the interpretation of spectroscopic data and have a deleterious effect even on the acquisition of topographic images. The deposition conditions chosen for the primary research were aimed to be as near *in vivo* pH as possible without adding buffer. Since individual pili were successfully imaged on the graphite surface when deposited from doubly deionized water, although not in the neural network configuration seen above, sample deposition was always

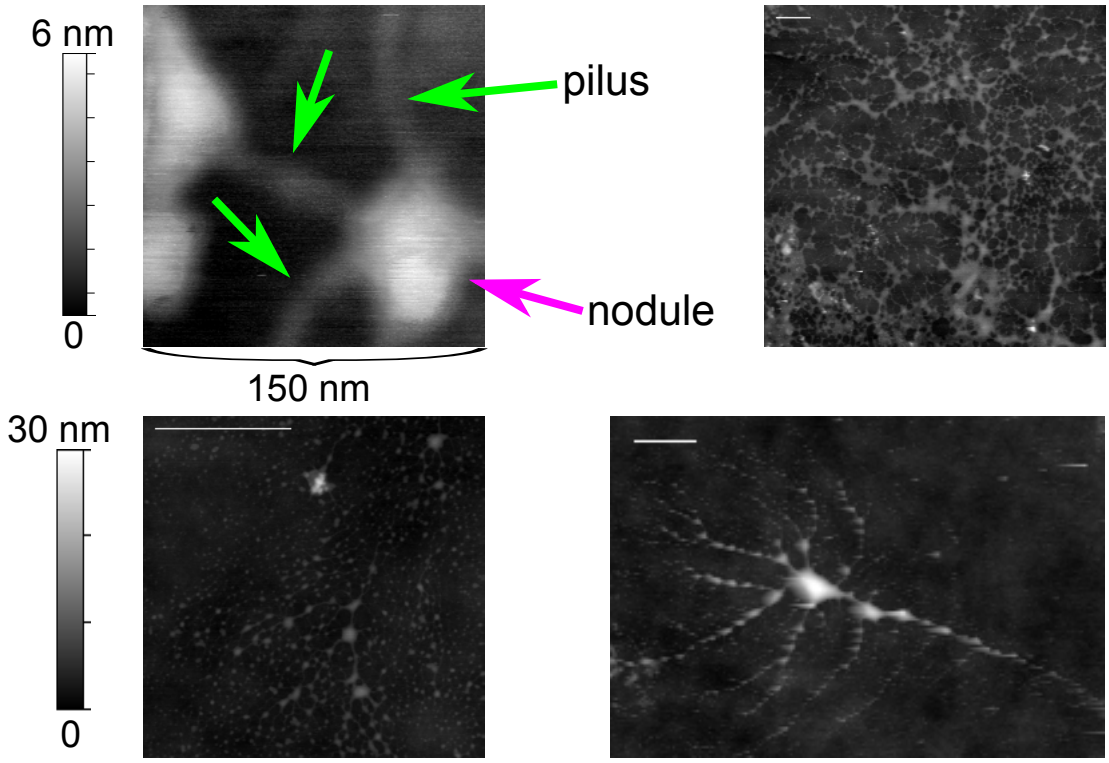

Figure C.4: Highlights from a deposition test conducted with the droplet of pili in pH 9.5 CHES buffer remaining on the thermally oxidized silicon surface for 2 hours, then rinsed twice with doubly deionized water. Upper Left: Focus on several individual pili interacting at a nodule. Scan size is 150 nm × 150 nm. Upper Right and Bottom Row: Pilus network topography examples from other locations on the same sample. Scale bars are 1 μm. The z height shading scale is the same for all of these AFM images except the upper left scan.

from water. Additionally, it was found that a deposition time of 10 minutes was sufficient to permit pili to be deposited with tolerable density on the graphite surface, and the rinsing time was increased to 5 minutes for each of the two rinses. Thus, despite differences between the surfaces, the deposition condition study on the silicon dioxide substrate provided a viable sample deposition protocol for experiments with pili on graphite.

As a final caveat regarding sample preparation, Figure C.6 shows an AFM topograph of a cell found on an electrode sample discussed in Appendix E. This sample was obtained from purified pili [12], so this is not a *G. sulfurreducens* cell. The question remains open as to from where this cell originated. Possible sources include pre-deposition contamination of the

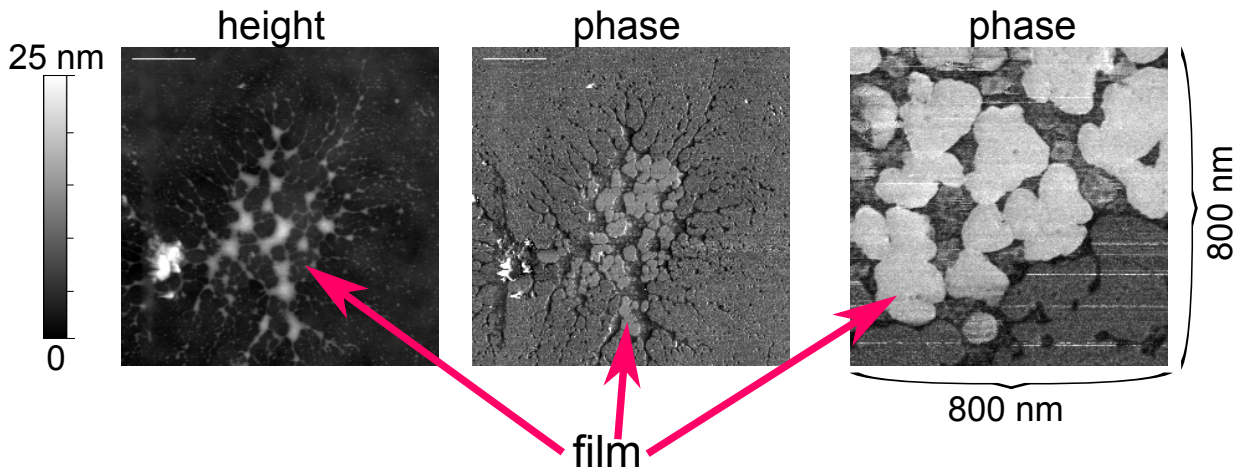

Figure C.5: Scans showing "film" between pili, from the same deposition test as Figure C.4. Left and Center: Height and phase images on the same feature area. Scale bars are 1 μm. Right: Phase image of an 800 nm $\times$ 800 nm portion of the "neural network" shown at left.

substrate, pre-deposition contamination of the water used to suspend and rinse the pili, or contamination of the sample during the deposition process. The mats of pili radiating from what appears to be a flagellum imply that the cell and its flagellum were in place either before or at the same time as the pili were deposited. If the cell had encountered the pili mats after the sample was dried, it seems slightly unlikely that it would have "stirred" the pili into such a configuration. Figure C.7 shows a smaller scan range view of this. Since this was the only cell observed during the course of this research, it can be considered an exotic contaminant. While the cell in Figures C.6 and C.7 is almost certainly *not* a *G. sulfurreducens* bacterium, it is useful to include for perspective on the relative sizes of the *Geobacter* pili of interest compared to more-familiar objects such as cells and flagella. This cell of unknown origin is of a typical size for a bacterial cell—approximately 1 μm long, 0.5 μm wide, and 0.1 μm tall. The flagellum is approximately 5 μm long, 0.1 μm wide and 30 nm tall—an order of magnitude taller than *Geobacter* pili.

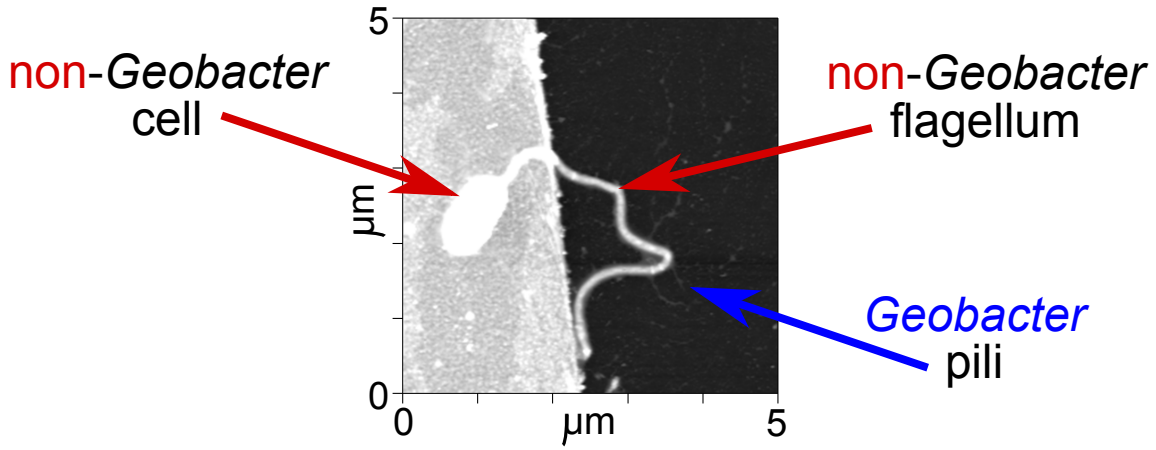

Figure C.6: Unexpected cell observed on a sample using AFM. The lower substrate surface is SiO_2, and the upper surface is a 25 nm-tall evaporated gold electrode.

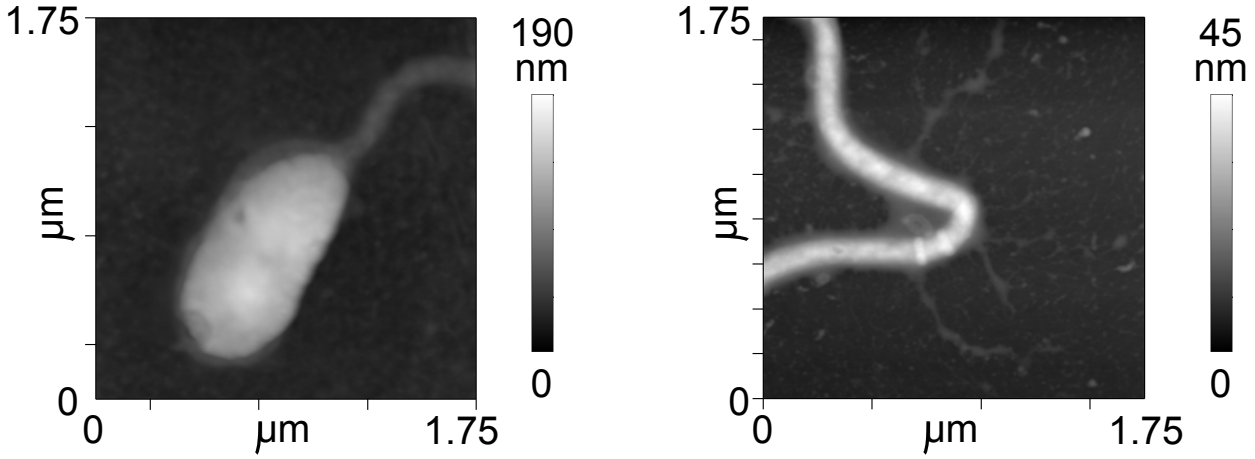

Figure C.7: Unexpected cell observed on a sample using AFM, seen in its entirety in Figure C.6. Left: Cell and flagellum on gold. Right: Flagellum on SiO_2 with *G. sulfurreducens* pili forming mats in response to it.

C.2.2 Spatial Density of Deposited Pili

Because of the uncertainty as to how conductive the pili would be at low temperature, thus how well they would be identifiably imaged by STM, a simple statistical argument was made to tie the observed density of pili on the sample scanned at room temperature to the predicted density of pili on the sample when scanning at low temperature. One significant assumption in this estimate was that the pili were uniformly distributed on the surface.

Since this was generally observed not to be the case, this estimate merely provided a rule of thumb for whether candidate features seen at low temperature were likely to be pili, even if the spectroscopy proved to be unstable.

In the systematic search for pili, it was convenient to define "regions" of the sample surface which were scanned in a uniform fashion in order to facilitate comparison. Since multi-micron–scale lateral (XY) sample translation was based on the stick–slip method, as discussed in Chapter 3, the regions were generally non-overlapping. It is a fair statement that the regions are independent samplings of a several mm^2 surface. The pili are only a few nanometers in diameter, so a multi-micron scan size divided into 128 pixels would limit the apparent pilus size to smaller than one pixel. In order to facilitate visual identification of pili, the regions were divided into individual scans smaller than 1 μm $\times$ 1 μm in area, as shown by the nine boxes comprising the region in Figure C.8. To ensure systematic coverage of the entire region and to avoid inadvertent redundant scans, a specific search pattern was followed of offsets moving to new scan areas within each region, as shown in the same figure.

In the initial room temperature data run, two pilus candidates appeared in the first six scanned regions, with one "region" systematically defined as in Figure C.8. Using the estimated scan area size decrease by a factor of 9 at 77 K as compared to its room temperature area, decreasing by a factor of three in both lateral directions due to thermal effects on the piezotubes as described in Chapter 3, the number of pilus candidates seen in a given number of regions should decrease correspondingly by a factor of 9. This was found to be approximately the case in the first low-temperature data run, as two pilus candidates were seen in 43 regions. Comparing the number of regions needed to see two candidates, $\frac{6}{43} \approx 0.14$. This has a $\sim$20% discrepancy with $\frac{1}{9} \approx 0.11$, which is not unexpected given the small statistics for the purposes of this calculation. This lent further credence to the

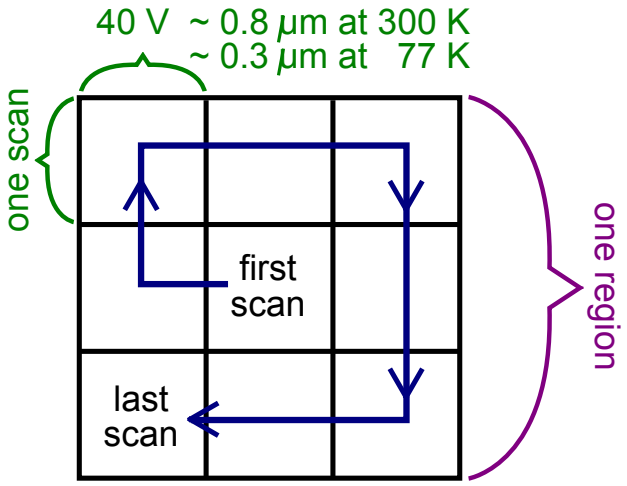

Figure C.8: Schematic of the search pattern typically followed within a particular "region." Each individual scan area of the nine scan areas comprising the region was 40 V × 40 V in size, where this voltage is the voltage applied to the scanning piezotube's quadrants. At room temperature, each scan area was approximately 0.8 μm × 0.8 μm, while at 77 K, the same applied voltages resulted in a scan area of approximately 0.3 μm × 0.3 μm, to one significant figure. Each of the nine boxes within the region is a complete scan.

determination that the candidate objects seen at 77 K were indeed pili. Later, spectroscopy was successfully obtained on objects with similiar topography, identifying them as pili.

C.2.3 Reproducibility of Deposited Samples

While substantial efforts were made to ensure that all samples were identical, some sample depositions did appear to have more pilus candidates than others. In part, this could have been due to the low statistics—if only a handful of individual pilus candidates were expected for each sample, based on the rough calculation above, a quantity difference of only a few pilus candidates between different samples could appear to be substantial while actually being a normal amount of scatter between samples.

For some sample depositions, the deposited droplet would "wet" the surface of the graphite differently. Wetting of a surface, or the amount a droplet spreads when deposited onto the surface, depends on the polarity of the surface and of the fluid. Water deposited on

hydrophobic surfaces forms droplets with minimal droplet area in contact with the surface. The graphite surface is hydrophobic, in contrast to another cleavable substrate, mica [99], which is also often used in scanning probe microscopy experiments. To cause a difference in the wetting of the sample surface, either something on the surface was modifying the hydrophobicity of the graphite, or something in the sample droplet was modifying the polar character of the water. In general, the graphite sample was cleaved immediately prior to deposition. In a few cases, the graphite was cleaved, proper graphite spectroscopy was verified using the STM, then the sample was deposited. In each case, since a water layer rapidly forms on graphite exposed to air, a thin layer of water was present on the graphite surface before sample deposition, potentially with associated contaminants. Since the sample droplet was exposed to air, albeit in a covered Petri dish, contaminants could also have entered the water of the sample droplet, although this would not be responsible for a difference in wetting at the moment of deposition. Despite this, the potential contaminants did not prevent acquisition of correct control spectroscopy on graphite during the experiments.

Some variation among samples could occur because the pili were suspended in the water, not dissolved, and pili had a tendency to aggregate. Since often only a few microliters of sample were deposited from the often several μL total volume of water in which the pili were suspended, the density of pili in the selected droplet could vary. It can be considered, however, that the anisotropic distribution of the pili on the surface played a greater role in the difficulty of finding individual pili to study. The droplet size was deliberately chosen not to cover the entire graphite surface; when water spills over the edges of a graphite slab, it could intercalate between the layers that comprise the graphite, loosening the connection between layers and, consequently, encouraging instabilities. In addition, edges and corners of the graphite slabs tend to possess flakes and outcroppings which can be quite hazardous

to STM tips, so the outer edges of the graphite slab were experimentally unusable. This means that the pili-containing droplet was confined to the center area of the graphite; even so, the graphite area was at least slightly larger than the droplet. After the droplet had been repeatedly rinsed and wicked dry, a sample without significant contamination was invisible by eye, thus positioning the STM tip in a specific location with respect to where the droplet had been could be a minor challenge. Making matters even trickier, once the sample was inside the cryogenic STM, it was no longer optically visible, and sample motion choices were based on a mental model of the overall structure of the sample. Considering that the droplet size was on the order of a millimeter in diameter and the largest scan size in which pili could be comfortably identified at room temperature under the scanning conditions used here was on the order of one square micron, starting in the "wrong" place on the sample for finding pili could lead to substantial amounts of time spent imaging graphite untouched by the sample droplet. For this reason, an apparent differing number of pilus candidates per scan time among samples, as in the $\sim$20% difference between room temperature and 77 K pilus densities discussed above, could also be impacted by the amount of time spent searching for pili on bare graphite where the sample had not been deposited, and hence should not be taken as an indicator of significant differences between samples.

C.2.4 Contact Between Pili and Substrate

STM imaging and stable spectroscopy rely on a consistent delivery of bias voltage to the sample. In some cases, it appeared as though the tip was moving the sample around on the substrate and, consequently, imaging it poorly, as in Figure C.9. In other cases, segments of the pili would appear and disappear between scans, which was attributed to the tip having perturbed the pilus out of contact with the surface. Additionally, in Figure C.10, it appears

as though the influence of the tip has caused part of the pilus to move back and forth along the surface. In particular, it appears as though the pilus shown in the left and center images in Figure C.10 is being moved by the tip. The retrace scan was obtained as the tip moved backwards into position to begin scanning the next line of the trace scan. It appears that the lower part of the vertically-oriented filament is in poor contact with the surface, as it is being imaged sporadically. The scan on the right shows the vertical tendril being imaged more stably after it appears to have been wrenched from the upper part of the pilus.

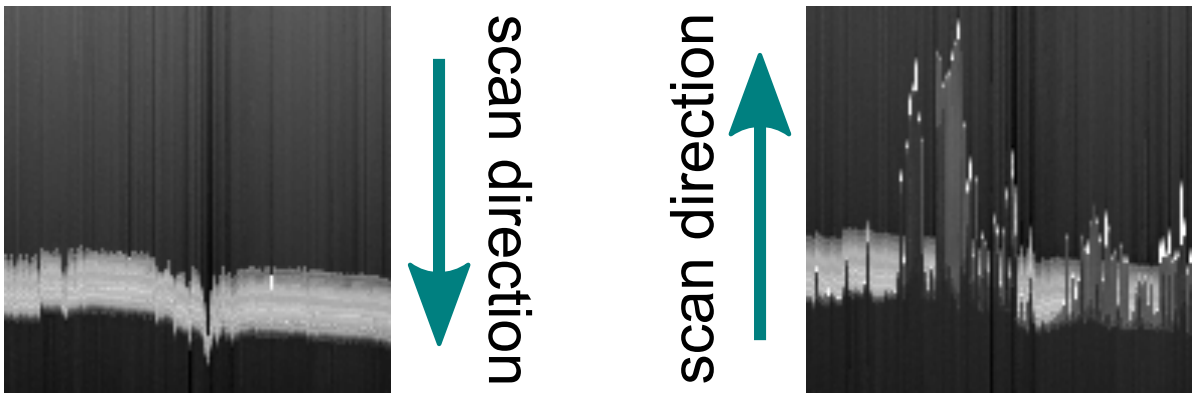

Figure C.9: A single STM topography scan. The tip moved down and then up along the same line of the image before proceeding to the next line. Tip-induced sample motion can be seen most clearly in the center of the scan, where nanowire is perturbed in the direction of scanning. Scan size is 763 nm vertically and 749 nm horizontally. The apparent breadth of the nanowire is likely due to a combination of the convolution of the nanowire topography with the tip's radius of curvature, ambiguous resolution of the edges of the nanowire, and motion of the nanowire along the scan direction. (+ 0.75 V, 0.2 nA)

In many cases, the most stable spectroscopy was on pili which were "anchored down" by a graphite flake, as though part of the pilus had become lodged under the flake's edge during deposition. These pili could be stably scanned for many hours repeatedly without degradation, showing that STM imaging under normal conditions did not discernibly alter the sample. Pili which protruded from aggregate bundles, as in Figure C.11, also seemed to be anchored down by the other pili in the bundle. These anchored-down pili did not show

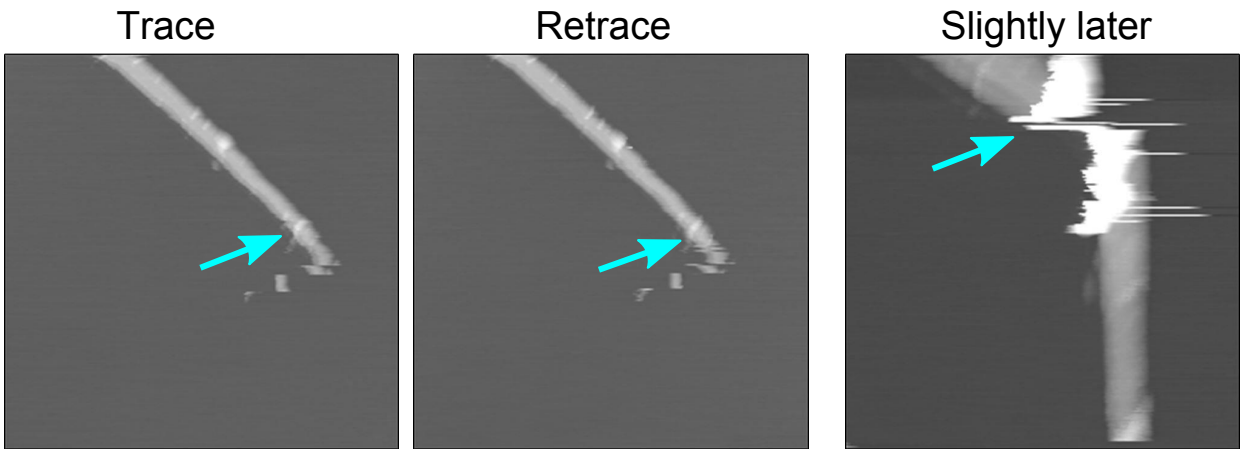

Figure C.10: STM scans of one filament. Arrows indicate a feature useful as a landmark. An unstably imaged tendril is visible below the arrow. Left: Scan of a pilus unstably affixed to the surface. Center: Near-simultaneous scan but with the tip moving in the opposite direction. Right: Smaller-scale scan. Left and center scans are 400 nm × 400 nm; right scan is 100 nm × 100 nm. (+ 0.5 V, 0.2 nA)

the sporadic imaging problem shown in Figures C.9 and C.10 and thus were good candidates for tunneling spectroscopic measurements.

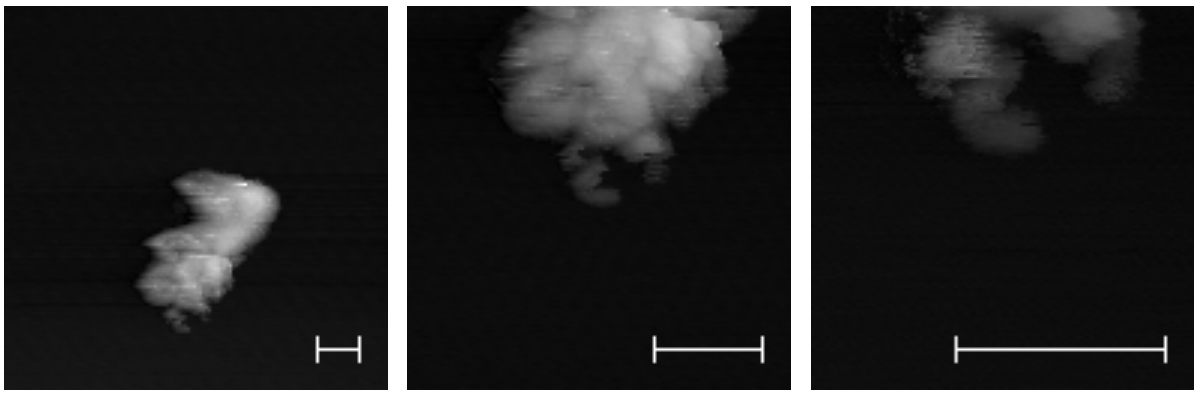

Figure C.11: Series of STM scans zooming in on the croissant-shaped mandibles—two individual pili—protruding from an aggregate bundle of pili. Pili found near bundles or graphite flakes were generally stable on the surface over hours of scanning, perhaps because of being anchored to the surface by the larger objects. Scale bars 20 nm. (+ 0.5 V, 0.1 nA)

Once a (relatively-)stable pilus was found on the graphite substrate, STM topography and point tunneling spectroscopy could be obtained.

Appendix D

Further Details

While the discussions and explanations in the main text can generally stand alone, this Appendix probes a little deeper into some of the details of the techniques and ideas relevant to this research. Particular emphasis is given to further discussion of the scanning probe microscopy techniques and apparatus presented in Chapters 2 and 3.

D.1 Feedback

For the scanning probe microscopy modes used in this study, the tip–sample separation is adjusted dynamically during scanning to reflect changes in the sample topography, convolved with the sample's density of states in the case of STM. The feedback signal for amplitude modulation AFM is the amplitude of the cantilever's oscillation, but otherwise, the feedback behaves as it does for STM, where the feedback signal is the tunneling current, so only STM feedback will be discussed here for simplicity.

In this feedback system, the signal of interest is the tunneling current detected by the electronics. This detected tunneling current is compared to a user-defined current "setpoint" value. If the detected current differs from this, the tip–sample separation is increased or decreased until the detected current matches the setpoint value. This is "negative feedback," in that it acts to minimize the difference between the actual and setpoint values. As the tip is scanned along a surface, it encounters variability in the surface topography or local

density of states of the sample. This causes the tunneling current to change, which requires intervention by the feedback system. Parameters affecting the response time of the feedback loop can be adjusted by the equipment operator. Both the gain and the time constant of the feedback loop can be adjusted, and their effects are not independent. In a simple picture, the time constant can be thought of as describing the reaction time of the feedback loop, and the gain can be thought of as the enthusiasm of response of the feedback loop. Consider the case of the STM electronics detecting a too-large tunneling current signal as mapped onto the case of little Miss Muffet seeing a spider sitting down beside her. The time constant of the spider-proximity feedback loop would then describe how quickly she was frightened away, and the gain would be the extremity of her fright impelling her to vacate the premises.

D.2 Piezoelectric Rastering

In order to raster the scanning probe over a sufficiently precise area in a well-controlled manner, either the tip or the sample has its motion governed by piezoelectric elements. Piezoelectric materials expand or contract slightly in response to applied voltages, so a tip or sample supported by piezoelectric elements with the expansion directions appropriately oriented can be moved in a controlled, nanoscale manner by applied electronic signals.

The piezoelectric elements in the cryogenic-capable STM used for this research are tube-shaped, hence their appelation "piezotubes." These thin, hollow cylinders of the piezoelectric ceramic material PZT—lead zirconate titanate, a mixture predominantly composed of $PbZrO_3$ and $PbTiO_3$ [30]—have metallic contacts applied to them to which wires are soldered which carry the voltages from the STM controller. There are four electrical contacts on the outside of the piezotube and an interior metallization providing the ground for the volt-

age applied across each quadrant. When a particular voltage is applied to one quadrant, the piezoelectric dipoles align such that the material of that quadrant contracts. When a voltage of the same magnitude and opposite polarity is applied to the quadrant opposite that one across the diameter of the piezotube, that opposite quadrant expands by the same amount. Thus the entire tube bends like an elephant's trunk. For small enough amplitudes of the bending compared to the diameter of the piezotube, this can be considered as a longitudinal translation of the top part of the piezotube, as schematically sketched in Figure 3.2.

Because of hysteresis in the piezoelectric material, the piezoelectric elements take a non-negligible amount of time to reach the elongation or contraction appropriate to the voltage applied to them. This is colloquially known as "piezo creep" and causes image artifacts such as apparent bending of straight features near the beginning of a scan, caused by the piezoelectric elements not yet reaching their full response to the applied voltage when the probe begins scanning; an example of this is shown in Figure D.1. This can be ameliorated by rescanning the region, sometimes repeatedly, to allow the piezoelectric elements to reach their full elongation or contraction before the production scan is acquired. Consequently, the first few lines of a scan may often be justifiably disregarded.

D.3 Image Processing

While raw scanning probe microscopy data can often be used to view the sample properties of interest, interpretation of same generally requires a certain amount of image processing as part of the analysis. This is not generally a case of "making it look prettier," but rather of "making it more intelligible," as artifacts and background effects can mislead both the experimenter and the experimenter's data extraction routine. The most basic and most

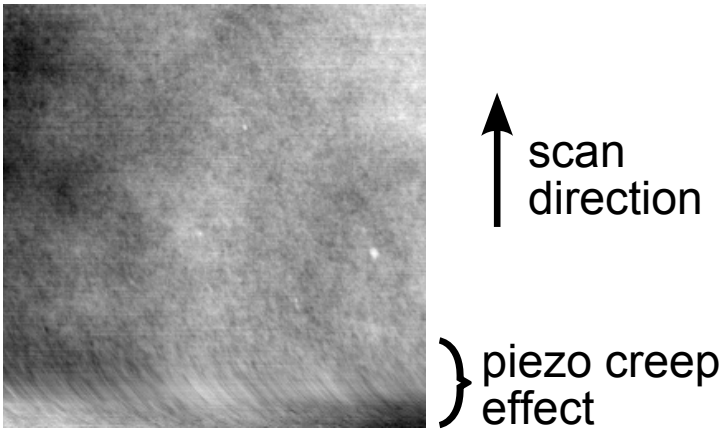

Figure D.1: Example of "piezo creep." Scan began from bottom of image and proceeded upward. The apparent bending of the image near the start of the scan is due to a delay in the full response of the scanning piezotube to the voltage applied to it. This scan of a silicon dioxide surface was obtained using a Dimension 3100 AFM with Nanoscope IIIa controller. Scan area is 1 μm $\times$ 1 μm.

harmless image processing techniques will be discussed here; many of the scans included in this thesis have had one or more of these processing techniques used on them. When measuring feature heights and breadths on a sample, it is particularly useful to process the data, as background properties of the sample could swamp the small dimensions of the features. Sometimes, it is sufficient simply to optimize the colorscale in which the scan is displayed, as in Figure D.2; default display settings may not be appropriate for the scan currently under consideration.

Most samples are tilted at an angle to the tip, as can be seen in Figure D.2. This is unsurprising, considering that achieving a sample which is flat to within less than a nanometer in height over a square micrometer or so of area when the sample is loaded macroscopically is an occurrence of some statistical unlikeliness. In order to correct for this near-omnipresent tilt, a background plane can be subtracted from the data. This can be quite important when measuring heights, as the background tilt can change the apparent heights considerably. After the plane subtraction, the line section across the graphite step

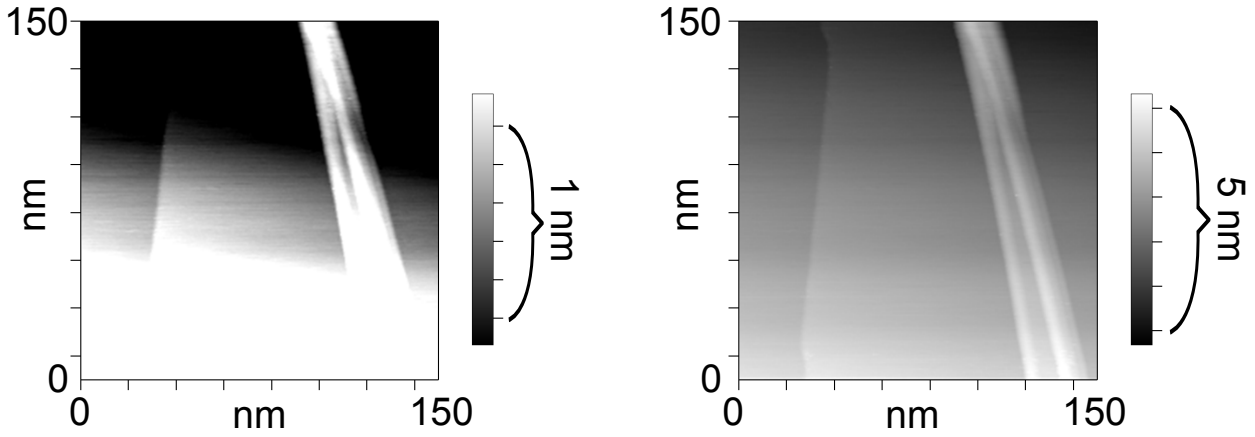

Figure D.2: Changing the colorscale used to display the data. Left: Raw image, as displayed by the Asylum Research data acquisition software. Right: After "auto" color range and offset applied. Both images show an overall tilt whereby the lower left of the image appears higher than the upper right of the image. (+ 0.5 V, 0.2 nA)

in Figure D.3 looks much more flat and step-like, providing a better baseline from which to measure the height of the filamental object.

Separately, or in tandem with a plane subtraction, line-by-line background subtractions can be made. This accounts for small variations in the tip–sample separation as a function of which "line" is being scanned at the time. Line offset subtractions are done by finding the average height of all the data in a scan line along the fast scan direction and subtracting that average value from all the data on that line; this is repeated for each line of the data. As a mental model for this terminology, consider a manual typewriter. The fast scan direction is the direction in which the typist is typing, and the slow scan direction is along the length of the page, slowly incremented by carriage returns. For example, the faint dark "bands" in Figure D.3 can be diminished by subtracting the average offset of each line, as is shown in Figure D.4. Caution should be used when choosing to apply this processing step to scans with features which align along the fast scan axis, as their heights with respect to the rest of the image would then be falsely subtracted away to match the rest of the image.

If features on the surface are significantly different from the background and including

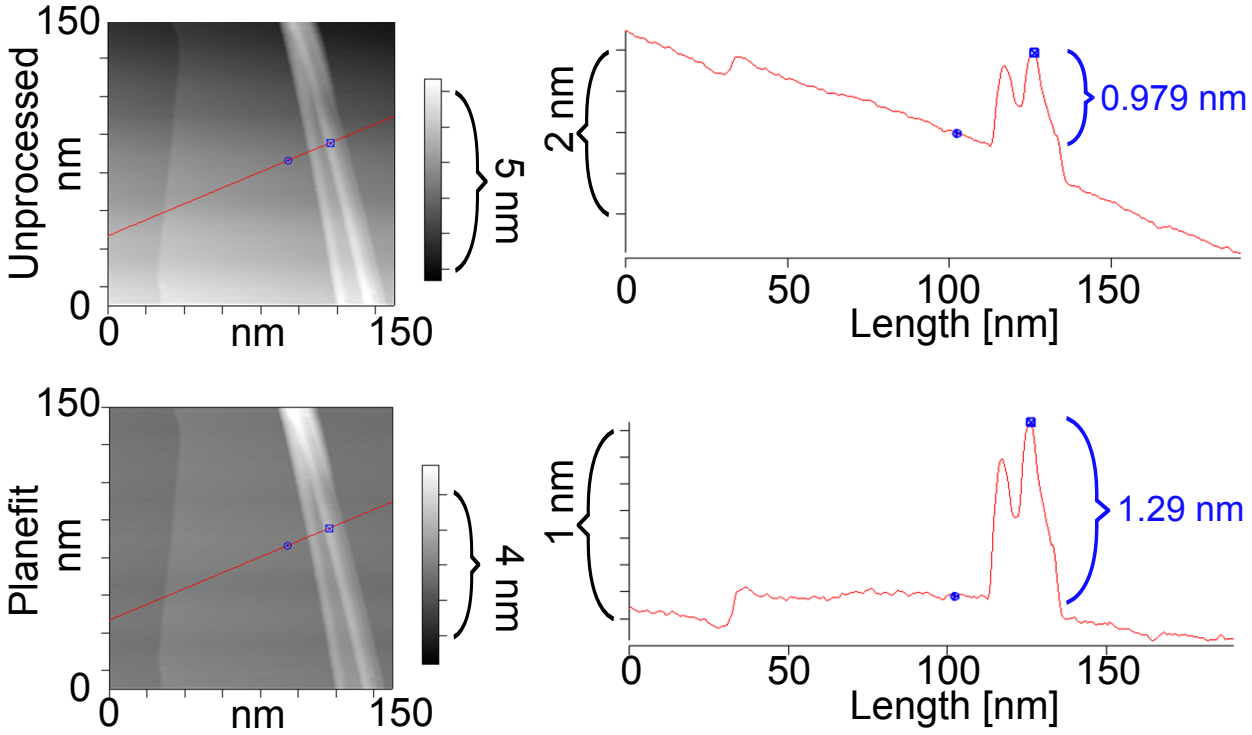

Figure D.3: Subtracting a background plane from the data. Top: Colorscaled data as seen in Figure D.2. Bottom: Data after a first-order plane subtraction was applied in the XY direction. Right: Line sections through the images on the left. The apparent height interval between the blue markers changes significantly with processing. (+ 0.5 V, 0.2 nA)

them in the processing fits would cause further artifacts, they can be "masked" away such that the processing does not include the properties of that region. This is generally not necessary for small objects such as the pili discussed here, although it was sometimes necessary when the pili were at unusual angles to the scan direction, which affected the ability to perform line offset subtraction. As an example of an image that benefited from masking during image processing, Figures C.6 and C.7, which displayed a large cellular contaminant on the surface, required masking in order to avoid including the large height of the cell in the background subtraction.

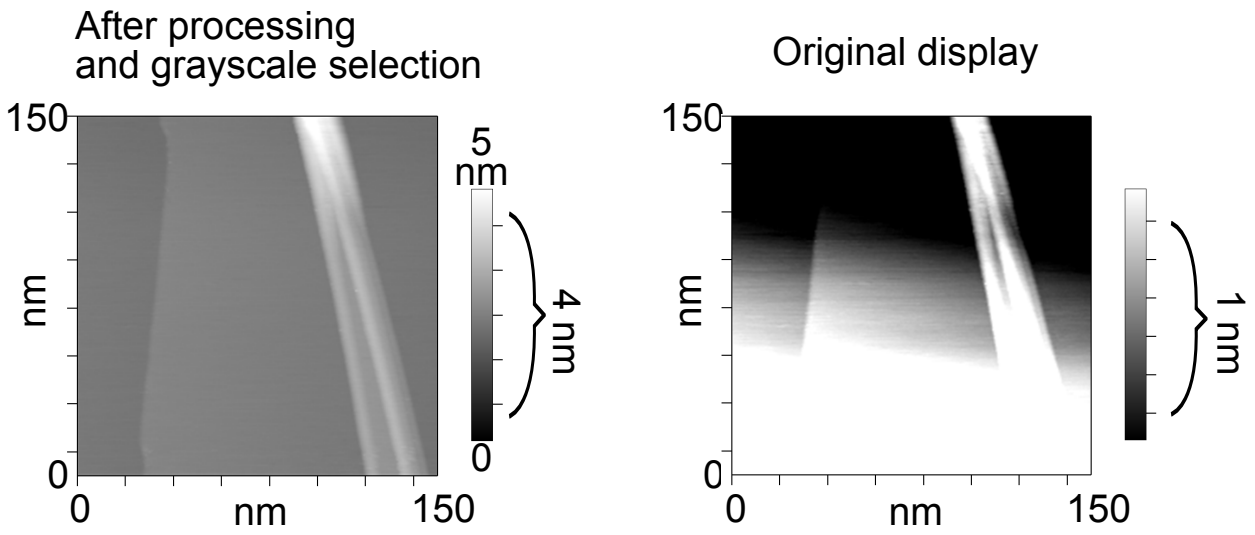

Figure D.4: Applying an offset along the X direction to the data from Figure D.3. Left: Image after subtracting a plane in the XY direction, subtracting the average offset of each line in the slow scan direction, and choosing the range and offset for the grayscale to match that in the processed image in Figure D.3. Right: Data as originally displayed in Figure D.2. Image processing done in Igor Pro using the Asylum Research software. (+ 0.5 V, 0.2 nA)

D.4 Direct and Numerical dI/dV Determination

Two ways to obtain dI/dV spectra are prevalent in the field. The first, used in this study, is to obtain I–V curves and differentiate them numerically. The second is to obtain dI/dV curves directly by means of a lock-in amplifier. When using the lock-in method, a small modulation is applied to the bias voltage with a frequency much faster than the voltage sweep, which causes the current to change correspondingly, yielding $\Delta I/\Delta V$ at each voltage step. This can give better resolution than the numerical differentiation method, yet it is also susceptible to simultaneous inadvertent measurements of other properties of the system, which can sometimes lead to differing results between the direct and numerical dI/dV curves. Since I–V curves are a more fundamental measure of the sample properties than are dI/dV curves obtained via the lock-in amplifier, in case of discrepancy, the I–V curves should be hewn to and numerically differentiated, as was done in this work.

Because of inherent scatter in I–V curve points, differentiation without smoothing beforehand resulted in noisy numerical dI/dV curves, as the differentiation interpreted transitions between scattered points as small steps of steep slope. This can be seen in Figure D.5, where the numerically-differentiated dI/dV looks impenetrably noisy. The averaged I–V data were imported into Igor Pro software and smoothed with a 2nd order Savitzky–Golay filter [100] using a 47-point window. This was found to be a good compromise level of smoothing, avoiding histrionics in the differentiation while not smoothing over meaningful features in the spectra. Additionally, the frequent flattening-out of I–V curves near the end of the bias sweeps led to sudden drops in the derivatives near the endpoints of the voltage sweeps. In general, the numerical dI/dV presented here have their displayed abscissas pruned to avoid this; most voltage sweeps in this work were from + 0.5 V to - 0.5 V. The benefit of this can be seen in Figure D.6, removing the confusing domination of these endpoint effects over the more physically interesting and relevant features in the spectra at voltages nearer zero bias.

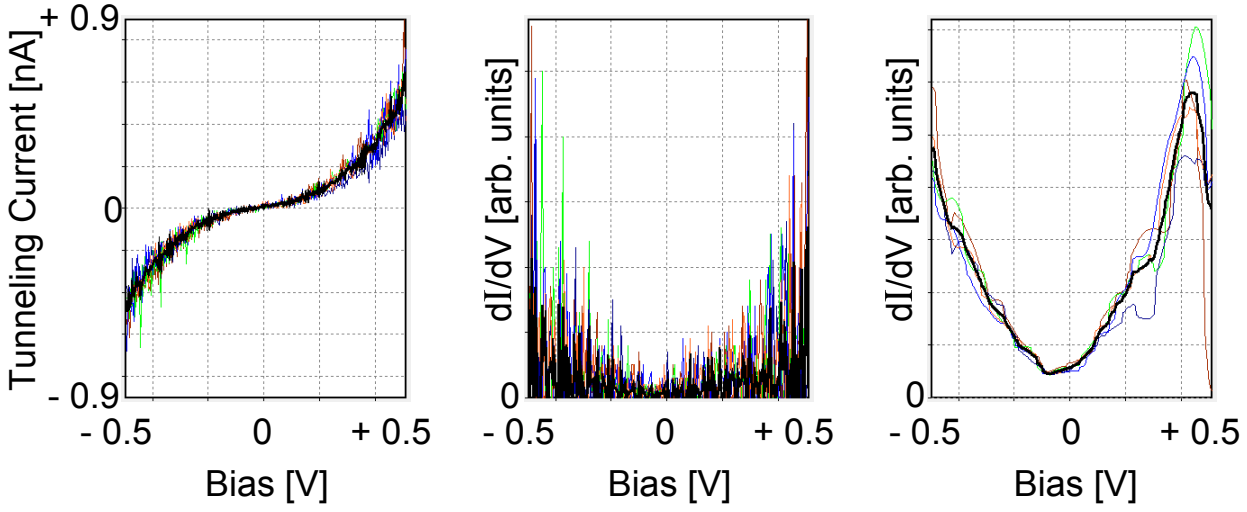

Figure D.5: Five immediately-sequential voltage sweeps above graphite. Black curves are averages of these curves. Left: I–V curves. Center: Minimally smoothed numerical derivatives calculated by the RHK data acquisition software. $dI/dV = 0$ is the bottom of the plot; parts of these curves also extend, unphysically, below that level. Noise dominates this plot. Right: Direct dI/dV via the lock-in technique. $dI/dV = 0$ is the bottom of the plot.

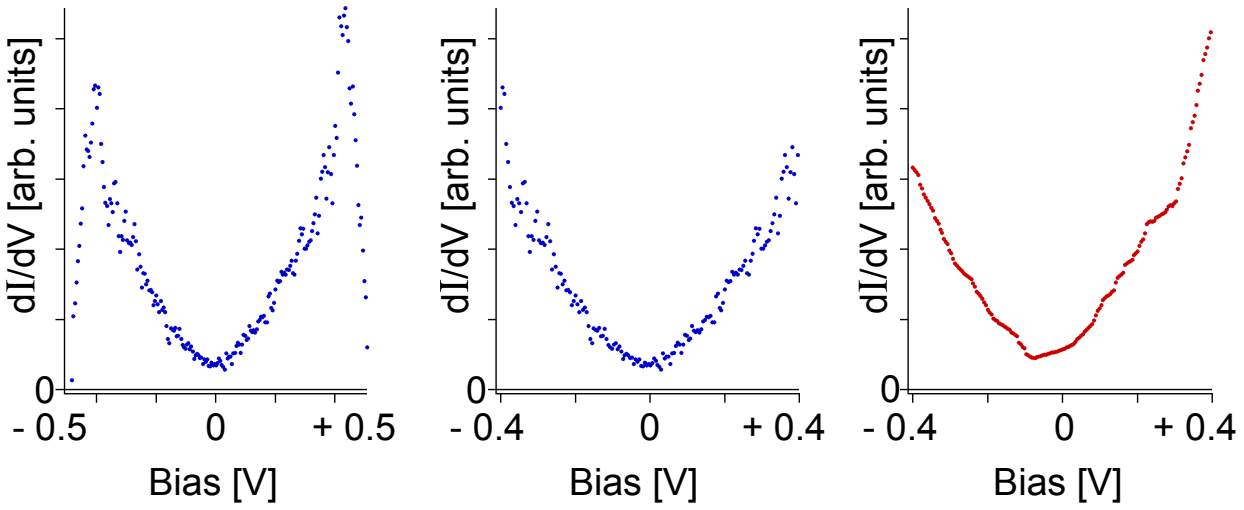

Figure D.6: Further analysis of averaged spectroscopy from Figure D.5. Left: Numerical derivative of averaged I–V curves after smoothing with a 47-point Savitzky–Golay filter using a 2nd-order polynomial to calm down some of the scatter in the data. Center: Same as left but only plotted between $\pm$ 0.4 V. Right: Direct dI/dV via the lock-in, averaged and replotted on same scales as center plot. Black lines at bottoms of plots are $dI/dV = 0$.

D.5 Tip Characterization

To ensure that a sufficiently high-quality tip existed at the start of each experiment, tips were characterized by scanning bare graphite before sample deposition. In some cases, the graphite was scanned immediately before deposition to ensure the graphite cleave was of high quality and did not leave loose graphite dust strewn about the surface; in others, the graphite was recleaved immediately before deposition. Neither of these procedures appeared to affect the appearance of the graphite substrate during the experiment. Graphite is a layered material and hence presents step edges of knowable sharpness against which the aspect ratio of the tip can be tested. From the apparent sharpness of the graphite step edges, the approximate dimensions of the pili, when deposited, can be predicted for that particular tip.

As a "reality check" for the spectroscopic measurements on pili, point spectroscopy mea-

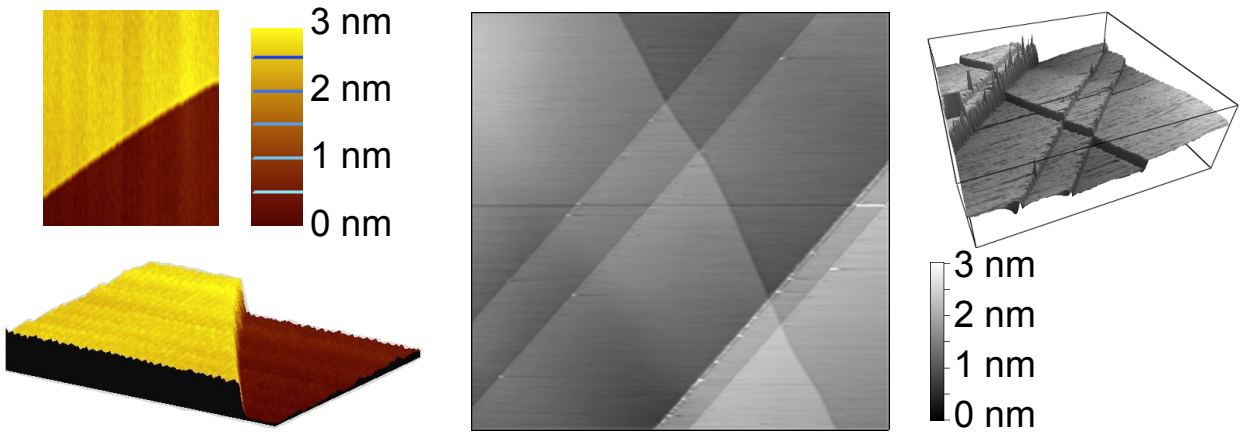

Figure D.7: Left: Standard and 3D view of a graphite step, several monolayers in height, obtained using the cryogenic-capable STM. Scan is 342 nm in the X direction and 418 nm in the Y direction. (+ 0.5 V, 1 nA) Center: 2 μm $\times$ 2 μm scan of overlapping graphite steps, obtained using the Cypher STM. Right: 3D display of overlapping steps. (+ 0.5 V, 0.2 nA)

surements were routinely performed on graphite before depositing the sample. This could, for example, help diagnose difficulties in the electrical connection delivering the bias voltage to the sample. In addition, control spectra were obtained on graphite before and after spectra were taken on locations on pili, in order to verify that the tip was still giving realistic spectroscopy as expected for a Pt:Ir tip on a graphite surface and that the tip hadn't picked up a particle from the sample, nor that there was a loose piece of tip which was mechanically unstable. A more thorough discussion of spectroscopic artifacts can be found in Appendix B.

Once an STM tip developed an undesirable characteristic such as a multiple tip or unstable behavior during scanning or spectroscopy, there were several methods by which it could be reformed into a more convenient shape. If a tip had acquired a contaminant particle, shaking the tip to dislodge it mechanically could be productive. This could also be useful if one of the STM "minitips" at the end of the tip was somewhat loose and causing unstable imaging or spectroscopy. Additionally, strong forces from the electric field between the tip and the sample in STM could be used to pull off contaminants or unsatisfactory minitips,

leaving a different minitip as the apex of the STM tip. AFM tips have more limited recovery options than STM tips and were customarily replaced rather than recovered.

D.6 AFM Phase Imaging

In amplitude modulation atomic force microscopy, the cantilever is driven in oscillatory motion very near to the sample surface, and the tip's interactions with the surface affect the oscillation of the cantilever. The feedback signal for the AFM in this mode, and thus the source of the height imaging signal, is the change in the tip–sample separation needed to keep the cantilever's oscillation amplitude constant. Surface properties can also affect the phase of the cantilever's oscillation. In essence, interaction with the sample shifts the resonance frequency of the cantilever from its free space value [101], which shifts the resonance frequency of the cantilever with respect to the frequency at which the cantilever is driven. This frequency shift can be described by a phase. Areas of a sample which are stickier can delay the cantilever's return to the peak of its amplitude, and areas of a sample which are softer will absorb more of the cantilever's vibrational energy [102] and thereby damp the resonance frequency of the cantilever. Thus the phase contrast in different parts of a scan can be used to detect surface properties other than height using AFM. Although this is qualitative [102] because it is difficult to disentangle the effects of softness vs. stickiness without using complementary techniques, it is a tremendously useful technique for detecting different types of materials which may differ only very slightly from one another in height. Indeed, for studies of soft pilus nanowires on a hard SiO_2 surface, the pili were generally more easily identifiable in phase than in height images. This also facilitated the identification of patches in Figure C.5 as being a different substance rather than a layer of well-packed pili.

D.7 Conductive AFM

Conductive AFM (often abbreviated C-AFM, or, more commonly in the field of protein nanowire studies, CP-AFM for "conductive probe" or "conducting probe" AFM) is a natural tool to use for scanning probe electronic measurements of *Geobacter* pili. While an overview is given here, results using this technique are discussed in Reference [25]. Conductive AFM tips are generally standard AFM tips coated with gold or platinum to provide a conducting path from the tip to the measurement electronics. Unlike in standard AFM, the tip–sample system is biased to induce an electrical current for the measurement. Unlike STM, this current only flows when the tip is in contact with the sample surface. The tip can be scanned in contact with the surface to detect this current at all points on the sample as a function of the applied voltage, with the tip pressing into the sample with a nanonewton-scale force to ensure stable electrical contact. An alternate method of obtaining conductivity measurements using AFM is by scanning the sample in intermittent-contact mode, then carefully selecting points and performing I–V curves with the tip coming into contact specifically with these points, a direct-conduction implementation of point spectroscopy.

If these measurements are performed on a conductive substrate, this can give information about the transverse conductivity of a sample such as pilus nanowires. STM was chosen over CP-AFM to address the electronic properties of *Geobacter* pili for the research described here, for several reasons. First, the spatial resolution of STM is generally higher than that of intermittent-contact AFM in an ambient environment, which is often used for CP-AFM studies of proteins' transverse electronic properties. Second, STM perturbs the structure of the pili less than CP-AFM does, since it does not need to press the tip into the sample in order to obtain electronic information. This is an important consideration, both from an

in-principle and from a practical standpoint. From an in-principle perspective, touching the sample with an AFM tip can alter the sample's structure if too much force is applied; the tip can press into or even punch through the pilus, complicating interpretation of results, as it would be difficult to determine exactly how much of the pilus was in contact with the tip [59]. Practically, the AFM tips tend not to be positioned solely atop pili when doing these measurements, and much care needs to be taken to avoid applying too much voltage between the tip and the surface to avoid tip damage. A voltage magnitude which may be necessary in order to cause a pilus with poor electrical contact to the sample substrate to conduct may cause a high enough current to melt the conductive coating from the tip when the tip touches the conductive substrate. Third, the apparatus and expertise were readily available to perform the temperature-dependence studies using STM.

In addition to this use of CP-AFM to probe the transverse conductivity of the sample, the CP-AFM tip can be used as a movable probe point for a two-terminal electronic transport measurement along the longitudinal direction, if another immobile terminal is provided for the measurement. Microfabrication of electrodes for a two-terminal conductivity measurement using CP-AFM is described in Appendix E.

D.8 STM Topography of Pilus Ends

Complementary to the scans focusing on the middle reaches of pilus lengths, topography was obtained on the ends of nanowires, as shown in Figure D.8. These ends display a characteristic notch several nanometers long where one side of the pilus is truncated before the other side ends. Detailed observation of the left image in Figure D.8 shows that this notch is longer than the longitudinal separation between nodules. Because the pili were purified, it

is not certain whether this "end" is the root of a pilus as would be anchored in the bacterium, the tip of a pilus farthest away from the bacterium, or a breakage plane along which the pilus was fragmented. The end could be speculated to be composed of an incomplete turn of the helical pilus coil, and the tail part which continues past the notch consists of the heads of pilins forming a partial coil. Alternatively, the end could be speculated to be composed of exposed α-helices which customarily are buried on the inside of the pili. In the "broken pilus" case, either of these speculations could apply, or the pilus could be sundered at another point. Further investigation would be necessary to disentangle these options to identify these notches. An exquisitely careful deconvolution of tip shape to obtain a more accurate lateral measurement of the widths of the notches, inspired by the pilin structure [52, 53], could assist in this determination.

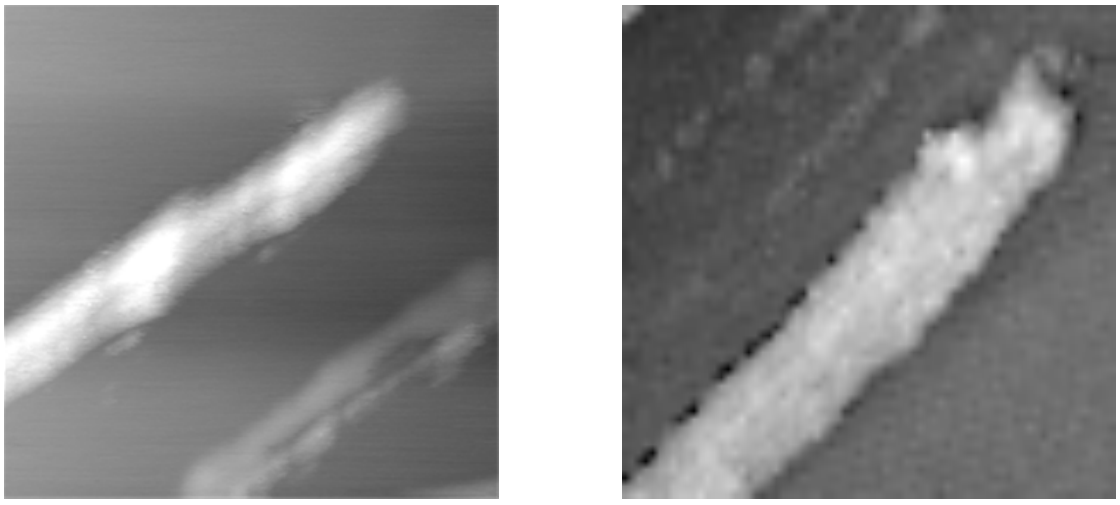

Figure D.8: STM topographs of the "ends" of two separate pili showing the characteristic notch. Both images are 75 nm $\times$ 75 nm. Both scans were performed at an applied bias of + 0.5 V. Left image tunneling current setpoint 0.2 nA, right 0.08 nA. The ghostly "echoes" in both images are due to a multiple tip effect.

Appendix E

Microfabrication of Electrodes

While this Appendix does not include experimental data from the study of *G. sulfurreducens* pilus nanowire longitudinal conductivity (see instead Reference [25]), methods for photolithographically fabricating the electrodes for that study are included here.

E.1 Goal and Starting Point

The conductive probe atomic force microscopy (CP-AFM) measurement using the electrodes whose microfabrication is described here aimed to investigate the lateral conductivity along the pilus nanowires. In brief, the idea was to let a microfabricated gold pattern on an insulating substrate act as one terminal of a resistance measurement and the conductive AFM probe act as the other terminal. By making resistance measurements at different tip–electrode separations along a pilus, resistance as a function of tip–electrode separation would permit determination of the resistivity of the pilus independent of the contact resistance between the pilus and the electrode and between the pilus and the tip. Because the tip was in direct contact with the pilus, contact resistance due to the tip was expected to depend also on the amount of force applied by the tip.

This project was a continuation of the work of Joshua Veazey and Sanela Lampa-Pastirk in collaboration with Jiebing Sun and Pengpeng Zhang. This team had obtained one measurement of the pilus longitudinal conductivity [22] which needed reproduction and expan-

sion. Further refinements were made to the procedure used for that measurement in an endeavor to expand that study. Because of the priority of obtaining cryogenic STM and point tunneling spectroscopy results, this project was continued, and successfully concluded, by Sanela Lampa-Pastirk [25].

The objective of the microfabrication of these electrodes was to create continuous, yet thin electrodes over which pili could drape, partially on the electrode and partially on the nonconductive substrate. An AFM topograph of pili draping over an electrode edge in this fashion is shown in Figure E.1. The tip would be positioned at various locations along the pili for the CP-AFM measurement.

E.2 Photolithography

The electrode patterns were fabricated using ultraviolet photolithography via an AB-M Mask Aligner in the W. M. Keck Microfabrication Facility Class 100 cleanroom at MSU. The gold electrodes were subsequently thermally evaporated in the adjoining Class 1000 cleanroom using an Edwards Auto 306 Thermal Evaporator. The resulting electrodes were characterized using one or both of the following atomic force microscopes: a Digital Instruments Dimension 3100 with Nanoscope IIIa controller for topography and an Asylum Research Cypher for topography and conductivity.

E.2.1 Materials

Electrodes were microfabricated onto silicon substrates covered by 300 nm thermally-grown oxide layers, obtained from Silicon Quest International after the optimal substrate supplier was determined. Because of the thick thermal oxide layer, the substrates were highly resistive

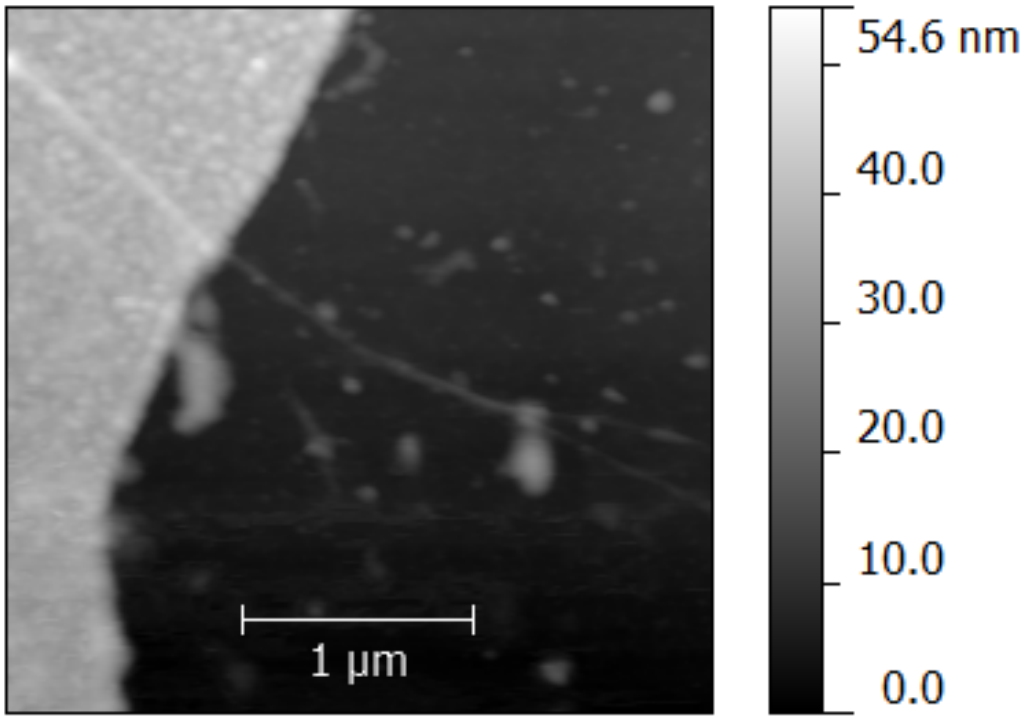

Figure E.1: AFM topograph of a microfabricated electrode and pili. Scan is 3 μm x 3 μm. The brighter region on the left is a gold electrode; the lower, darker-shaded region is the insulating substrate, exposed as a Swiss-cheese-like circular cut-out in the electrode. The tendril lying across the electrode and substrate is a small bundle, likely a pair, of pili.

and unlikely to give spurious current. Electrodes were fabricated out of gold of 99.99% purity atop a titanium "sticking layer" deposited in order to facilitate bonding of gold to the substrate. For most of the electrodes fabricated for this project, a good compromise enabling low electrode heights to decrease the steepness of the edges the pili would have to drape over while maintaining a continuous layer of conducting material was reached when the electrode consisted of 23 nm of gold atop 2 nm of titanium.

E.2.2 Procedure

The following describes the final version of the photolithography procedure using this photomask. Like most photolithographic processes, many iterations were required to devise a procedure that gave acceptable outcomes. The overall procedure is schematically shown in Figure E.2; the realities of photolithography process development are more subtle.

Figure E.2: Diagram of the photolithography procedure, not to scale. Left to right: substrate with photoresist deposited on top, photoresist exposed and developed to leave a pattern, gold deposited on the pattern and photoresist, photoresist "lifted off" to leave solely the pattern.

Chip Cleaning

The surfaces supporting the electrodes must be extremely clean, lest the electrodes adhere to a removable contaminant layer rather than to the chips themselves. Before photolithography cleaning, thermally-oxidized silicon wafers were cut into 1/2 inch $\times$ 1/2 inch chips. Dicing the chips rather than hand-cleaving them with a scribe resulted in more regularly-shaped chips and, therefore, a more reproducible photolithography protocol. A layer of photoresist was spun onto the wafer to protect the surface during dicing. The chips were then cleaned according to the following protocol:

Initial removal of protective resist, if chips were diced

- Ultrasonicate for 1 minute in acetone, rinse with acetone
- Ultrasonicate for 1 minute in isopropyl alcohol (IPA), rinse with IPA

Cleaning with a detergent, which must then be thoroughly rinsed off

- Ultrasonicate for 3 minutes in a 1% solution of Alconox in deionized water (DI H_2O)
- Rinse for 1 minute with DI H_2O
- Ultrasonicate for 3 minutes in DI H_2O, rinse with DI H_2O

Cleaning with solvents to remove organic contaminants [103]

- Scrub for 1 minute in acetone, scrubbing in only one direction with a cotton swab
- Ultrasonicate for 3 minutes in acetone, rinse with acetone
- Ultrasonicate for 3 minutes in IPA, rinse with IPA
- Ultrasonicate for 3 minutes in DI H_2O, rinse with DI H_2O
- Leave in DI H_2O for transportation to the cleanroom

Cleaning in the cleanroom, immediately before spinning on photoresist

- Ultrasonicate for 2 minutes in acetone, rinse with acetone
- Ultrasonicate for 2 minutes in IPA, rinse with IPA
- Ultrasonicate for 2 minutes in DI H_2O, rinse with DI H_2O
- Dry with N_2 gas
- (Optional) Heat for 1 minute on a 100°C bakeplate to evaporate additional water

Ultraviolet Exposure and Photoresist Developing

The pattern which would form the electrodes was created by shining ultraviolet light through holes in a photomask in order to create the desired pattern on the substrate. Akin to the classic photographic developing process, photoresist must also be developed to obtain the "image" upon which the metal electrodes will be deposited. The Shipley Microposit S1813 photoresist used for this work was a "positive" photoresist [104], meaning that the areas of the photoresist exposed to the ultraviolet light would dissolve and wash away when exposed to the developer (here, Shipley 352 developer). The photomask used to define the patterns for the electrodes was a repurposed photomask from a previous project, which had a veritable plethora of different patterns on it from which to select. For this project, it was important for the electrodes to be continuous, since the bias voltage to the electrodes would only be delivered at one or two locations.

As in most photolithography, this procedure required an appreciable amount of optimization. The exposure and developing steps contribute in a non-independent fashion to the overall result. Both overexposure and overdeveloping, for example, dissolve "too much" of the photoresist, resulting in malformed electrodes. Optimization of the procedure does not imply that this is the best possible way to fabricate these electrodes, but rather that electrodes made in this way were sufficiently functional. The protocol eventually settled on involved exposing the photoresist through the mask for 8 seconds, followed by agitating it in the developer for 30 seconds before rinsing thoroughly with DI H_2O.

The photoresist was initially spin-coated onto the chips, which were then placed on a bakeplate for a few minutes to ensure the photoresist was sufficiently dry [104] before ultraviolet exposure of the pattern. Following this, the mask aligner was used to press the

photoresist-covered chip against the mask, after which the ultraviolet light source was turned on and shone through the holes in the photomask, exposing that portion of the photoresist. The exposed chips were then post-baked on the hotplate. After the photoresist-covered and exposed chips were swished around in the developer, they were immediately rinsed with DI H_2O in order to remove residual developer. If they had not been rinsed immediately thereafter, the remaining developer would have continued to work on the photoresist.

Thermal Evaporation

Thermal evaporation is a commonly-used technique to deposit material on surfaces. The material, such as gold, to be deposited is placed in solid source form on a metal "boat" which is resistively heated by having current run through it. This, in turn, heats the gold until it melts and then evaporates. The evaporated material then sticks to the substrate surfaces, which are suspended in a vacuum chamber above the evaporation source. Since gold does not bond well to silicon, it is customary to include an "adhesion layer" of a few nanometers of titanium between the silicon and the gold [103]. An example of a chip at the microfabrication stage where gold has been evaporated over the entire surface is shown on the left side of Figure E.3, contrasted with the post-liftoff outcome.

Liftoff

After evaporation of titanium and gold, the underlying photoresist was removed by immersing, agitating, or rinsing the chip in acetone. Turbulence from agitating the chip in the acetone was generally sufficient to tear away, or lift off, gold which was not directly attached to the substrate. Of the liftoff protocols ventured during this experiment, some of the best results were obtained by soaking the chips in acetone at 90° C for ten minutes immediately

Figure E.3: Left: Photograph of a chip with electrodes patterned into photoresist and a layer of gold evaporated over the whole chip, before liftoff. The pattern of the electrodes can be seen as darker areas on the shiny surface. Right: Photograph of a chip after liftoff. The electrodes are the rectangular patterns. Chips are approximately 0.5 inches wide.

after evaporation, then leaving them overnight in fresh, room-temperature acetone. The next morning, the chips were quickly rinsed with acetone from a wash bottle in order to remove large leaves of gold from between the electrode areas; sonicated in acetone for one minute in fresh acetone; rinsed with a continuous stream of acetone from a wash bottle for one minute; and rinsed with acetone, IPA, and DI H_2O before drying with N_2 gas.

In principle, this procedure should result in continuous electrodes with uniform edges, with the gold firmly affixed to the substrate. While this was not always the case, the highest-quality electrodes thus produced were used for the CP-AFM experiments. For these experiments, a bias voltage was delivered to the electrodes via an external wire from the AFM. This wire attached to a magnet on the AFM sample-mounting disk to which was affixed the completed chip with electrodes and sample. Therefore, there needed to be a continuously conducting path between the disk's magnet and the electrodes. This was provided via a continuous path of silver paint, adhesive with a sufficiently large concentration of silver particles to render the paint conductive, between the magnet and a gold pad on the surface.

This gold pad then served as a voltage source for the electrodes. The electrodes were connected to the voltage pad with 1 mil-diameter 99.99% pure gold wire, using a West·Bond wire bonder to make the connections. The finished product is shown in Figure E.4.

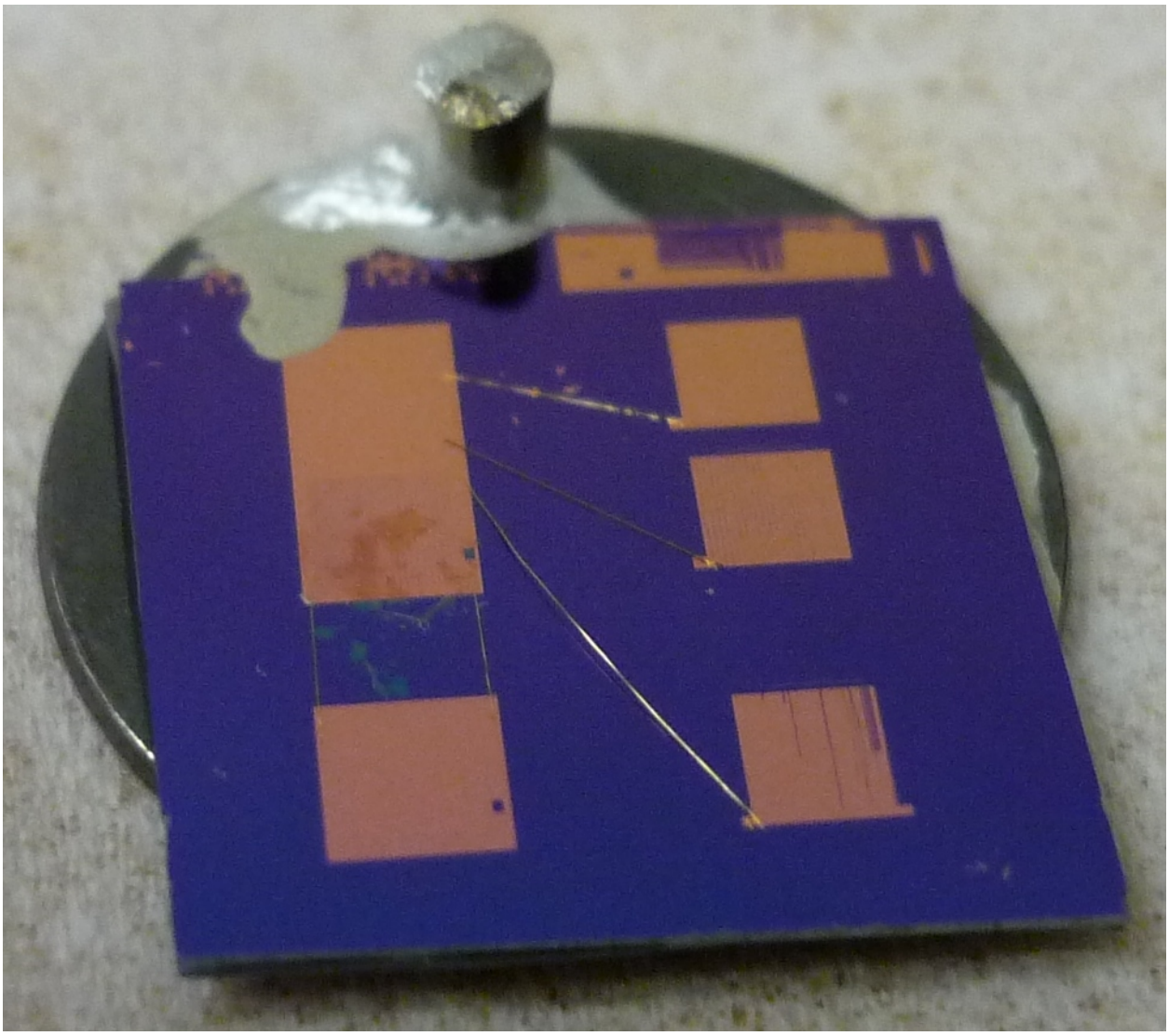

Figure E.4: Photograph of a sample used for the CP-AFM experiment. For scale, the disk on which the chip is mounted is 15 mm in diameter. The cylinder at the top of the image is the magnet to which the bias wire from the microscope was attached. Conductive silver paint connects this to a solid gold pad which is then connected via gold wires or by direct contact to electrodes on the chip. Residue of sample deposition can be seen on one of the electrodes at left in the image.

REFERENCES

REFERENCES

[1] F. Qian and Y. Li. Biomaterials: A natural source of nanowires. *Nature Nanotechnology*, 6:538–539, 2011.

[2] C.-Y. Chiang, C. Mello, J. Gu, E. Silva, K. VanVliet, and A. Belcher. Weaving genetically engineered functionality into mechanically robust virus fibers. *Advanced Materials*, 19(6):826–832, 2007.

[3] G. Reguera, K. D. McCarthy, T. Mehta, J. S. Nicoll, M. T. Tuominen, and D. R. Lovley. Extracellular electron transfer via microbial nanowires. *Nature*, 435:1098–1101, 2005.

[4] Y. A. Gorby, S. Yanina, J. S. McLean, K. M. Rosso, D. Moyles, A. Dohnalkova, T. J. Beveridge, I. S. Chang, B. H. Kim, K. S. Kim, D. E. Culley, S. B. Reed, M. F. Romine, D. A. Saffarini, E. A. Hill, L. Shi, D. A. Elias, D. W. Kennedy, G. Pinchuk, K. Watanabe, S. Ishii, B. Logan, K. H. Nealson, and J. K. Fredrickson. Electrically conductive bacterial nanowires produced by *Shewanella oneidensis* strain MR-1 and other microorganisms. *Proceedings of the National Academy of Sciences of the USA*, 103(30):11358–11363, 2006.

[5] G. Wanger, Y. Gorby, M. Y. El-Naggar, T. D. Yuzvinsky, C. Schaudinn, A. Gorur, and P. P. Sedghizadeh. Electrically conductive bacterial nanowires in bisphosphonate-related osteonecrosis of the jaw biofilms. *Oral Surgery, Oral Medicine, Oral Pathology and Oral Radiology*, 115(1):71–78, 2013.

[6] J. S. Mattick. Type IV pili and twitching motility. *Annual review of Microbiology*, 56:289–314, 2002.

[7] N. Guex and M. C. Peitsch. SWISS-MODEL and the Swiss-Pdb Viewer: An environment for comparative protein modeling. *Electrophoresis*, 18(15):2714–2723, 1997.

[8] G. T. Feliciano, A. J. R. d. Silva, G. Reguera, and E. Artacho. Molecular and electronic structure of the peptide subunit of Geobacter sulfurreducens conductive pili from first principles. *The Journal of Physical Chemistry A*, 116(30):8023–8030, 2012.

[9] D. S. Goodsell. Representing structural information with RasMol. In *Current Protocols in Bioinformatics*. John Wiley & Sons, Inc., 2002.

[10] F. Caccavo, D. J. Lonergan, D. R. Lovley, M. Davis, J. F. Stolz, and M. J. McInerney. *Geobacter sulfurreducens* sp. nov., a hydrogen- and acetate-oxidizing dissimilatory metal-reducing microorganism. *Applied and Environmental Microbiology*, 60(10):3752–3759, 1994.

[11] D. R. Lovley, E. J. Phillips, Y. A. Gorby, and E. R. Landa. Microbial reduction of uranium. *Nature*, 350:413–416, 1991.

[12] D. L. Cologgi, S. Lampa-Pastirk, A. M. Speers, S. D. Kelly, and G. Reguera. Extracellular reduction of uranium via Geobacter conductive pili as a protective cellular mechanism. *Proceedings of the National Academy of Sciences of the United States of America*, 108(37):15248–15252, 2011.

[13] D. R. Lovley. Cleaning up with genomics: Applying molecular biology to bioremediation. *Nature Reviews Microbiology*, 1:35–44, 2003.

[14] P. Sturman, P. Stewart, A. Cunningham, E. Bouwer, and J. Wolfram. Engineering scale-up of in situ bioremediation processes: a review. *Journal of Contaminant Hydrology*, 19(3):171–203, 1995.

[15] D. R. Lovley. Bug juice: harvesting electricity with microorganisms. *Nature Reviews Microbiology*, 4:497–508, 2006.

[16] G. Reguera, K. P. Nevin, J. S. Nicoll, S. F. Covalla, T. L. Woodard, and D. R. Lovley. Biofilm and nanowire production leads to increased current in Geobacter sulfurreducens fuel cells. *Applied and Environmental Microbiology*, 72(11):7345–7348, 2006.

[17] J. A. Gralnick and D. K. Newman. Extracellular respiration. *Molecular Microbiology*, 65:1–11, 2007.

[18] D. R. Lovley, J. D. Coates, E. L. Blunt-Harris, E. J. Phillips, and J. C. Woodward. Humic substances as electron acceptors for microbial respiration. *Nature*, 382:445–448, 1996.

[19] K. P. Nevin and D. R. Lovley. Lack of production of electron-shuttling compounds or solubilization of Fe(III) during reduction of insoluble Fe(III) oxide by *Geobacter metallireducens*. *Applied and Environmental Microbiology*, 66:2248–2251, 2000.

[20] M. S. Strom and S. Lory. Structure-function and biogenesis of the type IV pili. *Annual Review of Microbiology*, 47(1):565–596, 1993.

[21] G. Reguera, R. B. Pollina, J. S. Nicoll, and D. R. Lovley. Possible nonconductive role of *Geobacter sulfurreducens* pilus nanowires in biofilm formation. *Journal of Bacteriology*, 189(5):2125–2127, 2007.

[22] J. P. Veazey. *Scanning Probe Studies of the Pilus Nanowires in Geobacter sulfurreducens*. PhD thesis, Michigan State University, 2011.

[23] J. P. Veazey, G. Reguera, and S. H. Tessmer. Electronic properties of conductive pili of the metal-reducing bacterium *Geobacter sulfurreducens* probed by scanning tunneling microscopy. *Phys. Rev. E*, 84:060901, 2011.

[24] M. Y. El-Naggar, G. Wanger, K. M. Leung, T. D. Yuzvinsky, G. Southam, J. Yang, W. M. Lau, K. H. Nealson, and Y. A. Gorby. Electrical transport along bacterial nanowires from *Shewanella oneidensis* MR-1. *Proceedings of the National Academy of Sciences of the United States of America*, 107(42):18127–18131, 2010.

[25] S. Lampa-Pastirk, J. P. Veazey, R. Steidl, K. A. Walsh, S. Tessmer, and G. Reguera. Long-range electron transport via microbial protein nanowires. *in preparation*, 2013.

[26] L. Craig, M. E. Pique, and J. A. Tainer. Type IV pilus structure and bacterial pathogenicity. *Nature Reviews Microbiology*, 2:363–378, 2004.

[27] J. J. Davis. Molecular bioelectronics. *Philosophical Transactions of the Royal Society A*, 361:2807–2825, 2003.

[28] J. W. G. Wildöer, L. C. Venema, A. G. Rinzler, R. E. Smalley, and C. Dekker. Electronic structure of atomically resolved carbon nanotubes. *Nature*, 391:59–62, 1998.

[29] T. W. Odom, J.-L. Huang, P. Kim, and C. M. Lieber. Atomic structure and electronic properties of single-walled carbon nanotubes. *Nature*, 391:62–64, 1998.

[30] C. J. Chen. *Introduction to Scanning Tunneling Microscopy*. Monographs on the Physics and Chemistry of Materials. Oxford University Press, New York, 2nd edition, 2008.

[31] A. F. Raigoza, J. W. Dugger, and L. J. Webb. Review: Recent advances and current challenges in scanning probe microscopy of biomolecular surfaces and interfaces. *ACS Applied Materials & Interfaces* preprint online, 2013.

[32] N. S. Malvankar, M. Vargas, K. P. Nevin, A. E. Franks, C. Leang, B.-C. Kim, K. Inoue, T. Mester, S. F. Covalla, J. P. Johnson, V. M. Rotello, M. T. Tuominen, and D. R.

Lovley. Tunable metallic-like conductivity in microbial nanowire networks. *Nature Nanotechnology*, 6:573–579, 2011.

[33] S.-i. Park, J. Nogami, and C. F. Quate. Effect of tip morphology on images obtained by scanning tunneling microscopy. *Phys. Rev. B*, 36:2863–2866, 1987.

[34] G. Binnig, H. Rohrer, C. Gerber, and E. Weibel. Surface studies by scanning tunneling microscopy. *Phys. Rev. Lett.*, 49:57–61, 1982.

[35] R. M. Feenstra. Scanning tunneling spectroscopy. *Surface Science*, 299–300(0):965–979, 1994.

[36] G. Binnig, H. Rohrer, C. Gerber, and E. Weibel. Tunneling through a controllable vacuum gap. *Applied Physics Letters*, 40(2):178–180, 1982.

[37] G. Binnig and H. Rohrer. Scanning tunneling microscopy–from birth to adolescence. *Rev. Mod. Phys.*, 59:615–625, 1987.

[38] R. J. Hamers, R. M. Tromp, and J. E. Demuth. Surface electronic structure of Si (111)-(7×7) resolved in real space. *Phys. Rev. Lett.*, 56:1972–1975, 1986.

[39] T. Arai, K. Ichimura, K. Nomura, S. Takasaki, J. Yamada, S. Nakatsuji, and H. Anzai. Superconducting and normal-state gaps in κ-(BEDT-TTF)$_2$Cu(NCS)$_2$ studied by STM spectroscopy. *Solid State Communications*, 116(12):679–682, 2000.

[40] K. Jordan, A. Cazacu, G. Manai, S. Ceballos, S. Murphy, and I. Shvets. Scanning tunneling spectroscopy study of the electronic structure of Fe_3O_4 surfaces. *Physical Review B*, 74:085416–1–6, 2006.

[41] G. Binnig, C. F. Quate, and C. Gerber. Atomic force microscope. *Phys. Rev. Lett.*, 56:930–933, 1986.

[42] R. Proksch, T. E. Schäffer, J. P. Cleveland, R. C. Callahan, and M. B. Viani. Finite optical spot size and position corrections in thermal spring constant calibration. *Nanotechnology*, 15(9):1344, 2004.

[43] K. Besocke. An easily operable scanning tunneling microscope. *Surface Science*, 181:145–153, 1987.

[44] J. Frohn, J. Wolf, K. Besocke, and M. Teske. Coarse tip distance adjustment and positioner for a scanning tunneling microscope. *Review of Scientific Instruments*, 60:1200–1201, 1989.

[45] K. A. Walsh, M. E. Romanowich, M. Gasseller, I. Kuljanishvili, R. Ashoori, and S. Tessmer. Scanning-probe single-electron capacitance spectroscopy. *Journal of Visualized Experiments*, 77:e50676, 2013.

[46] W.-T. Pong and C. Durkan. A review and outlook for an anomaly of scanning tunnelling microscopy (STM): superlattices on graphite. *Journal of Physics D: Applied Physics*, 38(21):R329, 2005.

[47] Y. Baskin and L. Meyer. Lattice constants of graphite at low temperatures. *Physical Review*, 100(2), 1955.

[48] P. Kes, C. v. d. Klein, and D. d. Klerk. A new R–T relation for Allen-Bradley carbon resistor thermometers. *Cryogenics*, 14(3):168–169, 1974.

[49] W. N. Lawless, S. K. Hampton, and C. F. Clark. Calibration scheme for Allen–Bradley resistors, 4.2–100 k. *Review of Scientific Instruments*, 59(11):2505–2507, 1988.

[50] J. Freund, J. Halbritter, and J. Hörber. How dry are dried samples? Water adsorption measured by STM. *Microscopy Research and Technique*, 44(5):327–338, 1999.

[51] L. Craig, N. Volkmann, A. S. Arvai, M. E. Pique, M. Yeager, E. H. Egelman, and J. A. Tainer. Type {IV} pilus structure by cryo-electron microscopy and crystallography: Implications for pilus assembly and functions. *Molecular Cell*, 23(5):651 – 662, 2006.

[52] P. N. Reardon and K. T. Mueller. Structure of the type IVa major pilin from the electrically conductive bacterial nanowires of Geobacter sulfurreducens. *Journal of Biological Chemistry* preprint online, 2013.

[53] P. Reardon and K. Mueller. Structure of the type IVa major pilin from the electrically conductive bacterial nanowires of Geobacter sulfurreducens.

[54] E. Artacho, E. Anglada, O. Diéguez, J. D. Gale, A. García, J. Junquera, R. M. Martin, P. Ordejón, J. M. Pruneda, D. Sánchez-Portal, and J. M. Soler. The SIESTA method; developments and applicability. *Journal of Physics: Condensed Matter*, 20(6):064208, 2008.

[55] J. M. B. Jr. Electron relay in proteins. *Science*, 320:1730–1731, 2008.

[56] R. I. Cukier and D. G. Nocera. Proton-coupled electron transfer. *Annual Review of Physical Chemistry*, 49(1):337–369, 1998.

[57] H. Gray and J. Winkler. Electron flow through proteins. *Chemical Physics Letters*, 483:1–9, 2009.

[58] L. K. Skov, T. Pascher, J. R. Winkler, and H. B. Gray. Rates of intramolecular electron transfer in Ru(bpy)2(im)(His83)-modified azurin increase below 220 K. *Journal of the American Chemical Society*, 120(5):1102–1103, 1998.

[59] N. F. Polizzi, S. S. Skourtis, and D. N. Beratan. Physical constraints on charge transport through bacterial nanowires. *Faraday Discussions*, 155:43–62, 2011.

[60] T. Kakitani and N. Mataga. Effects of freezing out protein vibrational modes on electron transfer kinetics in bacterial reaction centers. *Photosynthesis Research*, 22:187–193, 1989.

[61] J.-J. Kim, I. Ekvall, and H. Olin. Temperature-dependent scanning tunneling spectroscopy of $1T$-TaS_2. *Physical Review B*, 54(3):2244–2248, 1996.

[62] K. Ichimura, M. Kobayashi, K. Nomura, T. Hanajiri, J. Yamada, S. Nakatsuji, and H. Anzai. SDW gap in $(TMTSF)_2PF_6$: STM spectroscopy. *Synthetic Metals*, 120(1–3):897–898, 2001. Proceedings of the International Conference on the Science and Technology of Synthetic Metals.

[63] G. Travaglini, H. Rohrer, M. Amrein, and H. Gross. Scanning tunneling microscopy on biological matter. *Surface Science*, 181(1–2):380–390, 1987.

[64] A. Szent-Györgyi. Towards a new biochemistry? *Science*, 93(2426):609–611, 1941.

[65] J. Veazey, S. Lampa-Pastirk, G. Feliciano, G. Reguera, E. Artacho, and S. Tessmer. Evidence of rectification in the local electronic structure of microbial nanowires. *to be submitted*, 2013.

[66] W. Humphrey, A. Dalke, and K. Schulten. VMD: Visual molecular dynamics. *Journal of Molecular Graphics*, 14(1):33 –38, 1996.

[67] B. Hess, C. Kutzner, D. v. d. Spoel, and E. Lindahl. GROMACS 4: Algorithms for highly efficient, load-balanced, and scalable molecular simulation. *Journal of Chemical Theory and Computation*, 4:435–447, 2008.

[68] K. Capelle. A bird's-eye view of density-functional theory. *arXiv:cond-mat/0211443v5* 1–35.

[69] J. M. Soler, E. Artacho, J. D. Gale, A. García, J. Junquera, P. Ordejón, and D. Snchez-Portal. The SIESTA method for *ab initio* order-N materials simulation. *Journal of Physics: Condensed Matter*, 14(11):2745–2779, 2002.

[70] J. P. Perdew, K. Burke, and M. Ernzerhof. Generalized gradient approximation made simple. *Physical Review Letters*, 77:3865–3868, 1996.

[71] R. K. Clayton. Effects of dehydration on reaction centers from Rhodopseudomonas sphaeroides. *Biochimica et Biophysica Acta (BBA)–Bioenergetics*, 504(2):255–264, 1978.

[72] R. Guckenberger, M. Heim, G. Cevc, H. F. Knapp, W. Wiegräbe, and A. Hillebrand. Scanning tunneling microscopy of insulators and biological specimens based on lateral conductivity of ultrathin water films. *Science*, 266:1538–1540, 1994.

[73] D. Martinez-Martin, R. Longuinhos, J. G. Izquierdo, A. Marele, S. S. Alexandre, M. Jaafar, J. M. Gómez-Rodríguez, L. Bañares, J. M. Soler, and J. Gomez-Herrero. Atmospheric contaminants on graphitic surfaces. *Carbon*, 61:33–39, 2013.

[74] R. Proksch. Multifrequency, repulsive-mode amplitude-modulated atomic force microscopy. *Applied Physics Letters*, 89(11):113121, 2006.

[75] D. J. Müller, M. Amrein, and A. Engel. Adsorption of biological molecules to a solid support for scanning probe microscopy. *Journal of Structural Biology*, 119:172–188, 1997.

[76] S.-F. Shi, K. I. Bolotin, F. Kuemmeth, and D. C. Ralph. Temperature dependence of anisotropic magnetoresistance and atomic rearrangements in ferromagnetic metal break junctions. *Physical Review B*, 76:184438, 2007.

[77] R. Mahadevan, D. R. Bond, J. E. Butler, A. Esteve-Nuñez, M. V. Coppi, B. O. Palsson, C. H. Schilling, and D. R. Lovley. Characterization of metabolism in the Fe(III)-reducing organism Geobacter sulfurreducens by constraint-based modeling. *Applied and Environmental Microbiology*, 72(2):1558–1568, 2006.

[78] B. Rosenberg. Electrical conductivity of proteins. II. Semiconduction in crystalline bovine hemoglobin. *The Journal of Chemical Physics*, 36(3), 1962.

[79] J. J. Davis and H. A. O. Hill. The scanning probe microscopy of metalloproteins and metalloenzymes. *Chemical Communications* 393–401, 2002.

[80] N. S. Wigginton, K. M. Rosso, B. H. Lower, L. Shi, and M. F. H. Jr. Electron tunneling properties of outer-membrane decaheme cytochromes from Shewanella oneidensis. *Geochimica et Cosmochimica Acta*, 71(3):543–555, 2007.

[81] K. S. Novoselov, A. K. Geim, S. V. Morozov, D. Jiang, Y. Zhang, S. V. Dubonos, I. V. Grigorieva, and A. A. Firsov. Electric field effect in atomically thin carbon films. *Science*, 306(5696):666–669, 2004.

[82] K. Walsh, S. MacLaren, *et al.* Engage panel tip height. https://support.asylumresearch.com/forum/showthread.php?1546-Engage-panel-tip-height, February 2013.

[83] N. Leonard, V. Nallathambi, and S. Calabrese Barton. Carbon supports for non-precious metal oxygen reducing catalysts. *Journal of the Electrochemical Society*, 160(8):F788–F792, 2013.

[84] N. D. Leonard and S. Calabrese Barton. Basicity of non-precious metal catalysts for oxygen reduction. *Meeting Abstracts*, MA2012-02(13):1698, 2012.

[85] K. Walsh *et al.* Ears in dual-gain ORCA IV curves. https://support.asylumresearch.com/forum/showthread.php?1124-Ears-in-dual-gain-ORCA-IV-curves, November 2011.

[86] C. Ware. Chapter 5–Visual salience and finding information. In *Information Visualization: Perception for Design*. Morgan Kaufmann, 2013.

[87] C. Ware. Chapter 6–Static and moving patterns. In *Information Visualization: Perception for Design*. Morgan Kaufmann, 2013.

[88] C. Ware. Chapter 11–Visual thinking processes. In *Information Visualization: Perception for Design*. Morgan Kaufmann, 2013.

[89] C. R. Clemmer and J. Beebe, Thomas P. Graphite: A mimic for DNA and other biomolecules in scanning tunneling microscope studies. *Science*, 251(4994):640–642, 1991.

[90] G. Binnig and H. Rohrer. Scanning tunneling microscopy. In J. Janta and J. Pantofliček, editors, *Trends in Physics 1984–Proceedings of the 6th General Conference of the European Physical Society* 38–45. European Physical Society, 1984.

[91] Y. Niimi, T. Matsui, H. Kambara, K. Tagami, M. Tsukada, and H. Fukuyama. Scanning tunneling microscopy and spectroscopy of the electronic local density of states of graphite surfaces near monoatomic step edges. *Phys. Rev. B*, 73:085421, 2006.

[92] P. Simonis, C. Goffaux, P. Thiry, L. Biro, P. Lambin, and V. Meunier. STM study of a grain boundary in graphite. *Surface Science*, 511:319–322, 2002.

[93] H. S. Wong, C. Durkan, and N. Chandrasekhar. Tailoring the local interaction between graphene layers in graphite at the atomic scale and above using scanning tunneling microscopy. *ACS Nano*, 3(11):3455–3462, 2009.

[94] R. Wilkins, M. Amman, E. Ben-Jacob, and R. C. Jaklevic. Single-electron and oxide-impurity effects in junctions formed by a cryogenic scanning tunneling microscope. *Phys. Rev. B*, 42:8698–8701, 1990.

[95] C. Schönenberger, H. v. Houten, and H. C. Donkersloot. Single-electron tunnelling observed at room temperature by scanning-tunnelling microscopy. *EPL (Europhysics Letters)*, 20(3):249, 1992.

[96] J. P. Pelz. Tip-related electronic artifacts in scanning tunneling spectroscopy. *Phys. Rev. B*, 43:6746–6749, 1991.

[97] S. Lindsay, N. Tao, J. DeRose, P. Oden, L. Yu.L., R. Harrington, and L. Shlyakhtenko. Potentiostatic deposition of DNA for scanning probe microscopy. *Biophysical Journal*, 61(6):1570–1584, 1992.

[98] X. Xi, J. Shi, S. Maghsoudy-Louyeh, and B. R. Tittmann. Characterization of silicon wafer surfaces after hydrophilic and hydrophobic treatments by atomic force microscopy. *AIP Conference Proceedings*, 1211(1):1493–1498, 2010.

[99] F. Zhang, H.-N. Du, Z.-X. Zhang, L.-N. Ji, H.-T. Li, L. Tang, H.-B. Wang, C.-H. Fan, H.-J. Xu, Y. Zhang, J. Hu, H.-Y. Hu, and J.-H. He. Epitaxial growth of peptide nanofilaments on inorganic surfaces: Effects of interfacial hydrophobicity/hydrophilicity. *Angewandte Chemie International Edition*, 45(22):3611–3613, 2006.

[100] A. Savitzky and M. J. E. Golay. Smoothing and differentiation of data by simplified least squares procedures. *Analytical Chemistry*, 36(8):1627–1639, 1964.

[101] S. Magonov, V. Elings, and M.-H. Whangbo. Phase imaging and stiffness in tapping-mode atomic force microscopy. *Surface Science*, 375(2–3):L385–L391, 1997.

[102] I. Schmitz, M. Schreiner, G. Friedbacher, and M. Grasserbauer. Phase imaging as an extension to tapping mode AFM for the identification of material properties on humidity-sensitive surfaces. *Applied Surface Science*, 115(2):190–198, 1997.

[103] K. R. Williams, K. Gupta, and M. Wasilik. Etch rates for micromachining processing—Part II. *Journal of Microelectromechanical Systems*, 12(6):761–778, 2003.

[104] A. M. Collins. Chapter 5—Physical Techniques. In *Nanotechnology Cookbook* 205–253. Elsevier, Oxford, 2012.